

**DEVELOPMENT AND VALIDATION OF A FINITE ELEMENT MODEL OF
HUMAN INTERVERTEBRAL DISC IN MULTIAXIAL LOADING
INCLUDING THE CONTRIBUTIONS OF CARTILAGE ENDPLATE AND
RESIDUAL STRAINS IN THE ANNULUS FIBROSUS**

by

John F. DeLucca

A dissertation submitted to the Faculty of the University of Delaware in partial fulfillment of the requirements for the degree of Doctor of Philosophy in Biomedical Engineering

Fall 2018

© 2018 John DeLucca
All Rights Reserved

**DEVELOPMENT AND VALIDATION OF A FINITE ELEMENT MODEL OF
HUMAN INTERVERTEBRAL DISC IN MULTIAXIAL LOADING
INCLUDING THE CONTRIBUTIONS OF CARTILAGE ENDPLATE AND
RESIDUAL STRAINS IN THE ANNULUS FIBROSUS**

by

John F. DeLucca

Approved: _____

Dawn Elliott, Ph.D.

Chair of the Department of Biomedical Engineering

Approved: _____

Levi Thompson, Ph.D.

Dean of the College of Engineering

Approved: _____

Doug Doren, Ph.D.

Interim Vice Provost for Graduate and Professional Education

I certify that I have read this dissertation and that in my opinion it meets the academic and professional standard required by the University as a dissertation for the degree of Doctor of Philosophy.

Signed:

Dawn Elliott, Ph.D.
Professor in charge of dissertation

I certify that I have read this dissertation and that in my opinion it meets the academic and professional standard required by the University as a dissertation for the degree of Doctor of Philosophy.

Signed:

Randall Duncan, Ph.D.
Member of dissertation committee

I certify that I have read this dissertation and that in my opinion it meets the academic and professional standard required by the University as a dissertation for the degree of Doctor of Philosophy.

Signed:

Edward Vresilovic, M.D., Ph.D.
Member of dissertation committee

I certify that I have read this dissertation and that in my opinion it meets the academic and professional standard required by the University as a dissertation for the degree of Doctor of Philosophy.

Signed:

Michael Santare, Ph.D.
Member of dissertation committee

I certify that I have read this dissertation and that in my opinion it meets the academic and professional standard required by the University as a dissertation for the degree of Doctor of Philosophy.

Signed:

Christopher Price, Ph.D.
Member of dissertation committee

ACKNOWLEDGMENTS

First, I would like to thank my advisor, Dr. Dawn Elliott, for her patience and guidance throughout my graduate studies. I am forever indebted to her for the chance she took by welcoming me into her lab, particularly as the biomedical engineering program at the University of Delaware was brand new. She is dedicated to her students and takes personal interest in the success of each project. Her support of my research ideas and her resiliency when dealing with any research “failures” that pop up along the way have made me a better scientist and better prepared to enter the world of employment.

I am also grateful to my committee members, Drs. Ed Vresilovic, Randy Duncan, Michael Santare, and Christopher Price. Each committee member views orthopedic biomechanics through a different lens and their thought-provoking insight has greatly influenced my graduate work. They encourage creative thinking and find the fun in science – making for a great collaborative team.

I wouldn't have been able to successfully go through graduate school without the help and support of my lab colleagues. I joined the lab at a transition period – as the last Penn students were graduating and Dawn was forming her lab in Delaware. I am forever thankful to the mentorship I had from some of the Penn lab members. In particular, Dr. Daniel Cortes was instrumental in training me in the experimental and

theoretical aspects of our lab. I am thankful to Daniel for his patience in training me as I transitioned into graduate school. I am also grateful to the mentorship of Drs. Woojin Han, Spencer Szczesny, Brent Showalter, and Nathan Jacobs. Their valuable technical insight and their guidance in overcoming the obstacles of research will stay with me throughout my career. I would also like to thank the members of the lab from Delaware: John Peloquin, Babak Safa, Andrea Lee, Ellen Bloom, and Kyle Meadows who have made the lab such a fun environment over the years.

Finally, I would like to thank all of my family members. I am eternally blessed because of their love and support for my professional aspirations. During my time in graduate school I lost three members of my family and I would not be completing a PhD without their love and moral support.

TABLE OF CONTENTS

LIST OF TABLES	viii
LIST OF FIGURES	ix
ABSTRACT	xi
Chapter	
1 INTRODUCTION	1
2 BACKGROUND	3
3 AIM 1 – MRI QUANTIFICATION OF HUMAN SPINE CARTILAGE ENDPLATE GEOMETRY: COMPARISON WITH AGE, DEGENERATION, LEVEL, AND DISC GEOMETRY	19
4 AIM 2 – HUMAN CARTILAGE ENDPLATE PERMEABILITY VARIES WITH DEGENERATION AND INTERVERTEBRAL DISC SITE	36
5 AIM 3 – MECHANICAL COUPLING WITH APPLIED LOADING CAUSES LARGE OFF-AXIS RESPONSES ACROSS ALL SIX DEGREES OF FREEDOM IN THE HUMAN DISC SEGMENT	57
6 AIM 4 – INCORPORATING RESIDUAL STRESS AND STRAIN IN A FINITE ELEMENT MODEL OF THE INTERVERTEBRAL DISC USING MULTIGENERATION CONSTITUTIVE MODELING IMPROVES MODEL PREDICTIVE CAPABILITIES IN MULTIAXIAL LOADING	79
7 CONCLUSIONS AND FUTURE WORK	99
REFERENCES	108
Appendix	
A PERMISSIONS	122

LIST OF TABLES

Table 3-1: Summary of Sample Set for CEP MRI Study.....	22
Table 4-1: Summary of Sample Set for CEP Mechanical Properties Study	39
Table 4-2: Summary of Mechanical and Biochemical Properties for Healthy and Degenerate CEP.....	43
Table 5-1: Summary Results	65
Table 6-1: Properties for the Finite Element Model.....	85
Table 6-2: Comparison of Multiaxial Stiffnesses Between Experimental Data, the Swelling Model, and the Multigeneration Model.....	94

LIST OF FIGURES

Figure 2-1: Overview of disc anatomy	5
Figure 3-1: Accuracy of the CEP MRI technique	23
Figure 3-2: Measurement technique for CEP thickness	25
Figure 3-3: Success of MRI technique and rater performance	27
Figure 3-4: CEP thickness across the anterior-posterior width of the disc	28
Figure 3-5: Relationships between CEP geometry and age	29
Figure 3-6: Relationships between CEP geometry and degeneration measured by T2 relaxation time.....	30
Figure 3-7: Relationships between CEP geometry and disc geometry	31
Figure 4-1: Schematic of the sagittal section of the intervertebral disc	39
Figure 4-2: Finite element model geometry and mesh.....	42
Figure 4-3: Relationships between CEP mechanical properties and degeneration and age.....	44
Figure 4-4: Histological assessment of non-degenerate and degenerate CEP	45
Figure 4-5: Relationships between CEP properties and biochemical content.....	47
Figure 4-6: Performance of the fiber-reinforced CEP model	47
Figure 4-7: Effect of CEP fiber-reinforcement on local and disc-level mechanical response to stress-relaxation loading.....	49
Figure 4-8: Schematic for transport and disc height changes with disc degeneration	56
Figure 5-1: Schematic of axes of disc loading	57
Figure 5-2: Overview of mechanical testing protocol.....	61

Figure 5-3: Representative lateral shear loading throughout multiaxial testing.....	64
Figure 5-4: Average load-displacement curves for slow rate multiaxial loading	66
Figure 5-5: Correlations between multiaxial stiffnesses and disc geometry	67
Figure 5-6: Off-axis response in all degrees-of-freedom throughout testing	69
Figure 5-7: Off-axis response for all degrees-of-freedom plotted against applied degrees-of-freedom.....	70
Figure 5-8: Magnitudes of amplitudes and offsets for the off-axis degrees-of- freedom.....	72
Figure 5-9: Relationships between amplitudes and offsets with disc geometry	73
Figure 6-1: Schematic of multigeneration modeling.....	88
Figure 6-2: Method for multigeneration deposition of collagen fibers	88
Figure 6-3: Example load-displacement curves for each degree-of-freedom	90
Figure 6-4: Parameter selection results for multigeneration parameters.....	91
Figure 6-5: Validation results for multiaxial loading	94

ABSTRACT

The intervertebral disc is a fibrocartilaginous tissue which provides flexibility and load support in the spine. The disc is composed of three substructures: a central and gelatinous nucleus pulposus surrounded by the fibrous lamellae of the annulus fibrosus and enclosed superiorly and inferiorly by the cartilage endplates. The structure and biochemical composition of these three constituents give rise to the non-linear, anisotropic, viscoelastic, and biphasic mechanical behaviors of the disc. Improving the ability to quantify disc biomechanics is essential to understanding the processes of aging and degeneration. Specifically, developing and validating computational modeling techniques to evaluate the relationships between disc degeneration and disc mechanics can inform on disc structure-function relationships, which will improve the accuracy of diagnoses, and aid in design of therapeutic interventions.

Finite element models are valuable tools for quantifying the complex mechanics of the disc, however their formulation and validation are complicated by disc geometry, the complex constitutive models required for mechanics of the disc sub-structures, and technical requirements for multiaxial experimental testing. Historically finite element models have therefore been limited in their model development and validation. Our lab recently developed and validated a finite element

model of the disc for compressive loading, however this model was not validated in multiaxial loading.

The overall objective of this dissertation was to further develop and validate a finite element model of the disc by incorporating residual stresses and validating the model against experimental multiaxial mechanical data. To achieve this objective, the mechanical properties and anatomy of the cartilage endplate were added to a finite element model of the human disc, a multiaxial experimental dataset was generated, and a novel multigenerational constitutive modeling approach was used to add residual stresses to the model. The outcome of this thesis is a finite element model with predictive capabilities in multiaxial loading.

Chapter 1

INTRODUCTION

The intervertebral disc is a fibrocartilaginous tissue which provides flexibility and load support in the spine. Normal function of the disc is compromised by aging, disc degeneration, or injury [1-3]. Disc degeneration is strongly correlated with low back pain and loss of quality of life. Improving our ability to quantify disc biomechanics is essential to understanding the processes of aging and degeneration. Specifically, developing and validating computational modeling techniques to evaluate the relationships between disc degeneration and disc mechanics can inform on disc biomechanics, improve the accuracy of diagnoses, and aid in design of therapeutic interventions.

The overall objective of this work is to improve and validate a 3D finite element model of human L4-L5 intervertebral discs by quantifying disc anatomy and mechanics. To this end, in this dissertation I will combine mechanical testing, magnetic resonance imaging (MRI), and constitutive modeling to accomplish this objective. In addition to further developing and validating the disc FE model, I will address basic science questions related to disc constituent geometry and mechanics, and disc 6 degree-of-freedom (multiaxial) mechanics. In Chapter 2 the relevant background information for this work to summarize the significance of this work. In

Chapter 3, cartilage endplate (CEP) geometry will be evaluated using a non-invasive magnetic resonance imaging (MRI) technique and relationships between CEP geometry and aging and degeneration will be established. This chapter will validate the technique as a viable tool for non-invasively determining CEP geometry as well as quantify CEP geometry as an input for FE models. In Chapter 4, CEP mechanical properties will be quantified using confined compression and biphasic-swelling constitutive modeling. Relationships between CEP properties and degeneration will be quantified and properties will serve as inputs to disc FE models. In Chapter 5, a novel dataset of intervertebral disc 6 degree-of-freedom (DOF) mechanics and coupled motion will be quantified and serve as validation metrics for the FE model. In chapter 6 I will present the validation of the disc FE model against the multiaxial data by including a novel multigeneration constitutive modeling approach to incorporate prestress in the AF collagen fibers. Finally, in Chapter 7 I will summarize the conclusions of this work and identify future directions for these techniques.

Chapter 2

BACKGROUND

2.1 Clinical Significance

Low back pain (LBP) is a debilitating condition affecting over 60% of the adult population in the United States [1]. LBP is the second most frequent reason for a physician visit, permanently disables more than 5 million Americans, and results in approximately \$100 billion in direct and indirect costs annually [4]. LBP can be acute or chronic and is related to several underlying pathologies including herniated discs [5], muscle strain [6], osteoarthritis [7], spinal stenosis [8], compression fractures [9], and disc degeneration [7]. These various pathologies, particularly disc degeneration, are strongly associated with altered joint biomechanics and mechanical loading [2, 10-12]. Current medical treatments for addressing LBP are often invasive surgeries which can result in limited flexibility and motion and degeneration of the adjacent discs. For example, a common procedure, fusion of the adjacent vertebrae, is often successful at alleviating pain, but eliminates motion of the joint [13]. The adjacent vertebrae and discs are required to carry the increased motion demands and may lead to degeneration of the adjacent discs [14]. Effective treatment is further hindered by difficulties identifying the problematic disc or discs to target for intervention as multiple discs in a

given spine may present as degenerated but each disc may not contribute equally to pain symptoms.

2.2 Intervertebral Disc Structure and Composition

The intervertebral disc is the largest avascular tissue in the body and is highly-organized to permit flexibility in the spine, dissipate energy, and support multi-axial loads. The disc is composed of three sub-structures: a gelatinous central nucleus pulposus (NP) surrounded by the fibrous rings of the annulus fibrosus (AF) and is separated from the adjacent vertebrae by the cartilage endplates (CEP) (Figure 2-1)[15]. The primary component of all three sub-structures is water, composing 70-80% of the NP [10, 16], 50-70% of the AF [17], and 55-65% of the CEP [18]. The primary components of the extracellular matrix of the disc are proteoglycans (10-50 %) and collagens (20-70 %) [17, 19-21]. While all 3 sub-structures contain proteoglycans and collagens, the types, quantity, and arrangement of these biochemical constituents vary with each sub-structure. Notably, the NP contains the highest fraction of proteoglycans by dry weight (50%) while the AF (15%) and CEP (10%) have comparably modest proteoglycan content by dry weight [16, 18, 22, 23]. The AF has the highest collagen content (60%) while the NP and CEP have approximately 20%. The disc is also sparsely cellular, with a cell density of $4 \times 10^6/\text{cm}^3$ in the NP, $9 \times 10^6/\text{cm}^3$ in the AF, and $15 \times 10^6/\text{cm}^3$ in the CEP [24]. In particular, the cells at the center of the NP are the furthest in the body (8 mm) from their nearest vascular supply in the capillary beds of the adjacent vertebrae [2, 25].

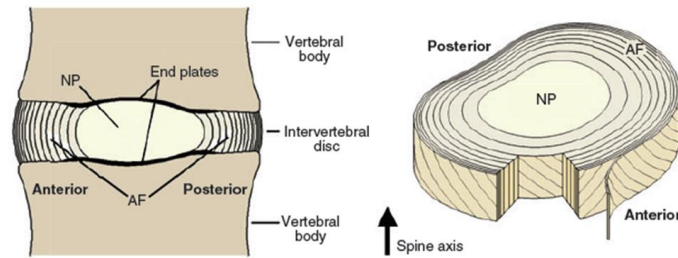


Figure 2-1: Schematic of disc anatomy in the (A) mid-sagittal plane and (B) three-dimensional view illustrating AF lamellar structure adapted from Smith et al. 2011.

In addition to varying quantities of biochemical constituents, the structural arrangement of these biochemical constituents varies among the disc sub-structures. The NP covers approximately 30% of the axial area of the disc [26] and is largely disorganized with randomly arranged collagen II fibrils dispersed through the proteoglycan-rich extracellular matrix. In contrast, the AF is highly organized into 15-25 concentric lamellae of alternating fiber angles to the transverse plane at approximately $\pm 40^\circ$ in the AF lamellae closest to the NP (inner AF) and $\pm 25^\circ$ in the periphery of the disc (outer AF) [27]. In addition, the collagen fibrils in the inner AF are largely type II collagen whereas the collagen fibrils in the outer AF are largely type I collagen [28]. The proteoglycan content of the AF also changes radially from the inner AF to the outer AF, where the proteoglycan content is approximately 40% of the dry weight of the inner AF and 15% of the dry weight in the outer AF [17]. The CEP covers the NP as well as some of the inner AF and has type II collagen oriented randomly but parallel to the adjacent vertebrae with some collagen fibrils oriented parallel to the fibers of the inner AF where the two tissues intersect [29]. Ultimately,

the differences in composition and structure among the disc constituents give rise to each sub-structure's unique contribution to overall disc mechanics.

2.3 Degeneration

With age the disc undergoes a cascade of biochemical changes resulting in disorganization of the disc structure and altered mechanical function of the disc. A hallmark of this degenerative process is the loss of proteoglycan content within the NP from approximately 50% in the normal disc to below 30% in the degenerated disc [2, 16, 17]. Similarly, the water content of the NP decreases from 80% in the normal disc to below 65% in the degenerated disc [2, 17], making the boundary between the NP and AF difficult to detect using conventional imaging techniques such as MRI. These changes also make the NP more fibrotic, less gel-like, and stiffer, compromising its mechanical role in the disc as greater loads are transferred to the AF in the degenerated disc, altering its loading environment. It is hypothesized that the altered loading environment of the AF can lead to local failure of the tissue in the form of radial and circumferential tears [30, 31].

The disc possesses limited ability to repair damaged tissue due to its sparse cellularity and distance from solute supply which may make tears precursors to herniation of the NP through the AF [12]. Moreover, altered loading in the AF may be linked to pain as local strains may increase in the outer AF, agitating pain receptors in that region. Additionally, the NP will have a reduced fixed charge density as proteoglycan and water contents decrease, causing the NP to recover less water, resulting in a loss of disc height with aging and degeneration. Another form of

herniation in the disc is the development of Schmorl's nodes, or a herniation of the NP vertically through the adjacent endplates and into the bone [32-35]. Unlike the soft tissue of the disc, the bone is able to repair itself when damaged and can heal in the area surrounding the herniated NP in the bone space [36]. Schmorl's nodes similarly lead to a reduction in intradiscal pressure and loss of disc height, but it remains unclear if they are associated with pain.

2.4 Disc Mechanics

Daily activity imparts multiaxial loads on the spine including compression, torsion, and bending and each constituent of the intervertebral disc has a unique function derived from its composition and structure and the combination of these individual structure-function relationships ultimately enables the disc to provide load support and permit flexibility in the spine [37-40]. The water and proteoglycan-rich NP serves to support axial compressive loads and expands outwards leading to circumferential hoop strain and stress in the AF [41, 42]. In addition, daily loading causes 20-25% of the disc's water content to be expressed and the NP's high proteoglycan content leads to the generation of osmotic pressure and permits overnight recovery of the water lost from daily loading [43]. The aligned collagen of the AF lamellae provide load support in rotational degrees of freedom (e.g. torsion, bending, and flexion), which impart significant tensile stress to the AF [37, 44-46]. Additionally, rotation of the lamellae during loading generates significant shear forces at the lamellar boundaries, further providing load support [47]. The unique anatomy

and biochemistry of the disc substructures is optimized to enable the disc to perform its multiaxial load-bearing functions. While it is widely recognized that the disc supports multiaxial loads, there is limited mechanical data on the full multiaxial mechanics of the disc as often DOFs need to be tested separately due to the technical complexities required of mechanical testing equipment.

2.5 Biphasic Mechanics of the Intervertebral Disc

A defining characteristic of soft tissues such as intervertebral disc, articular cartilage, tendon, ligament, and arteries is that their mechanics are viscoelastic, or time-dependent; under a constant deformation the tissues dissipate stress, a phenomenon called stress-relaxation, and under a constant load they continually deform, a phenomenon called creep. One mechanism of this behavior is termed “biphasic” and arises from the interaction of fluid and solid phases within the tissue, specifically movement of water through the porous solid matrix of the tissue which can be described using Darcy’s law:

$$\mathbf{w} = -\mathbf{k} \cdot \nabla p \quad (1)$$

Where \mathbf{w} is the fluid flux, \mathbf{k} is the tissue’s permeability, and p is the fluid pressure.

The tissue’s permeability arises from its composition and structure and describes the ability of water to move through the tissue. Mathematical modeling of tissue integrates this fluid flow behavior with solid matrix mechanics via a biphasic material model, where the tissue is modeled as a mixture of solid and fluid phases with a total stress ($\boldsymbol{\sigma}$) defined as:

$$\boldsymbol{\sigma} = -p\mathbf{I} + \boldsymbol{\sigma}^e \quad (2)$$

Where p is the fluid pressure, \mathbf{I} is the identity tensor, and $\boldsymbol{\sigma}^e$ is the elastic matrix stress. Quantifying biphasic material properties of NP and AF has been vital to elucidating structure-function relationships in the disc [16], effects of degeneration on disc mechanics [48-51], and serves as inputs for disc finite element models [52]. While there is detailed knowledge of biphasic properties in the NP and AF, the CEP's biphasic properties and their relationship with CEP structure, composition, and disc degeneration remain unknown.

2.6 Constitutive Models for Disc Tissues

To investigate the mechanics of the disc sub-structures, each tissue's stress-strain response from mechanical testing is curve-fit to constitutive models to acquire material properties. Constitutive models mathematically describe the nonlinear, anisotropic, viscoelastic, and biphasic behaviors of each sub-structure. Performing such analysis is useful not only for quantifying mechanical properties in the context of the experimental work but also serves as inputs for FE models of the disc. Common testing techniques for disc tissues include compression for NP [16, 53] and compression or tension for AF [48, 51, 54, 55] while mechanical testing of human CEP is limited to one study in tension [56] and one compression study on baboon CEP [57]. After performing the appropriate mechanical test, the resulting data is fit to a constitutive model.

Constitutive models can be either phenomenological or structural and both classes have been applied to disc tissues. Structural models incorporate characteristics of the tissue anatomy (e.g collagen fiber angle) to relate structure and mechanical function in the constitutive model, whereas phenomenological models simply describe the tissue's stress-strain relationship mathematically with no specific regard for the underlying tissue structure. Phenomenological models were first implemented to model the nonlinear response of tissues like arteries [58-60]. Prominently, the Fung-type model has been widely used to describe tissues such as AF [61], CEP [62], sclera [63], arteries [58], and duodenum [64]. While these models can describe the stress-strain behavior of a given tissue, they are not formulated with consideration to the underlying structure and composition of the tissue and therefore are limited in their ability to provide information on the structure-function relationships of tissues. Structural models aim to improve on phenomenological models by representing the contribution of collagen fibril's orientation, stiffness, distribution, and crimp to a tissue's mechanics. Often, these effects are represented using hyperelastic constitutive models defined by strain energy functions representing the fiber populations of the tissue. This approach is advantageous in that the contributions of each structural component can be accounted for in the overall stress-strain response. In particular, the matrix of tissues can be modeled using a total strain energy function (Ψ) that is defined by the summation of the strain energy of the extra-fibrillar matrix (Ψ_M) and the strain energy of the fibers (Ψ_F).

$$\Psi = \Psi_M + \Psi_F \quad (3)$$

Typically, for both analytical modeling and FE modeling, the NP is modeled without the effects of collagen fibers while the AF is modeled using two fiber families at alternating orientations [65]. To date there are no analytical modeling studies on human CEP and few FE models include CEP.

The elastic stress in the tissue can be determined from the strain energy density by the relationship:

$$\boldsymbol{\sigma} = \frac{2}{J} \mathbf{F} \cdot \frac{\partial \Psi}{\partial \mathbf{C}} \cdot \mathbf{F}^T$$

Where \mathbf{F} is the deformation gradient tensor, \mathbf{C} is the Right Cauchy-Green deformation tensor, and J is the Jacobian of the deformation gradient. In addition to the elastic stress of the tissue, the osmotic swelling effects of proteoglycans can be accounted for by defining a relationship between fixed charge density and osmotic pressure, and therefore the definition of the total stress in the tissue to

$$\boldsymbol{\sigma} = -(p + p_{\text{OSM}})\mathbf{I} + \boldsymbol{\sigma}^e \quad (4)$$

where p_{OSM} is the osmotic pressure. The specific constitutive models used to model the matrix, fibers, and osmotic effects of intervertebral disc tissues will be discussed in Chapters 4 and 6.

2.7 CEP Structure and Mechanics

The CEP supports the bone-disc interface, containing the NP while permitting the transport of water, solutes, and waste products across the interface [25]. The geometry

and mechanical properties of the CEP are likely optimized to support competing demands. For example, the CEP must be thick enough to provide mechanical support of the disc-bone interface but also be thin enough to minimize the distance solutes must travel en route to the cells in the center of the disc. The role of the CEP's geometry and mechanical properties in the disc and their changes with disc degeneration will be discussed in Chapter 3.

Despite the wealth of knowledge regarding changes in NP and AF composition and structure and their effects on tissue function with degeneration, changes in CEP composition, structure, and function with degeneration remain unknown. Quantifying changes in CEP with degeneration is important as it may elucidate the overall disc degeneration cascade and may be a predictor of disc degeneration. In particular, two competing hypotheses for disc degeneration are related to CEP transport properties (e.g. permeability), which remain unknown. If CEP permeability increases with degeneration, water will more readily leave the disc and will result in reduced disc height and lower water content observed in the NP with degeneration. However, if CEP permeability decreases with degeneration, the cells in the NP, which already reside in an environment poorly suited for solute transport, will not be able to receive solutes and expunge waste products as readily [66]. Human CEP permeability properties and their changes with degeneration remain unknown and will be explored in Chapter 4 of this dissertation.

2.8 Disc Motion Segment Testing

Identifying the mechanical behavior of the disc as a whole is often accomplished through testing of disc segments [40, 49, 67-71]. When testing one intervertebral disc, testing is performed on either functional spine units, a bone-disc-bone unit with posterior elements still attached, or disc motion segments, where the posterior elements have been removed [72, 73]. Testing can also be performed on multi-disc segments (e.g. L1-L5) with or without follower loads. For this dissertation emphasis will be placed on single-disc motion segment testing where the application of external loads does not result in load sharing between the disc and posterior elements. With this approach, emphasis is placed on the mechanics of the disc itself and not on the complex load sharing between disc and bone.

Prior to the application of external loads, the disc is often placed in 0.15 M PBS for up to 24 hrs to achieve hydration throughout the disc [74-77]. During testing it is important that discs remain hydrated as they will dehydrate with significant effects on mechanical properties. For example, discs that have been tested in air and not in a bath have reported higher stiffnesses in multiaxial loading which may be due to increased friction between lamellae due to dehydration [75]. Disc hydration is often preserved during testing by immersing the disc in a PBS bath during testing. However, over-hydration is a concern when performing tests in a saline bath as the disc can swell by 20% when immersed in a bath [78, 79]. Consequently, discs are often preloaded in axial creep [71, 80, 81] or preconditioned in cyclic compression [82, 83] before application of the intended loading conditions. If the intended loading condition is a degree-of-freedom other than compression, the compressive load may be held to

simulate body weight compression during loading. The magnitude of this compressive load is important as disc stiffness is dependent on the magnitude of the compressive load [84, 85].

After the disc is hydrated and preloaded or preconditioned, the intended loading scenario is performed. Historically axial compression has been evaluated extensively given the spine's prominent compressive load-bearing capacity. Testing has been performed in stress-relaxation [86], creep [67, 87], slow-ramp [67], and dynamic loading conditions [69, 70, 88]. Typical load curves obtained from these experiments show nonlinearity, time-dependence, and hysteresis in compression. Given that the disc experiences multiaxial loading physiologically, testing systems have been developed to apply rotational degrees-of-freedom (torsion, lateral bending, and flexion-extension) [45, 71, 89-91]. Similar to compression, rotation tests have demonstrated non-linearity and hysteresis [73]. Quantification of the multiaxial mechanics of the disc will be discussed in Chapter 5. Further, multiaxial mechanical data is particularly important to validate FE models of the disc as conventionally model validation is limited to compression while the disc experiences multiaxial loading.

2.9 Finite Element Modeling of Intervertebral Disc

Improvement of current treatment methods and development of new treatment methods is contingent on quantifying disc mechanics. To address this widely known relationship between mechanics and pain, disc mechanics have been thoroughly studied in the last 50 years, but these mechanical studies are often limited to ex vivo

testing of cadaveric or even animal tissue. Moreover, historical testing of cadaveric discs often focuses on disc-level mechanics (e.g. overall axial displacement, disc compressive stiffness, or reaction force) and often ignores the internal mechanics such as stress, strain, and fluid flow. Predicting internal mechanics is critical as regions of high stress/strain are likely locations for damage of the tissue, or failure of the treatment. Consequently, the finite element (FE) method has been increasingly used to predict internal disc mechanics. FE models of the disc should be constructed with proper disc structure, material models that appropriately represent the disc constituents, and must be extensively validated to ensure their utility.

Early disc FE models were limited computationally and were constructed from simple constitutive modeling approaches such as using linear elastic material properties for both NP and AF and attempted to model the anisotropy of the AF using orthotropic linear elastic material properties. Subsequent models would expand to model the tissues as biphasic materials and model the specific orientations of collagen fibers in the AF using tension-only rebar elements. Moreover, the constitutive models used for the matrices of NP and AF expanded to include hyperelastic models such as Mooney-Rivlin and Neo-Hookean. Additionally these models incorporated elements of deformation-dependent permeability. However, some models continue to exclude the contribution of CEP or use material models and properties that are not based on human CEP mechanical testing. While advances were made on extra-fibrillar matrix constitutive modeling, the contribution of AF fibers remained as cable elements. Often, disc models use a single fiber angle to represent the AF, while the in vivo disc

has a gradient in fiber angle from inner to outer AF. Similarly, material properties are assumed to be equal throughout the AF while the inner AF and outer AF are known to have different properties arising from their different biochemical contents. The FE model in Chapter 6 will address these historic limitations of disc FE models by incorporating CEP properties derived from human CEP mechanical testing and a novel AF modeling approach that reflects the gradient in properties from inner to outer AF.

While the constitutive models used for each disc tissue are important for model construction, FE models need to be thoroughly validated against the available mechanical data. Historically, model validation has been underdeveloped and uses metrics such as total displacement during creep, NP fluid pressure, and disc bulge from disc segment testing. Mechanical testing data of human tissue is notoriously variable and thus matching these metrics within one standard deviation can be easily achieved, particularly if the material properties are tuned to do so, and further these approaches ignore any transient behavior of the disc. Given that the disc rarely is at equilibrium in vivo, and undergoes various changes in loading state throughout daily activity, it is imperative that validation approaches target metrics such as dynamic loading profiles, transient relaxation or creep curves, as well as multiaxial stiffnesses. These metrics will be used for FE model validation and discussed in greater detail in Chapter 6.

2.10 Residual Stress in the Intervertebral Disc

Residual stress is the internal stress of a tissue in the absence of externally applied loads [92]. Residual stresses and strains exist in all soft tissues and were first

demonstrated in arteries when a radial cut was placed through the arterial wall, causing an opening of the cross-section [93, 94]. The addition of a second radial cut produced no appreciable change in tissue configuration, demonstrating that the opening due to the first cut truly created a stress-free configuration [95]. This opening-angle method was pioneering work in quantifying residual stresses and strains in soft tissue and has been applied to bovine AF [96]. The opening-angle behavior was observed in AF samples with a radial cut demonstrating the existence of circumferential hoop stresses and strains in the absence of external loads [96, 97].

Soft tissue residual stresses arise from osmotic swelling and fiber pre-stress due to growth and remodeling [92, 98, 99]. Swelling residual stresses arise from osmotic pressure induced by the negatively charged glycosaminoglycans of the tissue which result in water imbibing. The water movement into the tissue results in tension of the solid matrix and thus, residual stresses. Swelling is known to play an important role in disc mechanics by restoring hydration of the NP and imparting circumferential stress in the AF and therefore disc FE models routinely include the contribution of swelling [76]. While these techniques are able to capture the swelling of an intact cadaveric disc, the additional residual stresses arising from fiber pre-stress remain unaccounted for in FE models. A method to generate residual stresses and its implications on FE model validation will be discussed in Chapter 6.

2.11 Research Objectives

The overall objective of this work is to establish and validate a 3D finite element model of human intervertebral disc. The first objective of this dissertation was

to validate an MRI technique for measuring CEP geometry, which will serve as inputs for the FE model, and relate geometry to disc degeneration. To complete this research fast low-angle shot (FLASH) MRI imaging was used to quantify CEP geometry. The second objective was to quantify CEP mechanical and biochemical properties as inputs for a disc FE model and relate properties to degeneration. Confined compression mechanical tests and constitutive modeling were used to quantify CEP mechanical properties as inputs for the disc FE model. The third objective was to use a multiaxial hexapod loading device to acquire a dataset of multiaxial disc mechanics to serve as metrics for validation. The fourth objective was to validate the disc FE model in multiaxial dynamic loading by incorporating residual stress in the annulus fibrosus. To accomplish this, a novel multigeneration constitutive modeling strategy to account for AF residual stresses was incorporated into the FE model for validation.

Collectively, this work validates an MRI imaging technique for quantifying CEP geometry non-invasively, provides a unique dataset on multiaxial disc mechanics, and is the first to validate a disc FE model in multiaxial dynamic loading. This ensemble of techniques has significant potential to measure disc structure and quantify mechanics and future translation of these techniques could be used for patient-specific imaging and modeling. In particular, the FE model further developed and validated in this work will have unprecedented predictive capabilities due to its unique validation strategy incorporating experimentally-derived residual stress and comparing to a full dataset of multiaxial dynamic loading conditions.

Chapter 3

AIM 1 – MRI QUANTIFICATION OF HUMAN SPINE CARTILAGE ENDPLATE GEOMETRY: COMPARISON WITH AGE, DEGENERATION, LEVEL, AND DISC GEOMETRY

Geometry is important to the function of the intervertebral disc and changes in geometry are associated with disc degeneration and altered disc function. For example, disc height is critical to providing load support [100] and with degeneration and loss of hydration, the disc height decreases [30, 101] and disc axial area increases [102]. The nucleus pulposus and annulus fibrosus substructures also have well-defined geometries. For example, the nucleus pulposus occupies approximately 25% of the disc axial area [26] and the annulus fibrosus has a well-defined lamellar structure with decreasing fiber angle from the inner annulus fibrosus to the outer annulus fibrosus [27]. While the nucleus pulposus and the annulus fibrosus have well-known geometries, the cartilage endplate (CEP) does not. The CEP is a thin cartilaginous layer above and below the disc that separates the disc from the adjacent vertebral endplates and vertebral bodies. The CEP functions to transmit compressive loads across the disc-bone interface, pressurize the nucleus pulposus, and serve as a barrier for solute transport. The geometry of the CEP is critical to achieving these functions. The CEP must be thick enough to support the disc-bone interface by transferring compressive loads, while also being thin enough to minimize the distance solutes must

travel en route to the cells in the center of the disc [25]. The CEP also needs to cover enough axial area to reduce fluid flow and pressurize the nucleus pulposus. CEP geometry in the non-degenerate disc is presumably optimized to perform these functions.

With degeneration, however, the CEP permeability decreases, tensile modulus decreases, and it may become sclerotic, calcified, or even severely damaged by Schmorl's nodes [2, 34, 56, 66, 103-105]. While many CEP mechanical and compositional changes with degeneration are known, geometry of the CEP and changes with degeneration are not known. Indeed, there are conflicting findings in the few available studies that have measured CEP geometry. Histology demonstrated a decrease in CEP thickness with age [106] while resistance micrometry has shown an increase with age [107]. Additionally, histologic methods for assessing CEP geometry are not suitable in a clinical setting and only provide a 2D visualization of the tissue structure [18, 57]. Measuring CEP geometry and how it changes with degeneration is important, as it may elucidate the overall disc degeneration cascade and be a predictor of disc degeneration. Consequently, a three dimensional and non-invasive method to measure CEP geometry is needed.

Magnetic resonance imaging (MRI) techniques are appropriate for assessing CEP geometry as they are non-invasive and can provide strong contrast between adjacent tissues. Although the CEP cannot be visualized in routine clinical MRI, advances in MRI methods focusing on the CEP have aimed to identify CEP biochemical composition [62, 108], facilitate qualitative ultrastructural assessment

[109], and quantify CEP defects [110]. These improved MRI methods are derived from two MR sequences that have recently been applied to the CEP to enhance CEP visualization: ultrashort time-to-echo (UTE) [62] and fast low-angle shot (FLASH) [111]. In this study we apply the FLASH sequence because it is readily available on clinical scanners and usually requires shorter scan times for the same field-of-view and resolution [111]. Previously, we optimized the FLASH MRI sequence for CEP contrast and 3D visualization, providing proof of concept for measuring CEP geometry [111]. While this technique provided excellent CEP visualization and was validated against an excised cylindrical punch processed histologically, the accuracy and repeatability of the measurements were not assessed and only a small number of discs were analyzed.

The objectives of this study were to quantify CEP geometry in three dimensions using an MRI FLASH imaging sequence and evaluate relationships between CEP geometry and age, degeneration, level, and overall disc geometry. Specifically, we measured CEP width and area from a mid-axial image and CEP thickness from a mid-sagittal image. Additionally, to validate the CEP thickness measurement, we evaluated the accuracy and repeatability of the MRI-based technique compared to thickness measured in paired high resolution optical images taken after sectioning the disc.

Methods

Male lumbar motion segments ($n = 22$) from 9 human cadavers (age 60.9 ± 10.2 yrs; range 42-75 yrs, levels L1-L2 to L5-S1) were imaged using a Siemens 7T

MRI, as in [111] (Table 3-1). Both the superior and inferior CEP from each disc were imaged in 22 motion segments, although 1 segment only had 1 discernible endplate ($n = 43$ total CEP). Disc degeneration was graded using the Pfirrmann scoring system and by T2* relaxation time of the nucleus pulposus [105, 112]. Pfirrmann grade 2 was classified as non-degenerate while grades 3-4 were classified as degenerate. No grade 1 or 5 discs were present in the data set or used in this study. Enhancement of CEP contrast was achieved using a previously developed $200 \times 200 \times 200 \mu\text{m}^3$ 3D FLASH MRI technique. Imaging parameters were TR = 9 ms, TE = 3.7 ms, flip angle = 20° [111].

Table 3-1: Summary of Sample Set

Spine Level	Non-Degenerate CEP	Degenerate CEP
L1-L2	3	0
L2-L3	4	6
L3-L4	6	10
L4-L5	2	4
L5-S1	0	8
Total	15	28

Accuracy and Repeatability of CEP Thickness Measurement

The accuracy and repeatability of the CEP thickness measurement from the FLASH MR image were evaluated using paired high-resolution optical images of the CEP morphology taken after making a mid-sagittal section. Two discs that were imaged via MRI were selected for morphology analysis. Each disc was fixed in 10% formalin for 1 week and decalcified for 2 weeks with Formical-2000, refreshing the solution every 2-3 days. The discs were bisected along their mid-sagittal plane and imaged using a stereo dissecting microscope equipped with a high-resolution digital

camera (Leica Microsystems; Wetzlar, Germany). The corresponding mid-sagittal plane MRI image (Figure 3-1A) and morphology image (Figure 3-1B) were aligned and overlaid (Figure 3-1C) using OsiriX (www.osirix-viewer.com).

The MRI-morphology image pairs were evaluated by 2 raters, who each independently measured CEP thickness on the MR image and the morphology image on 4 separate days. Thickness was calculated as described in the following section. To assess the accuracy of the thickness measurement, the residual difference between the MRI and morphology measurements was calculated. To compare the slope of the raters' MRI-morphology measurements to a theoretically perfect 1:1 relationship, linear correlation was used with the y-intercept fixed to 0. To assess the repeatability for an individual user the coefficient of variation (CV) was used to analyze each rater's performance. CV is defined as the ratio of the standard deviation to the mean. The CV was calculated for each of the locations for each user. The average CV for each user was then compared. To assess inter-user error, the Bland-Altman test was used.



Figure 3-1: Accuracy of the CEP MRI technique. Mid-sagittal MRI (A) and morphology (B) images were resized and overlaid (C) to ensure that regions match in both images. In the merged image, red represents the MRI image and blue represents the morphology image. Scale = 5 mm.

Measurement and Analysis of CEP Axial and Mid-sagittal Geometry

The CEP thickness, anterior-posterior (A-P) width, lateral width, and axial area were measured in all discs by a single rater using a single measurement. CEP thickness was measured on the mid-sagittal plane of the disc using ImageJ. Thickness was calculated for 5 evenly-sized regions across each CEP using ImageJ (NIH) (Figure 3-2A). Within a region, the rater manually outlined the CEP using the polygon selection tool in ImageJ (Figure 3-2B) and converted the outline to a binary mask (Figure 3-2C). Thickness was calculated as the area of the mask divided by the width of the mask. Based on changes of thickness across the CEP (see results), thickness was further evaluated in three groups: center measurement, average of the anterior and posterior measurements (A/P), and the average of all five measurements. Axial CEP geometry (axial area, CEP A-P and lateral widths) was measured in the axial plane using OsiriX software. Due to the curvature of the disc-bone interface, MRI images were post-processed into thick mean intensity slabs of 1.5 mm and were used to calculate CEP axial geometry. Using a thick slab ensures that the full thickness of the CEP is accounted for when making measurements in the axial plane. In addition, total disc height and disc axial area were measured from the same sagittal and axial sections using OsiriX.

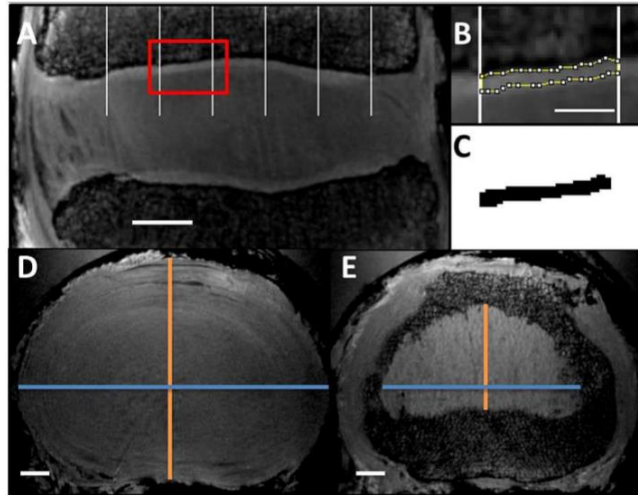


Figure 3-2: CEP thickness measurement technique. A CEP is divided into five evenly spaced regions (A). Using the polygon tool in ImageJ, the CEP of a particular region is outlined (B) and converted to a binary mask (C). The area of the mask is calculated in ImageJ and divided by the width of the mask to obtain thickness. Mid-axial plane (D) images were used to quantify disc axial geometry while a 1.5 mm thick axial slice (E) was used to calculate CEP axial geometry. Orange lines represent anterior-posterior width measurements while blue lines represent lateral width measurements. Scale = 5 mm.

Statistics

To determine if CEP thickness varies across the 5 measured regions, a one-way ANOVA with Tukey multiple comparison post-hoc test was performed. Within the full data set there are many factors (age, spine level, T2* score, Pfirrmann grade, disc height, and superior-inferior location) that may affect CEP geometry parameters (CEP axial area, A-P width, lateral width, center thickness, A/P thickness, average thickness), so reverse step-wise multiple regression analysis was performed using R software [113] to determine the effect of each predictor on CEP geometry. First, a full model including all factors was implemented. Factors were iteratively dropped from the model until either no factors were significant or all remaining factors were

significant. Factors were dropped in order of largest (most non-significant) p-value. Statistical significance was set at $p < 0.05$. This multiple regression procedure was performed for all CEP geometry measurements. To support interpretation of the correlations from the multiple regression procedure, for those factors that were significant, individual linear regressions were fit to each combination of factor and CEP geometry parameter to obtain individual r^2 and regression lines. To make comparisons between CEP geometry and disc geometry, linear regression was used to determine any significant correlations. To determine the percent of the disc covered by the CEP the ratio of (CEP geometry parameter) / (Disc geometry parameter) was computed for each CEP and averaged for the parameters of axial area, A-P width, and lateral width.

Results

Accuracy and Repeatability

Overall, independent raters produced accurate measurements between morphology and MRI images that match well with a perfect 1:1 relationship (slope = 1.01, 95% confidence interval of 0.97 to 1.04, Figure 3-3A). The average residual was 0.03 ± 0.14 mm. The standard deviation of this residual distribution was 0.14 mm, which is smaller than the 0.2 mm isotropic resolution of the MRI image, suggesting that the MRI-based method is an accurate measure of the thickness.

The repeatability, as measured by the coefficient of variation, was found to be 13.6% for rater #1 and 14.5% for rater #2. For a CEP thickness of 0.5 mm these repeatability measures equate to 0.068 mm and 0.073 mm, respectively, both of which

are below the MRI resolution. Sub-resolution error in repeatability for both raters suggests that both raters were able to produce consistent values when measuring a particular location. Therefore only one measurement, instead of 4, was used in the full dataset.

Inter-user error was assessed using the Bland-Altman test (Figure 3-3B, 3-3C). The bias for MRI comparisons (Figure 3-3B) was -0.049 ± 0.072 mm, with a 95% confidence interval of -0.19 to 0.09 mm. The bias for the morphology comparisons (Figure 3-3C) was -0.048 ± 0.092 mm, with a 95% confidence interval of -0.23 to 0.13 mm. There was no systematic inter-rater bias, therefore only one rater was used for the full dataset.

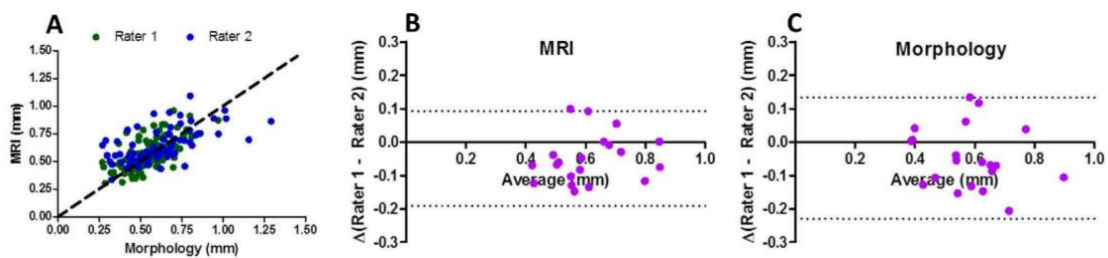


Figure 3-3: Success of MRI technique and rater performance. The MRI technique successfully predicts morphology thickness (A) with a slope of 1.01 with a 95% confidence interval of 0.97 to 1.04. Raters consistently matched MRI (B) and morphology (C) measurements. Each point in (A) represents one measurement at one location. Each point in (B-C) represents the average of all 4 measurements at each location.

CEP Mid-sagittal and Axial Geometry

CEP thickness was greater in anterior and posterior locations than in the center of the disc (Figure 3-4, $p < 0.01$). Therefore three thickness parameters were compared to sample age, degeneration grade, and disc geometries: CEP thickness (averaged

across the entire width), center CEP thickness, and A/P thickness (averaged from the anterior and posterior site).

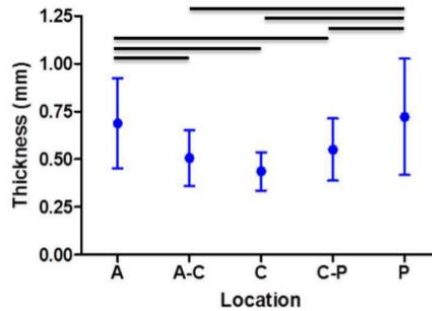


Figure 3-4: CEP thickness varied significantly across the anterior-posterior width of the disc ($p < 0.05$). CEP is thinnest in the center and thickest at the A/P ends, where the CEP interfaces with the inner annulus fibrosus. Bars represent $p < 0.05$. A = anterior, A-C = anterior-center, C = center, C-P = center-posterior, P = posterior.

With an established technique for measuring CEP thickness from MR images, the full dataset of 22 discs was evaluated for CEP geometry and evaluated via multiple regression. While center thickness did not correlate with age (Figure 3-5A, $r = -0.04$, $p > 0.05$), the A/P thickness (Figure 3-5B, $r = -0.40$, $p < 0.01$) and average thickness (Figure 3-5C, $r = -0.44$, $p < 0.01$) both decreased with age. CEP axial area (Figure 3-5D, $r = -0.37$, $p < 0.05$) and lateral width (Figure 3-5F, $r = -0.42$, $p < 0.01$) both decreased with age while A-P width (Figure 3-5E, $r = -0.25$, $p > 0.05$) did not correlate with age. No CEP geometry parameters correlated with degeneration measured by T2* (Figure 3-6) or Pfirrmann grade.

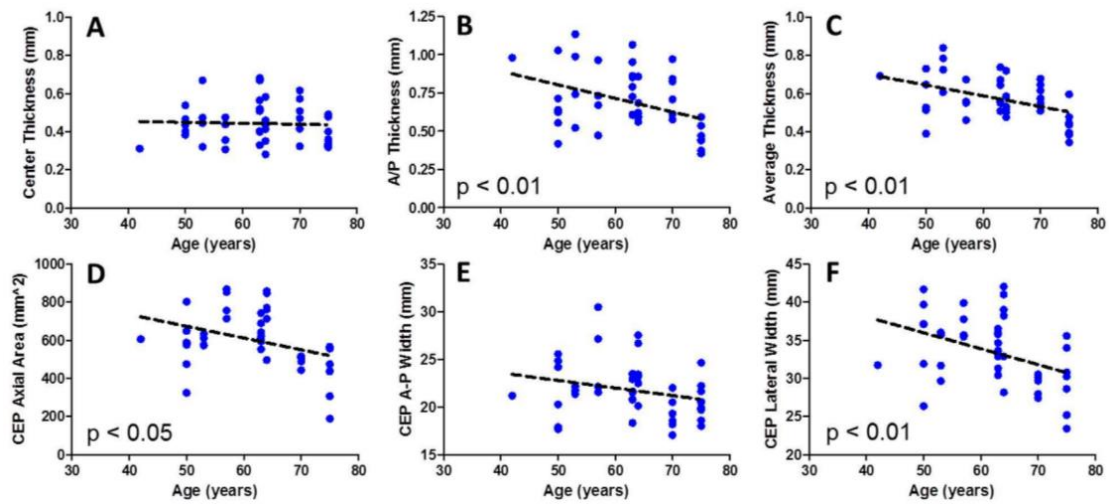


Figure 3-5: Relationships between CEP geometry and age. Center thickness (A, $r = -0.04$, $p > 0.05$) and CEP A-P width (E, $r = -0.25$, $p > 0.05$) did not correlate with age. A/P thickness (B, $r = -0.40$, $p < 0.01$) and average thickness (C, $r = -0.44$, $p < 0.01$) decreased with age. CEP axial area (D, $r = -0.37$, $p < 0.05$) and lateral width (F, $r = -0.42$, $p < 0.01$) decreased with age.

No CEP thickness parameter varied with disc level. CEP axial area did not vary by disc level, except L3-L4 CEP axial area was 35% greater than the L5-S1 CEP area ($p < 0.05$). Similarly, CEP anterior-posterior width didn't vary with disc level, except the anterior-posterior width was 20% greater in L3-L4 than L4-L5 ($p < 0.05$). CEP lateral width did not vary with disc level. No CEP geometry factor depended on

superior-inferior location.

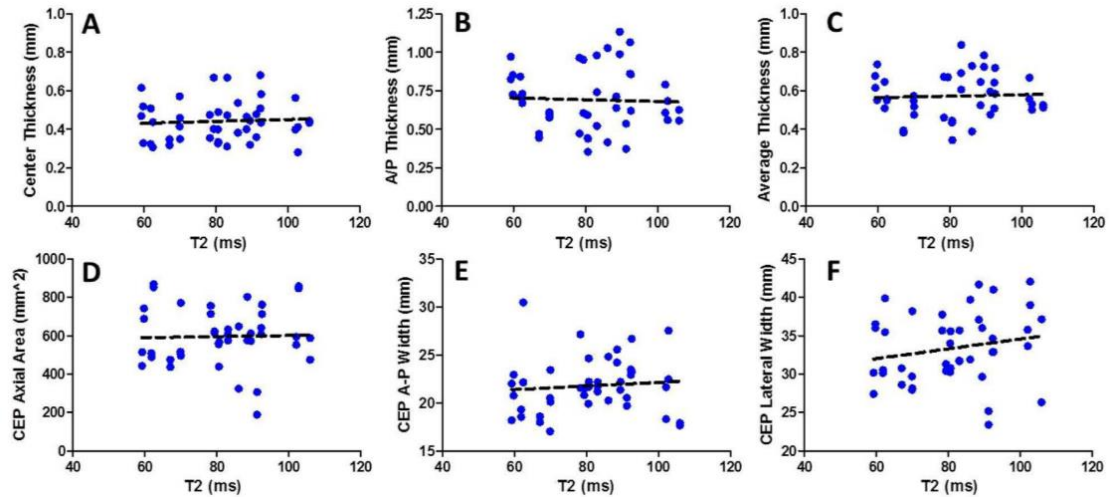


Figure 3-6: Relationships between CEP geometry and degeneration measured by T2* relaxation time. No CEP geometry parameter correlated with degeneration.

In comparing CEP geometry with its associated disc geometry, surprisingly, no CEP thickness parameter correlated with disc height (Figure 3-7A-C). CEP axial area did correlate with disc axial area (Figure 3-7D, $r = 0.47$, $p < 0.01$) and has a CEP axial area/disc axial area ratio of $30.9 \pm 7.0\%$. CEP anterior-posterior width significantly correlated with disc anterior-posterior width (Figure 3-7E, $r = 0.31$, $p < 0.05$) and a CEP A-P width/disc A-P width ratio of $56.1 \pm 7.5\%$. CEP lateral width correlated with disc lateral width (Figure 3-7F, $r = 0.32$, $p < 0.05$) and a CEP lateral width/disc lateral width ratio of $57.4 \pm 7.6\%$.

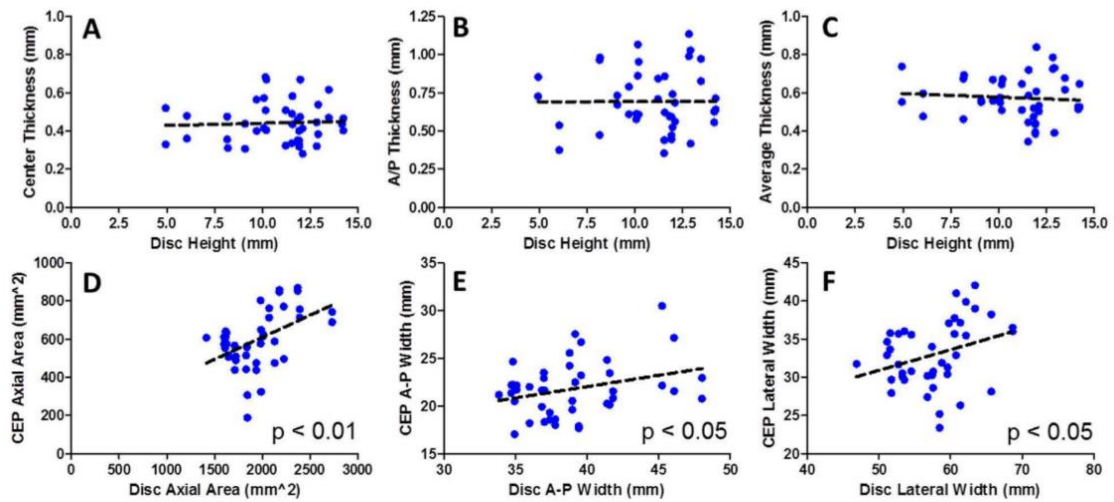


Figure 3-7: Linear regression relationships between CEP geometry and disc geometry. No CEP thickness parameter correlated with disc height (A-C). CEP axial area (D, slope = 0.23, $p < 0.01$), A-P width (E, slope = 0.24, $p < 0.05$), and lateral width (F, slope = 0.27, $p < 0.05$) all correlated with their disc counterparts.

Discussion

The objective of this study was to quantify CEP geometry in three dimensions using an MRI FLASH imaging sequence and evaluate relationships between CEP geometry and overall age, degeneration, spine level, and disc geometry. Previously we presented the MRI technique as a possible tool to visualize and measure CEP geometric features [111]. In the present study the accuracy and repeatability of the MRI technique was determined by comparing paired MRI and morphology based measurements. The 3D MRI technique yielded CEP thicknesses that were accurate with respect to paired morphology thickness and between raters. Importantly, there was no systematic over- or under-prediction of the CEP thickness by the MRI technique. Moreover, the validation procedure demonstrated differences in

repeatability and inter-user error that were lower than the MRI resolution ($< 0.2\text{mm}$). Therefore only one user making one measurement is required, enabling practical measurement of a larger data set. The excellent repeatability and low inter-user errors are likely due to the fact that this MRI technique offers significant contrast between the CEP and the surrounding bone and nucleus pulposus (Figure 1A), a feature that is traditionally best seen in histological assessment of the disc, where the CEP and surrounding tissues stain for significantly different biochemical content. Furthermore, the validity of the MRI technique is reinforced by the fact that measurements of CEP thickness presented here, 0.3-1 mm, are comparable to previous measurements produced using histology: 0.4mm-0.8 mm [18, 114, 115]. This FLASH MR imaging and analysis technique, if modified for clinical feasibility as previously demonstrated [111], will be valuable for assessing CEP geometry changes in patients with disc-related disorders.

This study evaluated changes in CEP geometry with age and degeneration. There were no significant correlations between any CEP geometry parameter and measures of degeneration, either T2* score or Pfirrmann grade, although several parameters were correlated with age. A/P thickness, average thickness, axial area, and lateral width were observed to decrease with age (Figure 5). It is unclear what processes lead to a smaller CEP and what significance a smaller CEP has on its structural, mechanical, and transport functions. A smaller CEP will provide less exchange area for transport of solutes and water, and may affect the transport cycle. Altered transport is often hypothesized to be a factor in the degenerative cascade [2,

24, 116, 117]. If smaller CEP axial area is significantly able to hinder transport, it is possible that using MRI to evaluate CEP axial area may be a valuable predictor of the efficacy of non-invasive therapies that require transport into the disc.

Furthermore, the changes in CEP geometry with aging are seen most prominently at the interface between the inner annulus fibrosus and the CEP (Figure 5B), a site of common CEP and annulus fibrosus herniation [115]. In this region, the CEP is thickest, likely due to annulus fibers passing through the CEP and anchoring to the adjacent bone [118, 119] which are not present in the center of the CEP [29, 105]. This may be a mechanically important junction in the disc as it experiences high tensile strains [49, 86, 120] and consequently, is frequently the sight of CEP and annulus fibrosus herniation [115, 121-123]. CEP thickness at this junction decreases with age which may make the CEP more susceptible to tensile failure. CEP axial area, which is enclosed by this outer boundary, also decreases with age. These age-related, but not degeneration-related, changes in geometry at the CEP-inner annulus interface suggest that the CEP may undergo a process of degeneration that doesn't directly follow disc degeneration [105].

Absence of significant correlations between CEP geometric parameters and measures of disc degeneration may also be due to the differences between disc degeneration and other cartilage degenerative processes like osteoarthritis. Notably, osteoarthritis results from increased wear of articular cartilage [124, 125], culminating in bone-on-bone contact. In contrast, the disc undergoes changes that manifest in altered structure and mechanics [3, 49, 67], but not wear. Disc degeneration is

typically not defined by bone-on-bone contact [7] and only in severe degeneration (Pfirrmann grade of 5) would wear possibly occur. No grade 5 discs were tested in this study and, due to fragmentation of the CEP in grade 5 discs, it would be challenging to visualize the CEP in such advanced degeneration using MRI. These different processes of articular cartilage wear and CEP changes with disc degeneration further confirm that the CEP is not a strict analog of articular cartilage.

CEP geometry correlated with disc geometry, as expected. Larger discs had larger CEP axial area and widths (Figure 7). The CEP had an axial area that occupies about 25-35% of the disc area, corresponding to a region encompassing the nucleus pulposus (~25% disc area) and some of the inner annulus fibrosus [26]. A larger CEP axial area than nucleus pulposus axial area is important for the CEP's functions in the disc. The CEP serves as for the interface for transport exchange as well as a load distributor between the disc and bone [25]. Both functions are successfully achieved by having a CEP axial area that covers the entire nucleus pulposus.

Surprisingly, particularly as CEP axial geometry correlated with disc axial geometry, the CEP thickness did not correlate with disc height. This may be valuable for the transport functions of the CEP. Taller discs are already burdened with a long diffusion distance from the vertebral solute supply to the cells in the center of the disc [25, 116, 117, 126]. If CEP thickness increased with disc height, this burden would only increase, particularly as the CEP has a high fixed charge density and a low permeability [18, 105].

This study is not without limitations. A small ($n = 22$) sample set was used to identify relationships between CEP geometry and disc geometry and disc degeneration factors. A priori power analysis suggested a minimum sample size of 98, at a power of $1-\beta = 0.8$, in order to compare across six factors. It is possible that such a large dataset would identify some correlations not detected here; however, it is not likely or expected that different outcomes would emerge. For example, in this study several CEP geometry factors, e.g. center thickness, shared no relationships ($p>0.9$) with disc degeneration (Figure 6), a fact that would not change with an increased sample size.

This study demonstrates the accuracy of measuring CEP geometry from 3D FLASH MRI. This technique was used to show a decrease in CEP axial geometry and A/P thickness with age. Age-related decreases in these geometric features may be related to commonly observed failure at the junction between the CEP and inner annulus fibrosus. The lack of relationship between CEP geometry and disc degeneration further suggests that CEP degeneration may not progress directly with disc degeneration. Consequently, it remains unclear what relationship the CEP shares with disc degeneration and low back pain. Nevertheless, as the CEP undergoes significant geometric changes with age, the MRI technique presented in this study may prove a useful diagnostic tool for clinical use.

Chapter 4

AIM 2 – HUMAN CARTILAGE ENDPLATE PERMEABILITY VARIES WITH DEGENERATION AND INTERVERTEBRAL DISC SITE

Degenerative disc changes in the nucleus pulposus and annulus fibrosus are well documented, but cartilage endplate (CEP) mechanical properties and how they change with degeneration remain unknown. The CEP is a 600-1000 μm layer of hyaline-like cartilage that separates the disc from the adjacent vertebral endplates and consists largely of type-II collagen, proteoglycans, and water [2, 111]. The CEP functions to transmit compressive loads, contain and pressurize the nucleus pulposus, and transport water, nutrients, and waste into and out of the disc. These functional roles have been qualitatively described but have been poorly explored quantitatively, particularly with degeneration. Quantifying the CEP mechanical properties and its changes with degeneration is essential for understanding how the CEP contributes to the function and pathology of the disc. Therefore the objectives of this study were to quantify the effect of disc degeneration on human CEP mechanical properties, determine the influence of superior and inferior disc site on mechanics and composition, and simulate the role of collagen fibers in CEP and disc mechanics using a validated finite element model.

Disc degeneration may be associated with altered CEP mechanical and transport properties. Decreased transport from the vascularized vertebral body, across the CEP, and into the nucleus pulposus may result in insufficient nutrition to its cells [66, 127, 128]. Structural damage decreases CEP tensile modulus [56]. However, the effect of degeneration on CEP compressive properties is unknown. Degeneration may affect the CEP's functions, which may be reflected in changes in mechanical properties. We recently applied confined compression to measure the extrafibrillar compressive properties of non-degenerate CEP [52]. Thus, the first objective of this study was to quantify the CEP mechanical properties in confined compression and how disc degeneration alters these properties.

Damage to the CEP can result in herniation of the nucleus pulposus through the vertebral endplate, known as Schmorl's nodes [32]. Schmorl's nodes cause a decrease in disc pressure, loss of disc height, and can result in vertebral body inflammation [35]. The prevalence of Schmorl's nodes is not symmetric; they occur more frequently across the inferior than the superior endplate [34]. This prevalence may be related to differences in superior and inferior vertebral bone properties, [129, 130] but may also be related to differences in CEP properties. Therefore, the second objective of this study was to determine the influence of disc site (i.e., inferior/superior) on human CEP mechanics and composition.

Finite element modeling is a valuable tool to study the role of the CEP in disc mechanics and transport. Essential to a successful finite element model is the choice of constitutive models and material properties for each tissue. Of the few disc finite

element models which have included the CEP, many have modeled it as a poroelastic material with an isotropic linear elastic solid matrix [127, 128, 131-133]. However the CEP constitutive formulations used have neglected non-linearity that may arise due to collagen fibers. Therefore, the third objective of this study was to model the CEP using measured CEP extrafibrillar matrix and permeability properties and evaluate the role of fiber alignment and mechanical properties.

Methods

Sample Preparation and Biochemical Composition

Human lumbar disc segments (n=19; Table 4-1) were acquired (NDRI, Philadelphia, PA), imaged with MRI, and graded for degeneration by both the nucleus pulposus T2 relaxation time and the Pfirrmann grade [134]. The T2 relaxation time is a continuous variable suitable for correlation analyses and the Pfirrmann grade is an integer variable that is widely used and suitable for grouping samples for descriptive statistics. The T2 relaxation time and Pfirrmann grade are correlated with each other [134, 135]. Non-degenerate discs were defined by a Pfirrmann score of 1 and 2 while degenerate discs were grade 3. No grade 4 or 5 discs had CEP that was testable. The gender distribution was 7 female and 6 male with an age range of 46 to 80 years old, with an average age of 60 ± 12 . Samples from lumbar levels L1L2 and L2L3 were used for statistical analyses. Only a few discs from L3L4 and L4L5 had testable CEP so these were not included in averages or statistical analyses (Table 4-1). CEP samples were dissected from the central region above the nucleus pulposus (total n=34, L1-L5; Figure 4-1). Samples were tested in confined compression and biochemical

composition of adjacent tissue was measured via a DMMB assay [52]. Material properties were determined by optimizing the experimental load curve and biochemical composition using finite element software, FEBio, as described previously [52].

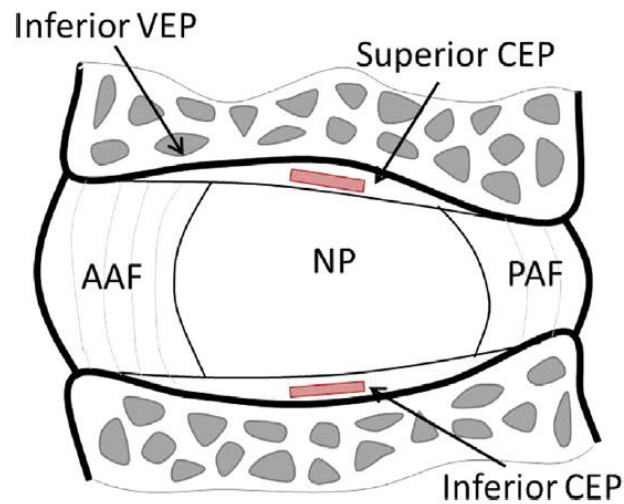


Figure 4-1: Sagittal section of the intervertebral disc showing location of CEP test samples taken adjacent to the nucleus pulposus (NP). *CEP: cartilage endplate, AAF: anterior annulus fibrosus, PAF: posterior annulus fibrosus, NP: nucleus pulposus*

Table 4-1: Summary of sample set by lumbar level. *Asterisks denote CEP samples that were excluded from mean calculations and statistical analyses

Lumbar level	Number of non-degenerate CEP	Number of degenerate CEP	Total number of CEP
L1L2	11	10	21
L2L3	4	5	9
L3L4	0	2*	2*
L4L5	2*	0	2*
Total	17	17	34

Statistics

The effect of disc site (Superior and Inferior) and degeneration (Nondegenerate Grade 1 & 2 and Degenerate Grade 3) was analyzed using a two-way ANOVA with

Wilcoxon matched-pairs signed-rank post hoc test for the effect of disc site and Mann-Whitney-U-test for effect of degeneration. The Pfirrmann scoring system is widely used and allows for grouping tissue samples into categories appropriate for the ANOVA, however, it is limited by its discrete nature. Therefore, a continuous parameter, the nucleus pulposus T2 time, [134], was used to evaluate the Pearson's correlation with all mechanical and biochemical parameters. Finally, correlation of age and CEP properties were also evaluated. Relationships between mechanical (permeability, modulus) and biochemical (fixed charge density, water) properties were analyzed using Pearson correlation.

Histology and Scanning Electron Microscopy

Additional spine segments (n=4) underwent histological examination of CEP fiber alignment and potential structural differences between non-degenerate and degenerate CEP. Segments were fixed in buffered 10% formalin and decalcified with Formical-2000. Decalcified bone-CEP-NP segments from the center of the disc were paraffin-embedded and 5 μm slices were cut. Samples were stained with Alcian blue and Picrosirius red to show proteoglycan and collagen, respectively. Additional slides were stained with only Picrosirius red and viewed over a polarized light microscope to show CEP fiber alignment. An additional, non-degenerate (Pfirrmann grade 2) disc was prepared for scanning electron microscopy (SEM). An NP-CEP-Bone plug was cored across the inferior CEP. The sample was digested in Chondroitinase ABC overnight to expose collagen fibers and cryosectioned to create a flat imaging plane. The sample was imaged using a Hitachi S4700 SEM.

Finite Element Modeling of CEP Mechanics

The full set of measured CEP Grade 3 extrafibrillar elastic, permeability, and swelling properties (Table 4-2), averaged for the superior and inferior locations, were incorporated into a validated Grade 3 finite element disc model [136]. Fiber properties, not available from confined compression experiments performed in this study, were obtained by fitting the tensile response from Fields et al [56] using an inverse finite element method. The average tensile response was fit to a biphasic-swelling model that was reinforced with an ellipsoidal fiber distribution. The ellipsoidal fiber distribution introduced two additional families of parameters, fiber modulus (ξ) and fiber nonlinearity (α) that are defined by an ellipsoidal distribution function [137]. This ellipsoidal distribution function was based on CEP polarized light histology and SEM, where fibers appear primarily oriented in the plane parallel to the vertebrae and nucleus pulposus and the anterior-posterior and lateral fiber directions were assumed to have the same fiber modulus (e.g. $\xi_1 = \xi_2$) while the contribution in the axial direction (ξ_3) was set at 10% of ξ_1 . Fiber nonlinearity was assumed to be independent of coordinate direction (e.g. $\alpha_1 = \alpha_2 = \alpha_3$). These assumptions reduce the ellipsoidal fiber distribution formulation to

$$\xi(\theta, \varphi) = \left(\frac{\sin^2 \varphi + 100 \cos^2 \varphi}{\xi_1^2} \right)^{\frac{1}{2}} \quad (5)$$

$$\alpha(\theta, \varphi) = \alpha_1 \quad (6)$$

To evaluate the performance of CEP fiber-reinforcement to local CEP mechanics, confined compression and uniaxial tension tests were simulated in FEBio and compared to compression and tension data. To evaluate the role of CEP fiber-reinforcement in overall disc mechanics, a disc compression simulation was performed. The simulated disc was hydrated to equilibrium for 24 hrs with the vertebral bodies fixed, which pressurized the disc [136]. After hydration, 10% axial compression was applied over 10 sec and held for 6.5 hrs to equilibrium. Disc reaction force, CEP strain, and CEP fluid flux data were calculated along the anterior-posterior axis of the mid-sagittal slice of the disc (yz -plane, Figure 4-2). Simulations were performed with and without including CEP fibers to evaluate the role of fibers in disc and CEP mechanical function.

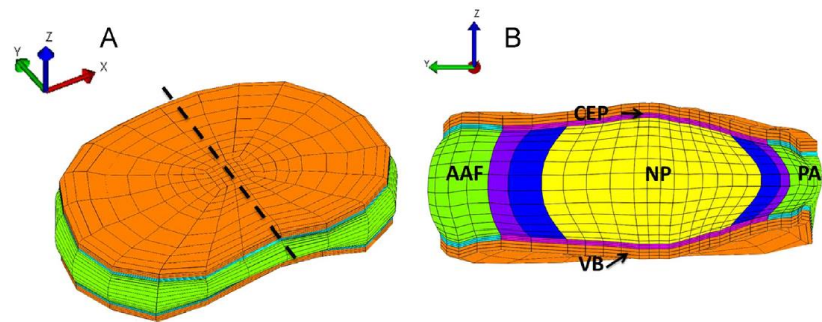


Figure 4-2: Finite element model geometry and mesh shown for (A) the full disc, and (B) the mid-sagittal section, cut at the dashed line in (A). The full disc is oriented such that the anterior-posterior disc axis coincides with the y -axis. The CEP mechanics were calculated along the yz -plane. *CEP: cartilage endplate, AAF: anterior annulus fibrosus, NP: nucleus pulposus, PAF: posterior annulus fibrosus, VB: vertebra*

Results

Composition

Average CEP GAG content across all CEP was 14.8% of the dry weight (n=30, Table 4-2) and was not different with degeneration or disc site ($p > 0.05$). Average water content across all CEP was 61.2% (n=30) and was also not different with degeneration or disc site. FCD did not significantly relate to degeneration as measured by the Pfirrmann scale but did correlate with degeneration measured by T2 time ($r = -0.36$, $p < 0.05$; Figure 4-3A). Although degenerative grade (Pfirrmann) and NP T2 time are both used to describe degeneration, they are defined differently, so it is not surprising that some parameters, e.g., FCD, are not affected the same way by these different measures of degeneration. FCD also did not increase with age ($r = 0.24$, $p > 0.05$; Figure 4-3D). Surprisingly, GAG and water content did not correlate with degeneration, but FCD, a function of both GAG and water content, increased with degeneration. GAG content was not correlated with water content.

Table 4-2: Summary of mechanical and biochemical properties (median, inter-quartile range) for healthy and degenerate CEP

	Non-degenerate (Grade 1 and 2)		Degenerate (Grade 3)		FE
	Inferior	Superior	Inferior	Superior	
<i>E</i> (kPa)	193 ± 58	308 ± 40	219 ± 118	227 ± 248	328
<i>v</i>	0.000 ± 0.183	0.200 ± 0.138	0.246 ± 0.066	0.342 ± 0.013	0.25
<i>β</i>	0.054 ± 0.480	0.416 ± 5.023	0.392 ± 0.516	0.224 ± 0.443	1.06
<i>H_A</i> (kPa)	193 ± 140	317 ± 199	181 ± 409	289 ± 329	–
<i>k₀</i> (mm ⁴ /N s)	0.000287 ± 0.000203 [◊]	0.000824 ± 0.000346*	0.000162 ± 0.000108	0.000306 ± 0.0000743 [#]	0.00025
<i>M</i>	3.786 ± 0.608	5.986 ± 2.340	3.077 ± 0.567	4.489 ± 2.334	3.9
Water (%)	57.2 ± 2.5	61.7 ± 3.5	61.1 ± 0.6	62.4 ± 4.1	62.3
GAG (%)	10.6 ± 3.0	10.5 ± 5.0	19.8 ± 4.5	16.3 ± 4.0	–
FCD (mM)	412 ± 76	241 ± 24	481 ± 29	275 ± 163	365

Key: modulus (*E*), Poisson's ratio (*v*), matrix nonlinearity parameter (*β*), aggregate modulus (*H_A*), permeability (*k₀*), permeability nonlinearity parameter (*M*), glycosaminoglycan (GAG), fixed charge density (FCD), finite element (FE).

* $p < 0.05$ vs. paired inferior sample.

[#] $p < 0.1$ vs. paired inferior sample.

[◊] $p < 0.1$ vs. degenerate samples from same disc site.

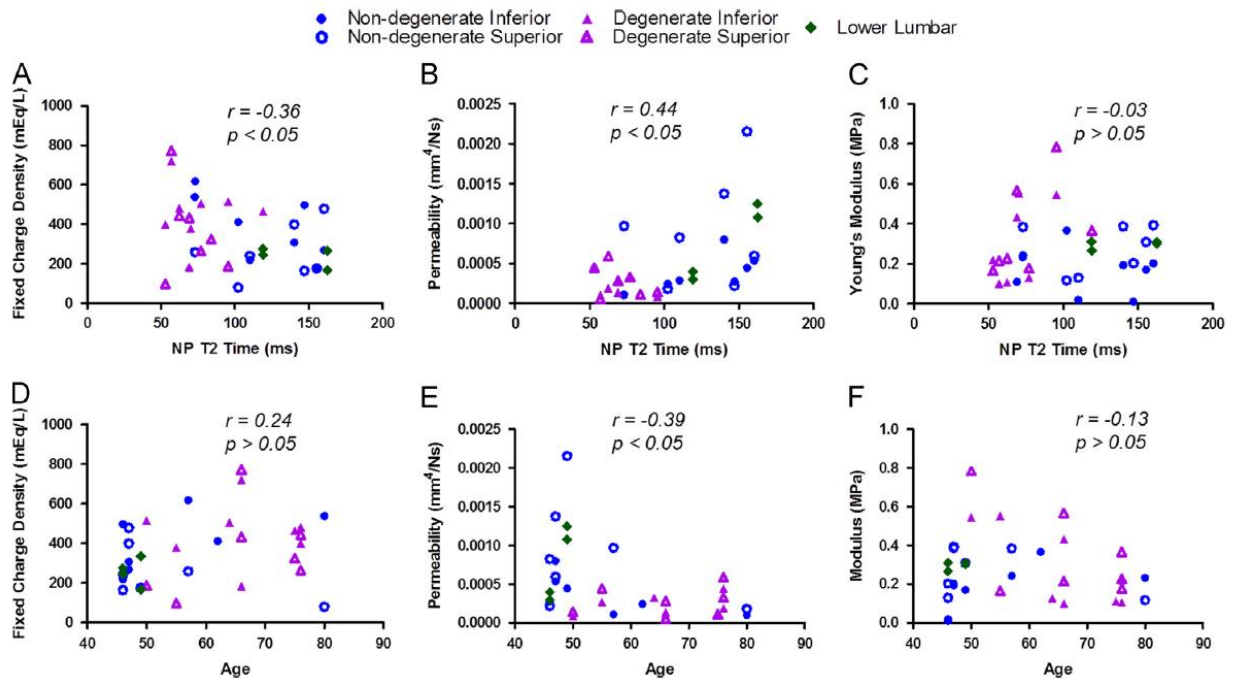


Figure 4-3: Mechanical parameters for all samples were evaluated for correlation with degeneration measured by nucleus pulposus (NP) T2 relaxation time and with specimen age. A lower T2 time represents a more degenerate disc. (A; D) Fixed charge density increases with degeneration ($r = -0.36$, $p < 0.05$) and does not change with age ($r = 0.24$, $p > 0.05$) while (B; E) permeability decreases with degeneration ($r = 0.44$, $p < 0.05$) and age ($r = -0.39$, $p < 0.05$). (C; F) Modulus was not correlated with degeneration or age ($p > 0.05$).

Histological Appearance

Histological assessment of NP-CEP-Bone segments demonstrated the structural organization of the CEP (Figure 4-4). The nucleus pulposus stained almost exclusively for proteoglycans, marking the boundary with the more fibrous CEP in non-degenerate samples (Figure 4-4A, 4-4C). The CEP from degenerated discs showed staining for proteoglycans (Figure 4-4B, 4-4D), inconsistent with measured composition. In non-degenerated CEP the proteoglycan staining appeared to be

concentrated at the pericellular matrix (PCM) (Figures 4-4A and 4-4C) but in degenerate CEP the proteoglycan staining was more dispersed (Figures 4-4B and 4-4D). The pericellular matrix, and thus the cells, appear to be randomly arranged and do not have the columnar organization observed in articular cartilage [138]. Fibers in the CEP tend to be oriented in the same direction although from polarized light it is unclear whether the fibers are parallel or perpendicular to the vertebrae (Figures 4-4E and 4-4F). Cells tend to be elongated parallel to the vertebrae, suggesting a parallel arrangement of fibers. This observation is supported by SEM as fibers appear mostly parallel to the vertebrae (Figure 4-4F).

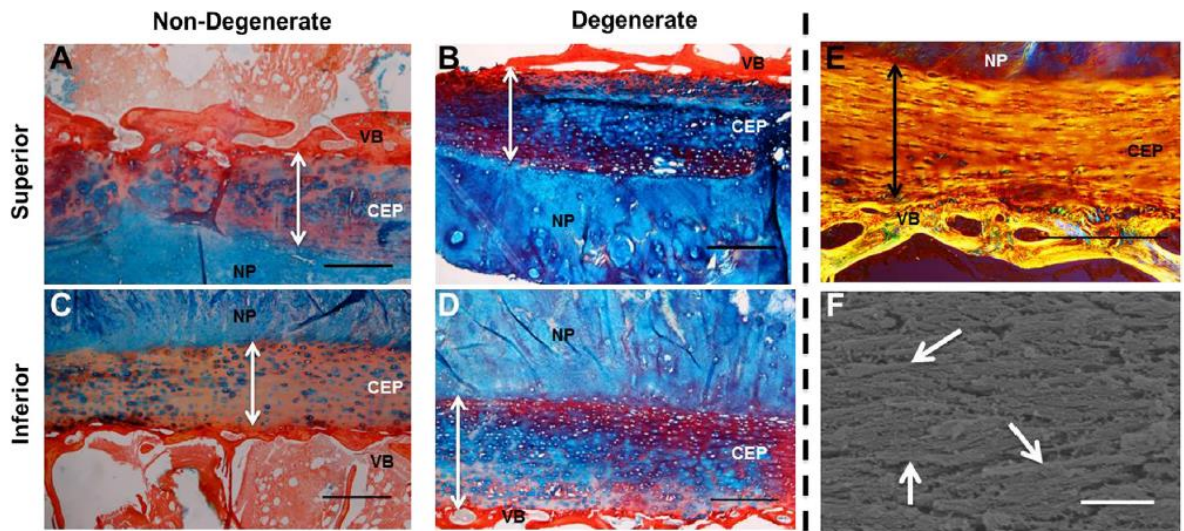


Figure 4-4: Histological assessment of non-degenerate and degenerate CEPs. Alcian blue and picosirius red staining of superior (A,B) and inferior (C,D) endplates. Arrows denote CEP thickness. Non-degenerate CEP (A,C) appear structurally different than degenerate endplates (B, D). Non-degenerate CEP have GAG concentrated in the PCM (E) while degenerate CEP have prominent GAG staining throughout the tissue. Polarized light image viewed over 45° cross polarizers (E) and SEM image of CEP fibers (F). Fibers appear aligned in parallel to the vertebral bone and are not arranged like those found in articular cartilage. Arrows (F) denote example

horizontally-oriented fibers. Scale bar (A-E) = 500 μm . Scale bar (F) = 1 μm . NP = Nucleus Pulposus, VB = Vertebra.

Confined Compression Mechanical Properties

The optimization to determine CEP properties from the confined compression tests fit the data very well, with an average R^2 of 0.96. Permeability significantly correlated with degeneration determined by NP T2 time, where lower T2 is more degenerate ($r = 0.44, p < 0.05$), and significantly decreased with fixed charge density ($r = -0.35, p < 0.05$) (Figures 4-3B and 4-5A, respectively). Permeability tended to be lower in degenerate inferior CEP compared to non-degenerate inferior CEP ($p < 0.1$). Permeability also decreased with age ($r = -0.39, p < 0.05$; Figure 4-3E). Modulus did not correlate with degeneration ($r = -0.03, p > 0.05$; Figure 4-3C), but tended to decrease with water content ($r = -0.31, p = 0.08$; Figure 4-5B). Modulus did not correlate with GAG content, suggesting that GAG plays a more significant osmotic role in the CEP than an elastic role. Permeability (k_0) was significantly greater in superior than inferior CEP in non-degenerate discs ($p < 0.05$) and tended to be greater in superior than inferior CEP in degenerate discs ($p = 0.08$).

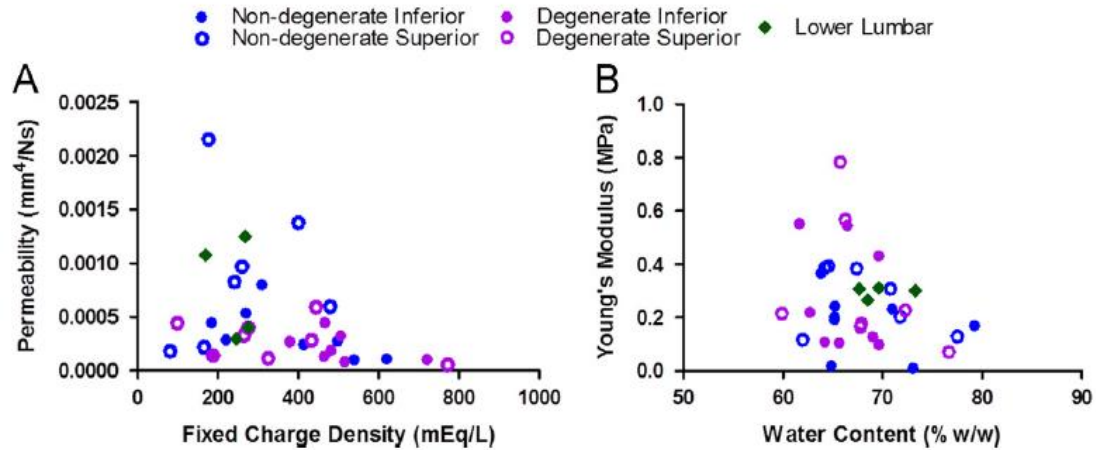


Figure 4-5: Permeability decreases with fixed charge density ($r = -0.35$, $p < 0.05$; A) and modulus tended to decrease with water content ($r = -0.31$, $p = 0.08$; B).

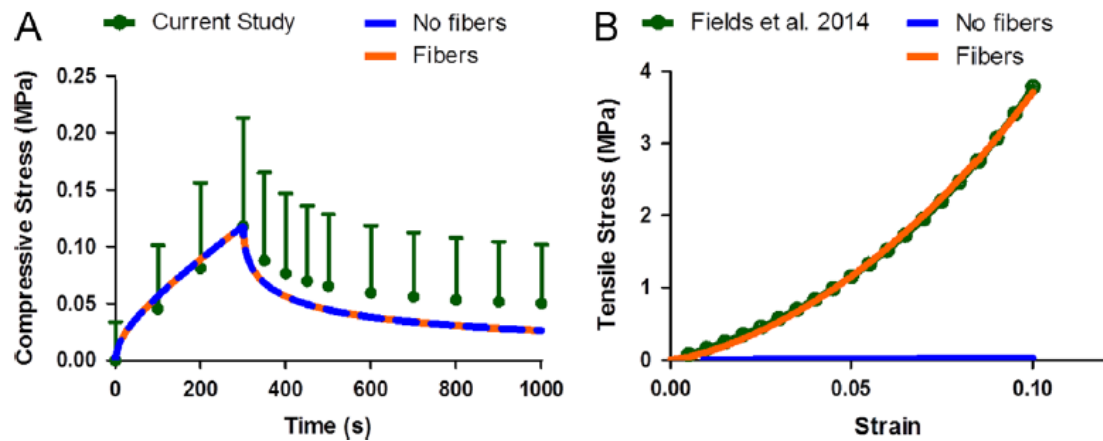


Figure 4-6: Fiber-reinforced model performance in compression and tension. Both models perform identically in confined compression (A) as fibers do not contribute in confined compression. However, fibers are essential to reproduce tensile data (B).

Finite Element Modeling of CEP Mechanics

An objective of this study was to model the CEP using measured extrafibrillar matrix and permeability properties and evaluate the role of collagen fibers. The fiber properties were obtained by optimizing to tensile test data [56]. The optimization for the tension test fit the experimental data well ($R^2 = 0.97$) and resulted in a fiber

modulus $\zeta_I = 7.01$ MPa and a fiber nonlinearity $\alpha_I = 2.88$ (unitless). At the tissue level, fiber-reinforcement had no effect on confined compression compared to the fiber-less model (Figure 4-6A), but fiber-reinforcement was necessary to reproduce tensile results (Figure 4-6B). Including CEP collagen fiber reinforcement significantly affected CEP mechanics but had little effect on the overall disc behavior in compression. When fibers were not included and an axial compression was applied to the disc, the CEP was predicted to experience large axial tensile strains (Figure 4-7A) and large shear strains (Figure 4-7B) in the regions near the AF. However, when fiber reinforcement was included, the CEP was in compression (Figure 4-7A) and shear strains were reduced compared to the fiber-less model (Figure 4-7B). Fluid flux, or water flow, through the CEP above the NP were 65% greater in the fiber-reinforced model due to the reduced CEP deformation (Figure 4-7C). Although inclusion of fibers had large effects in the region of the CEP, the effect was minimal for the entire disc. Including CEP fiber reinforcement increased the peak disc axial reaction force to compression loading by 13% but did not change the equilibrium axial reaction force (Figure 4-7D).

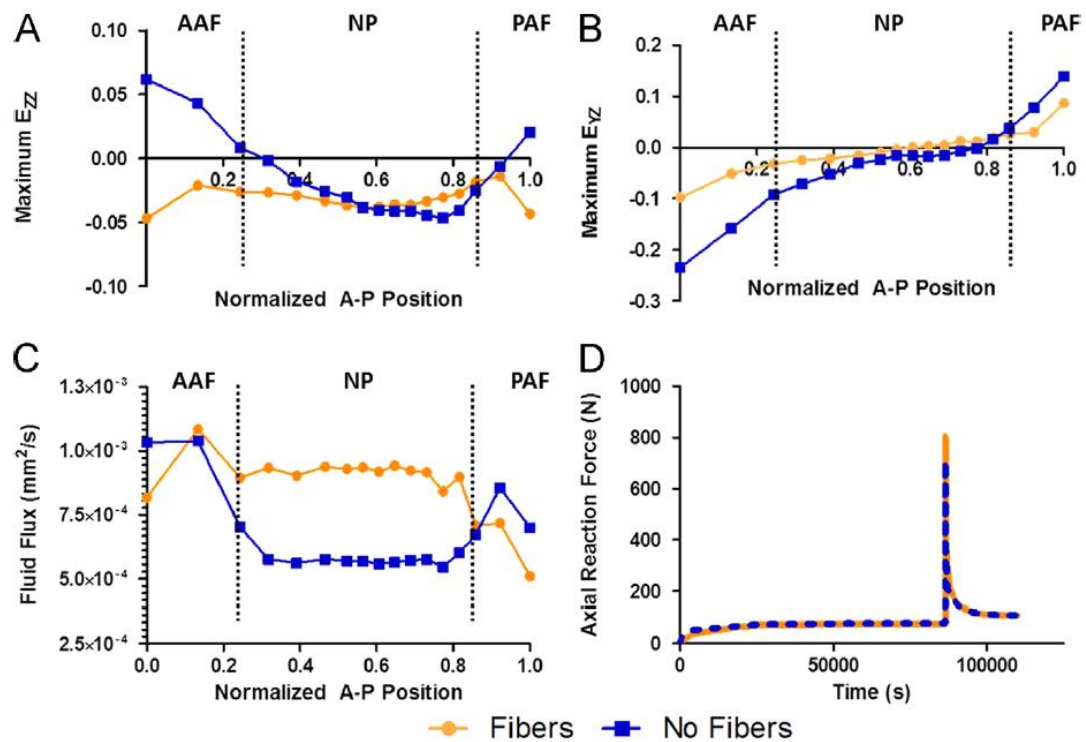


Figure 4-7: Compression stress-relaxation finite element results taken from the time step of maximum disc compression comparing the fiber-reinforced CEP model to the fiber-less model. AF and NP denote which disc sub-tissue is adjacent to the CEP with lines denoting tissue boundaries. Fibers significantly affect axial (A) and shear (B) deformations. Reduced CEP deformation allows for enhanced fluid flow (C). Fiber-reinforcement minimally affects global disc reaction force (D). *CEP: cartilage endplate, AAF: anterior inner annulus fibrosus, PAF: posterior inner annulus fibrosus, NP: nucleus pulposus*

Discussion

The aims of this study were to determine the influence of 1) degeneration and 2) superior and inferior site on human CEP mechanics and composition, as well as to 3) determine the role of CEP fiber reinforcement on CEP and disc mechanics. The first objective of this study, to quantify the CEP mechanical properties in confined compression and the effect of disc degeneration, demonstrated that the human CEP

mechanical function and composition change with degeneration. Notably, permeability decreased with degeneration, which has important implications related to obstruction of the disc's transport cycle [66, 139, 140]. Deleterious molecules like lactic acid may not be able to leave the disc as readily and may accumulate in the nucleus pulposus, reducing pH and affecting cell function and viability [25]. While CEP permeability is correlated with disc degeneration, whether permeability-related reduced transport *causes* disc degeneration is unknown. Other FE studies have estimated that transport should be reduced by 40% to reduce disc glucose production, and potentially cause disc degeneration [141, 142]. In this study, permeability in degenerate CEP was 60-70% lower than non-degenerate CEP, suggesting that changes in CEP permeability may indeed lead to reduced disc glucose production.

The observed reduction in permeability was correlated with increased CEP fixed charge density (FCD). Tissues with higher FCD can impede diffusive transport by creating a steric and ionic barrier [66]. Although this study only measured CEP permeability for Grade 3 discs, as more advanced degenerate discs did not have testable CEP, taken with other studies, we propose that the relationship between CEP permeability and disc degeneration is non-monotonic (Figure 8). The non-degenerate disc's transport cycle is at a normal baseline (Figure 8A). As degeneration proceeds (Figure 8B) permeability decreases, which may inhibit transport. In advanced degeneration, transport again increases [104], possibly due to combined CEP structural breakdown and disc height loss, allowing fluid to leave the disc more easily. This non-monotonic relationship between CEP permeability and degeneration may

also be accompanied by changes in fixed charge density. FCD increases with mild degeneration (measured by T2 time) and correlates with permeability. We hypothesize that this increase in FCD represents an accumulation of fragmented GAG chains that have been cleaved and expunged from the NP. These fragmented GAG chains may become entangled in the dense and charged CEP environment before slowly leaving the disc altogether [21, 143]. This observation is qualitatively supported by increased proteoglycan staining in CEP.

While this study demonstrated an increase in FCD with mild degeneration, it remains unclear how FCD changes with advanced degeneration, as studies often report GAG and water content and not FCD explicitly. It is challenging to interpret previous results of GAG and water content in the context of FCD, as FCD is a function of both. Nevertheless, GAG content increased in advanced degeneration [22], but this increase was accompanied by increased water content. On the other hand, GAG content has been shown to decrease with degeneration [18, 56, 107]. In the present study there was no significant change in GAG with degeneration. The role of GAG content, water content and their impact on the more functional parameter, FCD, is a complex relationship.

The second objective of this study, to determine the influence of disc site on human CEP mechanics and composition, demonstrated that the superior CEP permeability was greater than that of inferior CEP. The origins of this mechanical difference remains unknown but may be related to differences in the adjacent superior and inferior vertebral bone and physiological loading. Under spinal compression the

nucleus pulposus pressurizes and compresses both CEPs, but different underlying bone properties may affect the loading experienced in the CEP. Furthermore, since the spine does not experience pure compression, it is very likely that loading conditions are different across each disc-bone interface. As the tissues remodel in response to their respective loading conditions, differences in mechanical properties of both CEP and the adjacent bony endplate and vertebrae body may develop. For example, the vertebral endplate inferior to the disc has a smaller mean failure load [130, 144] and is thinner [145], rendering it more susceptible to Schmorl's nodes [34]. Therefore experimental studies of the CEP and vertebral endplate should carefully control inferior/superior location. Similarly, clinical therapies of the disc should acknowledge potential differences between superior and inferior bone and CEP properties.

The third objective of this study, to model the CEP and evaluate the role of collagen fibers, successfully demonstrated that fibers are important for the CEP function and fluid flow, but have minimal effect on overall disc deformations. These findings demonstrate that CEP properties should reflect its structure in order to produce a physiologically likely stress-strain response at the tissue level. Neglecting the fiber contribution results in CEP axial strains that are in tension and also predicts very large shear strains. These predictions are physiologically unlikely, as axial tensile strains could cause delamination of the CEP. Ultimately, even with fiber-reinforcement, CEP shear strains are large due to significant lateral expansion of the NP. This suggests that excessive shear deformation may be a failure mechanism of the CEP, consistent with clinical observations of CEP delamination [115, 121]. Moreover,

while fiber-reinforcement can affect CEP mechanics, it doesn't significantly affect disc-level mechanics, with reinforcement increasing maximum disc reaction force by only 13% without affecting equilibrium reaction force. Thus previous models used to evaluate overall disc deformations remain valid [126, 127, 131, 136, 146], however they may not predict accurate stress and strain in the CEP and in nearby tissues.

The finite element simulations confirm that the collagen fibers significantly affect the fluid flow through the CEP. By including the fibers, the CEP fluid flux is nearly doubled compared to simulations that neglect the fibers. This can be explained by noting that fluid flow is dependent on the CEP deformation. Including fibers results in less CEP deformation, decreasing apparent permeability, and promoting greater fluid flow. Excluding the fiber distribution in models of the CEP may underestimate fluid flow and therefore convection, a potentially important component of the transport cycle [2, 25, 133]. Fluid flow out of the disc due to mechanical loading reduces the disc height and thus, the distance between the solute supply in the vertebral body and the cells in the center of the NP, which would promote transport of nutrients through the disc to the central NP cells. On the other hand, fluid flow out of the disc also reduces NP water content and increases NP FCD, which would inhibit transport of nutrients through the disc to the central NP cells [116]. Fiber-reinforcement may play a role in balancing these opposing mechanisms. Deviations from the normal fiber organization and fiber mechanical properties may affect CEP deformations and fluid flow, causing an imbalance between transport-promoting and

transport-inhibiting mechanisms. Furthermore, deviations from normal fiber organization are likely relevant across the full 3D distribution of fibers.

The values of the extrafibrillar elastic and permeability properties reported here reflect the accepted functions of the CEP, including transmitting compressive loads. In order to accomplish this, the CEP must be stiff enough to support the high pressures developed in the nucleus pulposus and transmit loads across the disc-bone interface. The CEP accomplishes these functions by generating osmotic pressures comparable to those in the NP, arising from similar fixed charge densities. The CEP FCD is 80-770 mM, and is comparable to the 40-700 mM FCD of the NP [16, 52]. Interestingly, the CEP compressive modulus in this study (270 kPa) and our previous work (300 kPa) is on the lower end of the range for articular cartilage 300-1000 kPa [147-150] which also supports large compressive loads. Since the CEP compressive modulus is significantly lower than the CEP tensile modulus (~6 MPa) [56], the CEP exhibits tension-compression nonlinearity [151-153] which provides for interstitial fluid pressurization as a mechanism in supporting load [125, 152].

Despite having some mechanical property similarities, the CEP has structural and biochemical differences that distinguish it from articular cartilage. The fiber arrangement in articular cartilage has distinct zones, including a surface zone with fibers aligned along the surface, a middle zone with randomly dispersed fibers, and a deep zone with vertical fibers integrating with the subchondral bone [154]. The CEP fibers appear to be parallel to the NP and do not have columnar organization at the cartilage-bone interface. While both tissues interface with bone, the strength of this

interface in the CEP is likely much weaker due to a lack of fibrillar connection. This may render the CEP weak in shear and may lead to detachment from the bone as seen in lateral herniation [115, 121]. Furthermore, the CEP biochemical composition is different from that of articular cartilage. The CEP is much less hydrated and has a lower GAG content than human articular cartilage [18, 57, 124, 155, 156]. These structural and biochemical differences between CEP and articular cartilage, together with the different functional roles of these tissues, where the CEP functions to provide a barrier between the bone and the nucleus pulposus and articular cartilage supports joint contact, support the notion that the CEP and articular cartilage are unique and different tissues.

In conclusion, compressive experimental testing and biphasic-swelling modeling show that permeability and fixed charge density are significantly affected by degeneration and superior and inferior location. These findings have important implications in the mechanics and health of the intervertebral disc. Furthermore, CEP fibers are organized parallel to the VB and the NP and may contribute to large shear strains and delamination failure of the CEP. Fibers also contribute to the disc transport cycle by reducing CEP axial strains and enhancing fluid flux. Collectively, these results show that CEP permeability and fiber-reinforcement may be important factors influencing the disc transport cycle.

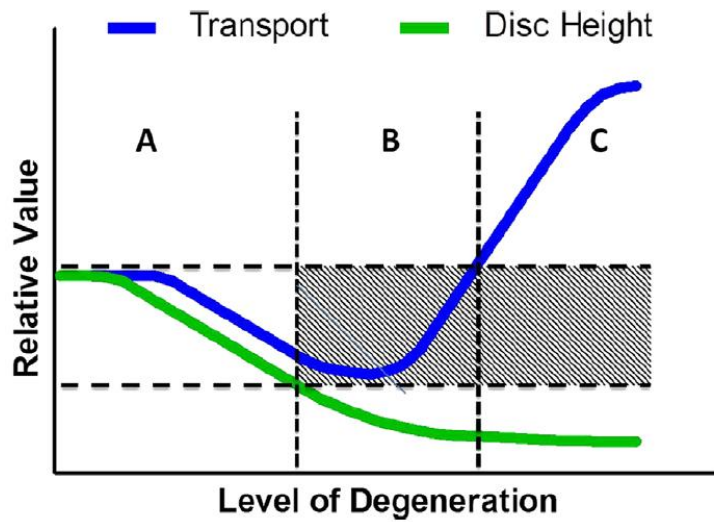


Figure 4-8: Graph describing proposed changes in transport and disc height with degeneration. In non-degenerate discs, there is an unimpeded transport cycle (A). An optimal range of transport properties permits this balance. As degeneration proceeds, structural and biochemical changes to the CEP and disc reduce transport properties, inhibiting transport (B). In advanced degeneration, transport is enhanced but disc height substantially decreases (C).

Chapter 5

AIM 3 – MECHANICAL COUPLING WITH APPLIED LOADING CAUSES LARGE OFF-AXIS RESPONSES ACROSS ALL SIX DEGREES OF FREEDOM IN THE HUMAN DISC SEGMENT

The kinematics of the intervertebral disc are defined by six degrees of freedom (DOF): three translations (T) (Tz: axial compression, Tx: lateral shear, Ty: anterior-posterior shear) and three rotations (R) (Rz: torsion, Rx: flexion-extension, Ry: lateral bending), (Figure 5-1, adapted from [102]). Mechanical tests using multiaxial testing systems such as pulleys and weights [157], cables and linear actuators [158, 159], stepper motors and linear bearings [160, 161], and Stewart platforms (hexapods) [71, 88, 89] have demonstrated that the disc's load-deformation and moment-rotation responses are highly nonlinear and viscoelastic. Quantifying these mechanical behaviors across all six DOF are critical for designing and testing disc therapies, such

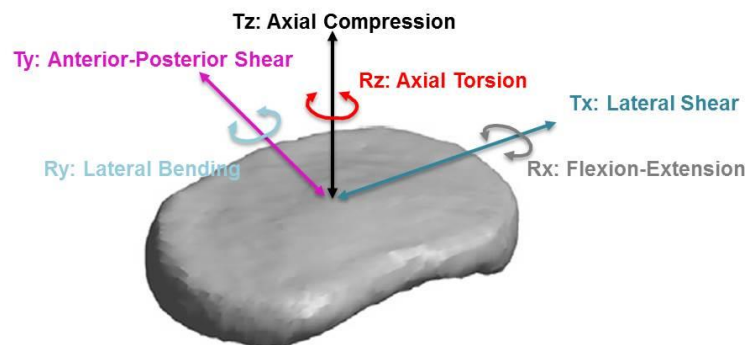


Figure 5-1: Schematic of axes of loading for the intervertebral disc and labels for each degree-of-freedom. T = translation and R = rotation. (Figure modified from Peloquin et al. 2014)

as implants and tissue engineered constructs [162, 163] and also for validating finite element models [71]. Moreover, disc multi-axial mechanics drive many critical physiological processes under investigation, such as low back pain; tears and herniation; injury, repair and remodeling; and cell mechanotransduction [164-166].

The disc mechanical response has been measured in all DOFs; however, most studies apply either position control or pure moment control in only one or two DOFs, such as axial compression [67, 87, 167] or axial torsion [11, 168, 169]. Most studies do not control or measure all 6 DOFs simultaneously, meaning that the off-axis DOF are ignored. Importantly, there is evidence that the 6 DOFs are mechanically coupled, such that loading in one DOF affects the mechanics of the other 5 “off-axis” DOFs [170]. For example, applying axial compression increases stiffness in the rotational DOFs (Rx, Ry, Rz) [46, 171]. In this study we sequentially tested the disc’s response to cyclic loading in each of the 6 DOFs, using a state-of-the-art hexapod system to measure both same-axis and off-axis responses [72, 73, 88]. We hypothesized that applied loading in each DOF would generate coupled off-axis motions (translations and rotations) in the other 5 DOFs, and we tested this hypothesis by correlating, for each DOF, the applied motion vs. measurements of the resulting 5 off-axis motions.

Relationships between disc geometry and disc mechanics, including coupled off-axis responses, are important for evaluation of data from different sized donor and patient discs, interpretation of finite element models, and development of patient-specific models. Geometry, such as height and width, is known to affect the same-axis mechanical response of a disc segment when loading is applied to a DOF [45, 100].

For example, in a computational parametric simulation, disc height correlated with range of motion in pure moment flexion-extension (Rx), lateral bending (Ry), and axial torsion (Rz) [100]. In this study, we hypothesized that coupled off-axis motions for each DOF are also, like the same-axis mechanical response, correlated with disc geometry.

Therefore, the objectives of this study were to quantify the mechanical behavior of the intervertebral disc in all six degrees of freedom (DOFs), measure the coupling between each applied motion in each DOF and the resulting off-axis motions, and test the hypothesis that disc geometry influences these mechanical behaviors.

Methods

Specimens

Human lumbar intervertebral disc bone-disc-bone segments ($n = 8$) from 5 spines (3 male and 2 female; age 49 ± 9 years, range 35 to 59) were dissected with posterior elements removed and graded for degeneration (Levels: L1-L2 ($n = 1$), L2-L3 ($n=1$), L3-L4 ($n = 2$), L4-L5 ($n = 4$)). To limit variation from degeneration, only mild to moderately degenerated discs (Pfirrmann grades 2 to 3) were used. The disc's anterior-posterior width (W_{AP}), lateral width (W_{LAT}), and disc height were determined from lateral and coronal x-ray images. The disc's cross-sectional area was calculated from $A = 0.84 * W_{AP} * W_{LAT}$ [172]. The disc's aspect ratio was calculated as W_{LAT} / W_{AP} . Prior to testing, discs were thawed overnight under 50 N axial compression in 0.15 M PBS with protease inhibitors. Three k-wires were inserted halfway into the sides of each vertebra, 120° apart, and the vertebrae were potted into custom cups

using polymethylmethacrylate (bone cement). An alignment device was used during potting to keep the inferior and superior cups parallel [88]. The potted bone-disc-bone segment specimen was then mounted in a 6DOF hexapod robot with a 37 °C 0.15M PBS bath for mechanical testing.

Mechanical Testing

Segments were tested using a state-of-the-art hexapod system that simultaneously controls and measures all 6 DOFs [72, 73, 88]. The protocol consisted of an axial compression preload followed by 6 sequential tests, subsequently called “DOF tests”, each of which applied cyclic loading to one target DOF (Figure 5-2). A novel hybrid control system was used. In each DOF test, prescribed cyclic loading was applied to the target DOF in position or load control, and the off-axis DOFs were load controlled in real time to maintain (approximately) zero off-axis forces and moments [173]. This adaptive approach to minimizing off-axis loads and moments allows the disc’s center of rotation to change during the protocol, which is an advantage over conventional tests that fix the center of rotation to one location, potentially causing supra-physiologic and damaging loads [170].

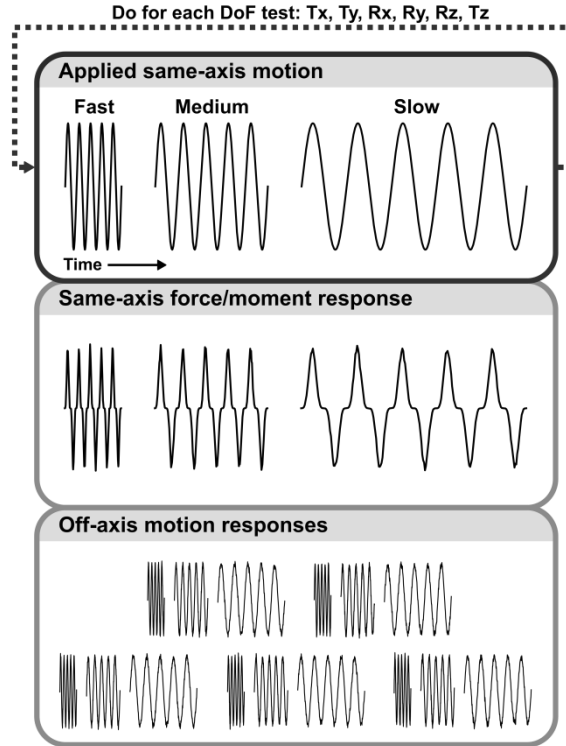


Figure 5-2: Schematic for mechanical testing protocol. Testing consisted of an overnight 0.2 MPa compression preload followed by Degree of Freedom (DOF) tests where 5 cycles at 0.5, 0.05, and 0.005 Hz (fast, medium, and slow rates) were performed for each DOF, followed by a 30 minute recovery period. To maintain off-axis zero force and moment conditions, the off-axes displace and rotate in response to loading. DOF test order was Tx (lateral shear), Ty (anterior-posterior shear), Rz (axial torsion), Ry (lateral bending), and Rx (flexion-extension). Finally, the Tz (axial compression) test was performed with 5 cycles at 1, 0.1, and 0.01 Hz with recovery (R) after after 0.1 Hz as well as after the 0.01 Hz test.

The preload consisted of axial compression with off-axis forces and moments controlled to zero. It was held overnight for 12 hours before the DOF tests started. The preload was chosen to produce a nucleus pulposus (NP) pressure of 0.2 MPa, which mimicked physiologic conditions and reduced axial displacement creep during the subsequent DOF tests. The preload force was calculated as $F = \frac{P \cdot A}{1.5}$, where P is the desired NP pressure (0.2 MPa), A is the disc cross-sectional area, and 1.5 is an

empirically derived factor [73]. The axial preload was maintained during through the DOF tests except (as described below) when axial force was cyclically varied in the Tz test.

Six “DOF tests”, each of which applied cyclic loading to a specific DOF and controlled the off-axis moments and forces to be zero (hybrid control), were performed in the sequence Tx, Ty, Rz, Ry, Rx, Tz (Figure 5-2). Each DOF test was separated from the others by a 30 minute recovery period (held in the preload state). Each DOF test consisted of a 3 blocks of 5 loading cycles at fast, medium, then slow cycle frequencies. In the Tx, Ty, Rz, Ry, and Rx tests, the blocks’ frequencies were 0.5, 0.05, and 0.005 Hz, and the target DOF was sinusoidally loaded in displacement or rotation control. In the Tz test, the blocks’ frequencies were 1, 0.1, and 0.01 Hz, and Tz was loaded with haversine cycles in force control. Loading in Tz caused significant axial creep, which is why the Tz test was done in force control. An additional 30 minute recovery period was also inserted after the Tz medium rate block to allow some recovery of axial creep before the slow rate block started. The Tx and Ty tests had a slightly modified hybrid control scheme to prevent the test fixtures from colliding. In the Tx test, Ry rotation was controlled at 0°, and in the Ty test, Rx rotation was controlled at 0°. Overall, this mechanical testing sequence (Figure 5-2) was designed to minimize disc volume loss (water exudation) during the protocol [72]. The cycle amplitudes in each DOF test were chosen to be physiologically reasonable [69, 174, 175]: Tx = ±0.6 mm, Ty = ±0.6 mm, Rz = ±3°, Ry = ±4°, Rx = ±3°, and Tz = -0.2 MPa to -1.1 MPa.

Data Analysis

For each DOF test, stiffness in the applied DOF (same-axis stiffness) was calculated from the load-displacement curve of the applied DOF in the final loading cycle (slow rate). Stiffnesses were calculated by linear regression between 70 and 90% of the maximum force or moment. Potential correlations between stiffness and each geometry parameter (height, lateral width, anterior-posterior width, aspect ratio) were determined using Pearson correlation.

To determine the relationship (coupling) between each applied DOF and its off-axis responses, the final loading cycle (a slow rate cycle) for the applied DOF was plotted against the corresponding off-axis motions. To evaluate the strength of this correlation, a second-order polynomial regression (r^2) was performed with significance set at $p < 0.05$. For the purposes of this study, data from the slow tests was used because the hexapod system controller exhibited poor control at the fast rate (future instrument improvements will address this).

Since the applied loading and hence the off-axis responses in each DOF test were cyclic, each off-axis response was also characterized by the *offset* of its oscillations and the *amplitude* between its value at the start of the DOF test and the value about which it oscillated during the DOF test (Figure 5-3). The amplitude and offset of each off-axis response was determined relative to a line fit through the oscillation of the off-axis displacement/rotation vs. time (Figure 5-3, red line). The offset is the intercept of the line with the start of loading. The amplitude is the average distance from the line to the peak and valley of the oscillation over the five applied cycles. To determine

whether there was a significant off-axis response, the offset and amplitude were compared to zero using a *t*-test. To determine the effect of geometry, each geometry parameter was correlated against each off-axis offset and amplitude.

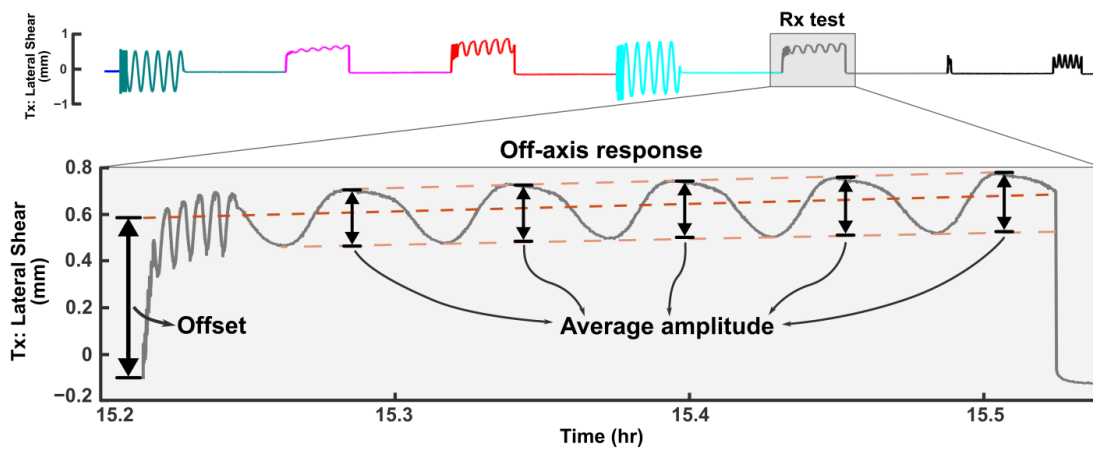


Figure 5-3: Representative response in Tx (lateral shear) throughout the entire test protocol. Large off-axis responses to each DOF test can be observed. The expanded response of Tx to Rx loading (inset) shows how the offset and amplitude were calculated from a line that was fit through the oscillation. The offset is the intercept of the line with the start of loading. The amplitude is the average distance from the line to the peak and valley of the cyclic response over the five applied cycles for each loading rate, calculated by subtracting the fit line from the experimental data.

A representative same-axis load–displacement (or moment–rotation) curve for each DOF test’s slow rate cycles is shown in Figure 5-4 and average same-axis stiffnesses are reported in Table 5-1. Correlations of same-axis stiffness with geometry were evaluated (Figure 5-5, Table 5-1). The axial compression (Tz) stiffness tended to correlate with disc height ($r = 0.66$, $p = 0.08$, Figure 5-5), and also strongly correlated with A-P width ($r = 0.75$) and lateral width ($r = 0.81$), but not aspect ratio ($p = 0.9$, Figure 5-5B). Lateral shear (Tx) stiffness and A-P shear (Ty) stiffness were not correlated with disc height (Figure 5-5). A–P shear (Ty) stiffness correlated with

lateral width ($r = 0.70$, $p = 0.05$), and lateral shear (Tx) stiffness ($r = -0.85$, $p < 0.01$) correlated with aspect ratio (Figure 5-5). Interestingly, none of the rotational DOF stiffnesses were correlated with disc height (Figure 5-5), but flexion-extension (Rx) stiffness ($r = -0.86$, $p < 0.01$) and torsion (Rz) stiffness ($r = -0.84$, $p < 0.01$) were correlated with aspect ratio (Figure 5-5).

Table 5-1: Summary of Results

	Lateral Shear (Tx)	Anterior - Posterior Shear (Ty)	Compression (Tz)	Flexion-Extension (Rx)	Lateral Bending (Ry)	Torsion (Rz)
Overnight Creep	0.10±0.12 mm	0.21±0.26 mm	0.68±0.34 mm	N/A	N/A	0.74±0.61 deg
Stiffness	152.5 ± 60.8 N/mm	105.3 ± 70.8 N/mm	2132.0 ± 437.7 N/mm	0.133 ± 0.176 Nm/deg	0.918 ± 0.568 Nm/deg	2.276 ± 1.033 Nm/deg
Correlation with Disc Height (r^2; p)	0.36; 0.12	0.28; 0.17	0.43; 0.08[#]	0.29; 0.17	0.01; 0.89	0.06; 0.55
Correlation with Aspect Ratio (r^2; p)	0.73; 0.01*	0.37; 0.11	7.8e-4; 0.95	0.73; 0.01*	0.35; 0.13	0.70; 0.01*
Correlation with Lateral Width (r^2; p)	0.38; 0.10	0.50; 0.05*	0.66; 0.01*	0.19; 0.29	0.04; 0.63	0.09; 0.48
Correlation with A-P Width (r^2; p)	0.01; 0.82	0.11; 0.43	0.57; 0.03*	0.01; 0.82	0.28; 0.18	0.04; 0.65

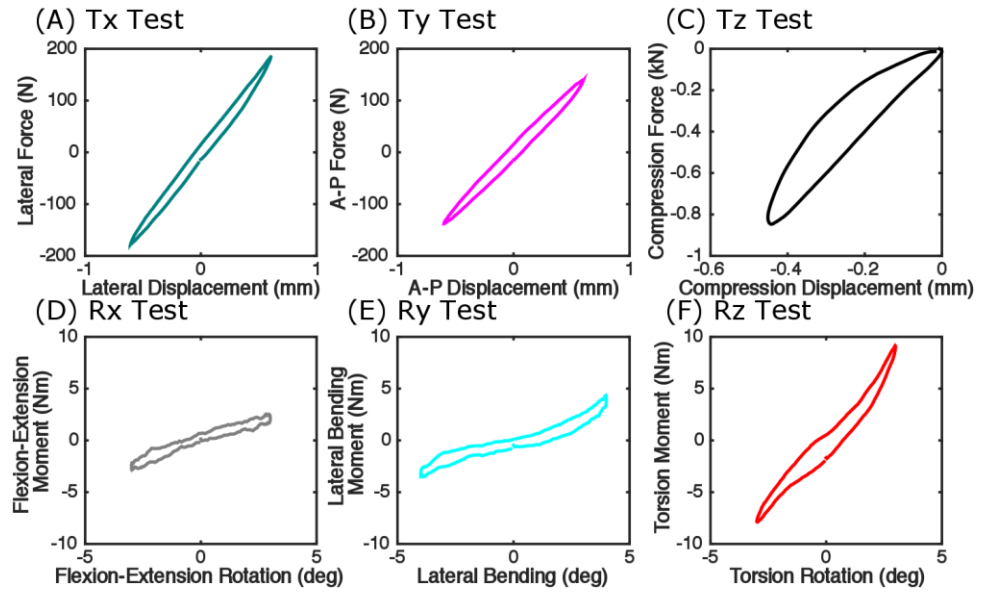
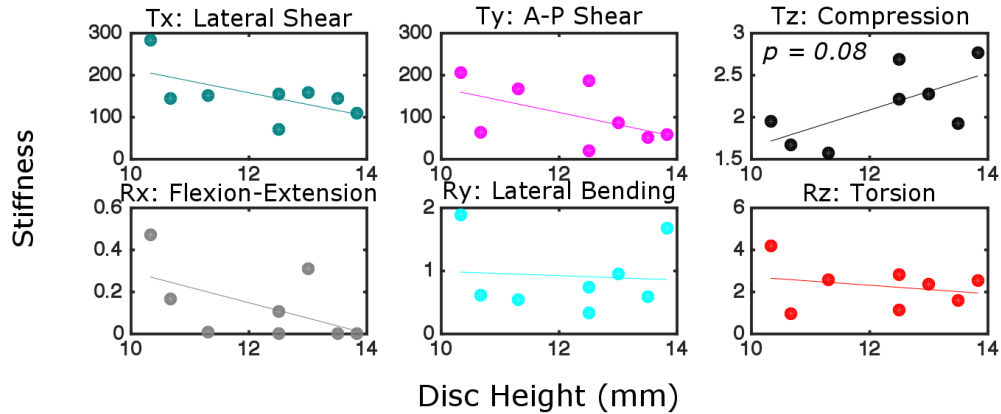


Figure 5-4: Representative same-axis response of the final cycle for the slow rate in each DOF test. Top: the translation degrees of freedom (force vs. displacement, A-C), Bottom: the rotation degrees of freedom (moment vs rotation, D-F).

(A) Stiffness vs Disc Height Correlations



(B) Stiffness vs Aspect Ratio Correlations

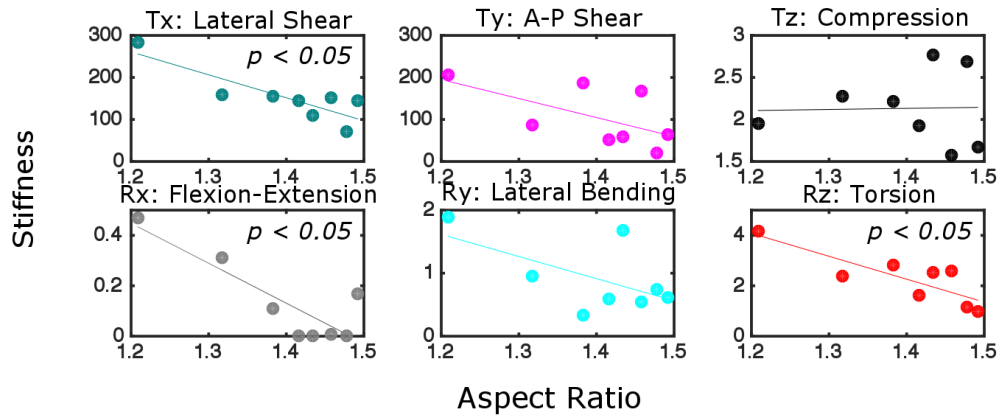


Figure 5-5: Correlations between stiffness and measures of disc height (A) and aspect ratio (B). Stiffness for translation DOFs have units of N/mm (Tx, Ty) and kN/mm (Tz) while stiffnesses for rotation DOFs have units of Nm/deg. Correlations are listed in Table 5-1.

Off-axis Mechanical Response

The 6 DOF response for a representative specimen throughout the entire testing protocol is shown in Figure 5-6. During the 12-hour preload (0.2 MPa axial compression), there was a large axial creep $T_z = -0.70$ mm (Table 5-1). A small amount of creep occurred in the lateral shear $T_x = 0.10$ mm, A-P shear $T_y = 0.21$ mm, and torsion directions $R_z = 0.74$ deg (Table 5-1). Similarly, throughout the duration of testing the segment continued to creep in axial displacement (T_z , Fig 6C), and with

small amounts of additional creep in torsion (Rz, Fig. 6F), lateral shear (Tx, Fig. 6A) and A-P shear (Ty, Fig. 6B). There was no creep in flexion-extension (Rx, Fig. 6D) and lateral bending (Ry, Fig. 6E), as these were controlled to be zero.

The off-axis responses were large, with magnitude similar to the applied DOF (Figure 5-6). For example, lateral shear (Tx), was controlled to +/- 0.6 mm, but when the slow rate lateral bending (Ry) loading was applied, the coupled displacement in lateral shear ranged from +/-0.7 mm (Figure 5-6A). Similar effects, where the coupled off-axis motion is greater than or equal to the applied motion can be seen for all of the directions (Figure 5-6B-E), except perhaps torsion Rz which is less than 1 deg (Figure 5-6F). Notably, the response in the axial direction was qualitatively different than that of the lateral and anterior-posterior directions (Figure 5-6C). In the Tz DOF test, applied compressive loading caused the disc to decrease in height, but loading of the other DOFs caused disc height to increase in order to keep the axial force at its controlled preload value (Figure 5-6C). That is, when the disc was loaded in all other DOFs the disc pressure increases [171], and in order to maintain the applied preload, the axial displacement is reduced.

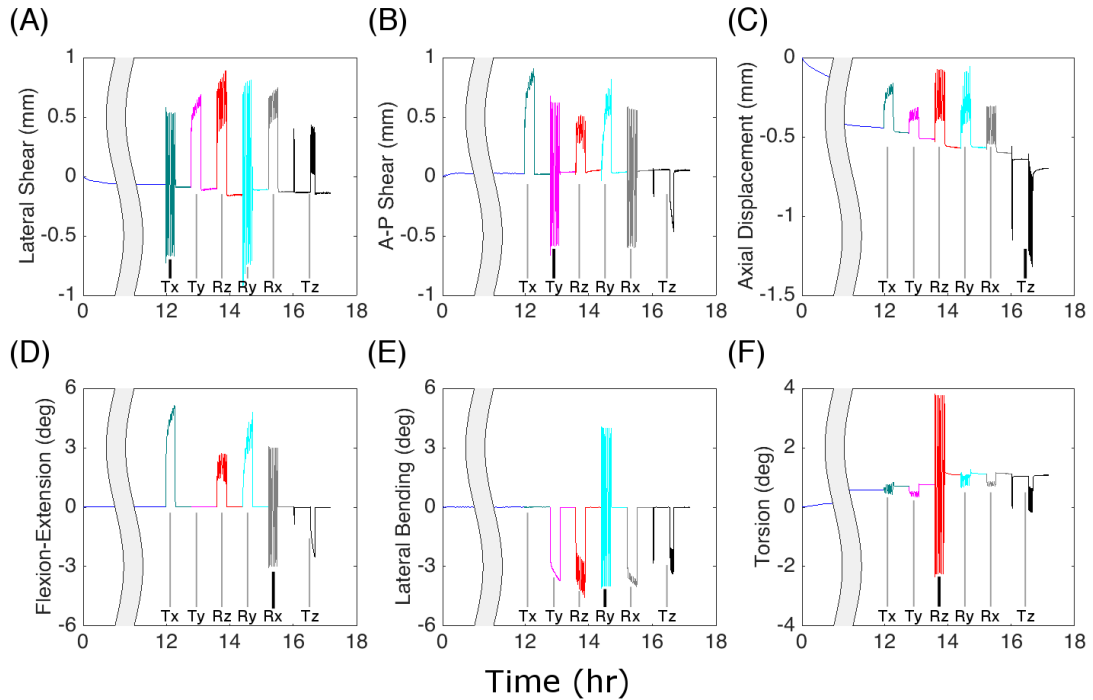


Figure 5-6: Representative displacements and rotations for all six DOF throughout the entire test protocol. Labels on the bottom of each sub-figure denote the applied DOF tests. Large creep occurred throughout the test for axial compression (C) and some creep occurred for lateral shear (A), anterior-posterior shear (B), and torsion (F), while flexion-extension (D) and lateral bending (E) were controlled to zero throughout. Large off-axis response occurred for all six DOF throughout the duration of testing.

The average off-axis response was plotted against the applied DOF and tested for correlations (Figure 5-7). The off-axis response was significantly correlated ($p < 0.001$) to applied displacements and rotations for all combinations and at both slow and medium rates (Figure 5-7B). Off-axis rotations that were controlled to be 0° (Ry during the Tx test, and Rx during the Ty test) were not included; these are shaded gray in Figure 5-7A. The strength of the correlations ranged from $r^2 \approx 1$ to ≈ 0 (Figure 5-7B). Off-axis axial compression (Tz) was strongly correlated to all applied DOFs (red box in Figure 5-7A, $r^2 > 0.8$ in Figure 5-7B). The other off-axis translations (Tx, Ty)

tended to be especially strongly coupled to applied rotation (Rx, Ry, Rz tests). For example, the off-axis Tx response correlated with applied Ry and Rz loading with r^2 values of 0.99 and 0.98, respectively. The pattern of correlations between applied DOF loading and off-axis responses was similar between the slow and medium loading rates, but with decreased r^2 values for the medium loading rate (Figure 5-7B).

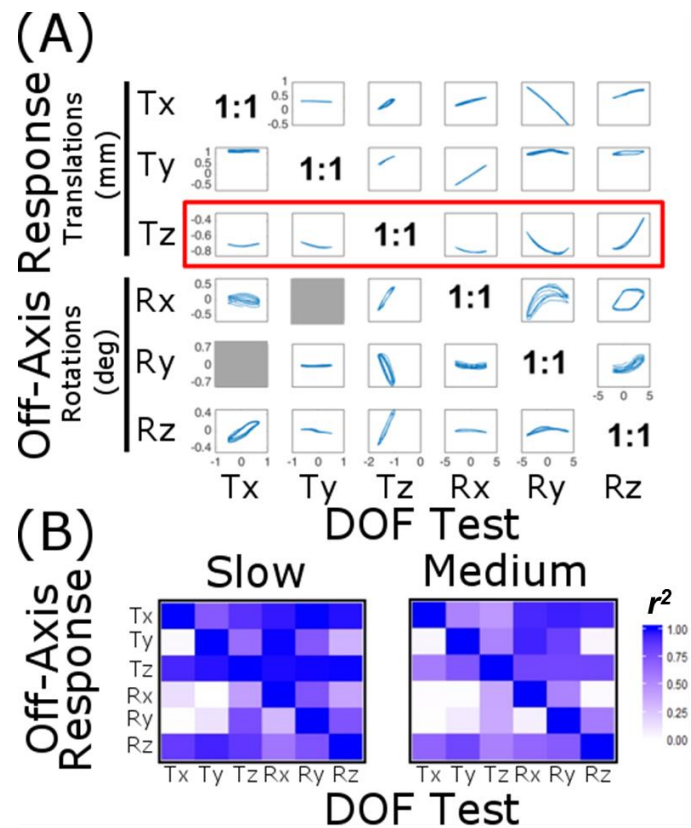


Figure 5-7: (A) Off-axis response in each DOF averaged over all disc specimens plotted against the applied DOF for the slow rate. All responses are significantly correlated with applied loading ($p < 0.01$) except for Rx during Ty loading and Ry during Tx loading (which were controlled to be zero in the test protocol). (B) The strength of the correlation (r^2) between applied and off-axis DOF for slow and medium rates of loading. The slow rate relationships are preserved at the medium rate although the r^2 values themselves are reduced.

Off-axis Amplitudes and Offsets

The off-axis responses in each DOF test was decomposed into an offset and amplitude, as described in the methods (Figure 5-8). Many off-axis offsets and amplitudes were large; all significantly differed from zero. A large Tz offset (0.19 mm) was observed in response to an applied axial torsion (Rz). Some off-axis amplitudes were comparable to the applied amplitudes chosen for the DOF test protocols (Figure 5-8, blue line). As in the previous paragraph, Tx and Ry, Ty and Rx, and Tz and Rz were found to be particularly strongly coupled. The off-axis lateral shear (Tx) amplitude (0.62) was strongly coupled with applied lateral bending (Ry), and was of similar to the amplitude applied in the Tx test (0.6 mm). Similarly, the off-axis lateral shear (Ty) had a large amplitude (0.53 mm) and offset (0.46 mm) with applied flexion-extension bending (Rx). In addition, the coupled off-axis axial compression (Tz) amplitude (0.16 mm) with applied axial torsion (Rz) was large and of similar magnitude to the amplitude applied in the Tz DOF test (0.29 mm). The off-axis Tz amplitudes overall tended to be greater in rotational DOF tests (0.10-0.16 mm) than in translational DOF tests (0.03-0.04 mm). These observations support the hypothesis that the disc's off-axis displacements and rotations depend on (are coupled to) motion in the applied DOF.

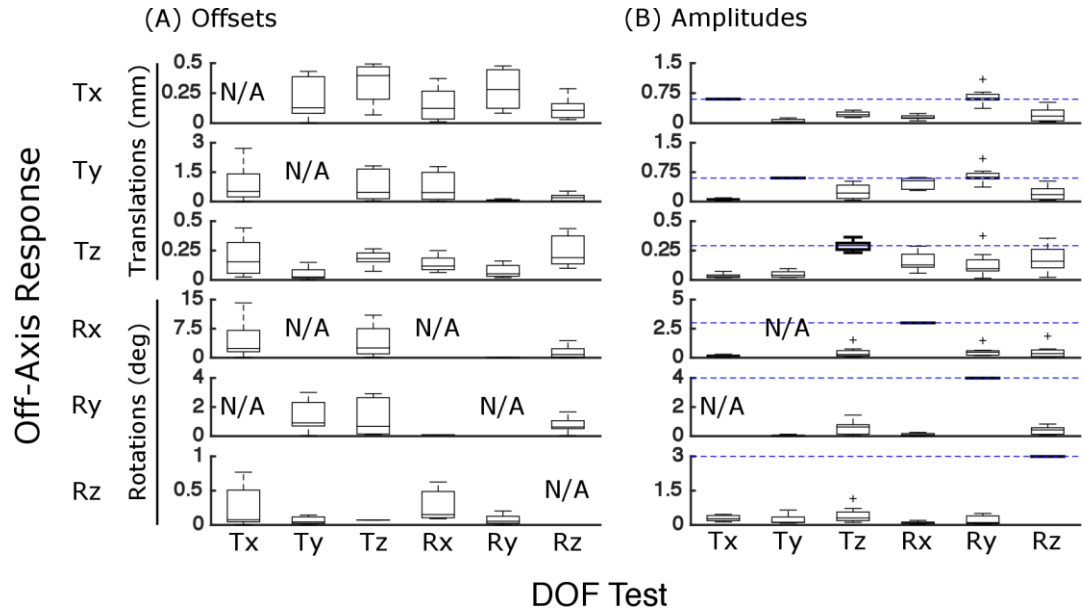


Figure 5-8: Magnitude of the (A) offset and (B) amplitude for the off-axis DOFs, median and inter-quartile range for the slow rate. All offsets and amplitudes are significantly non-zero. Blue lines in (B) denote the applied magnitude for comparison. Amplitudes for translational DOF tend to be larger and of similar magnitude as the applied amplitudes when rotational DOFs are applied.

Relationship between Off-axis Mechanical Response and Disc Geometry

The off-axis mechanical response in each DOF test was hypothesized to depend on disc geometry. Disc height, A–P width, and lateral width were found to be significantly correlated with some, but not all, of the off-axis amplitude and offset response variables (Figure 5-9). Aspect ratio was not significantly correlated with any off-axis response. More offsets than amplitudes were significantly correlated with disc geometry. Lateral width had a particularly large number of significant correlations. Interestingly, lateral width and A–P width tended to have opposed effects on the off-axis offsets and amplitudes (opposite sign correlation coefficients).

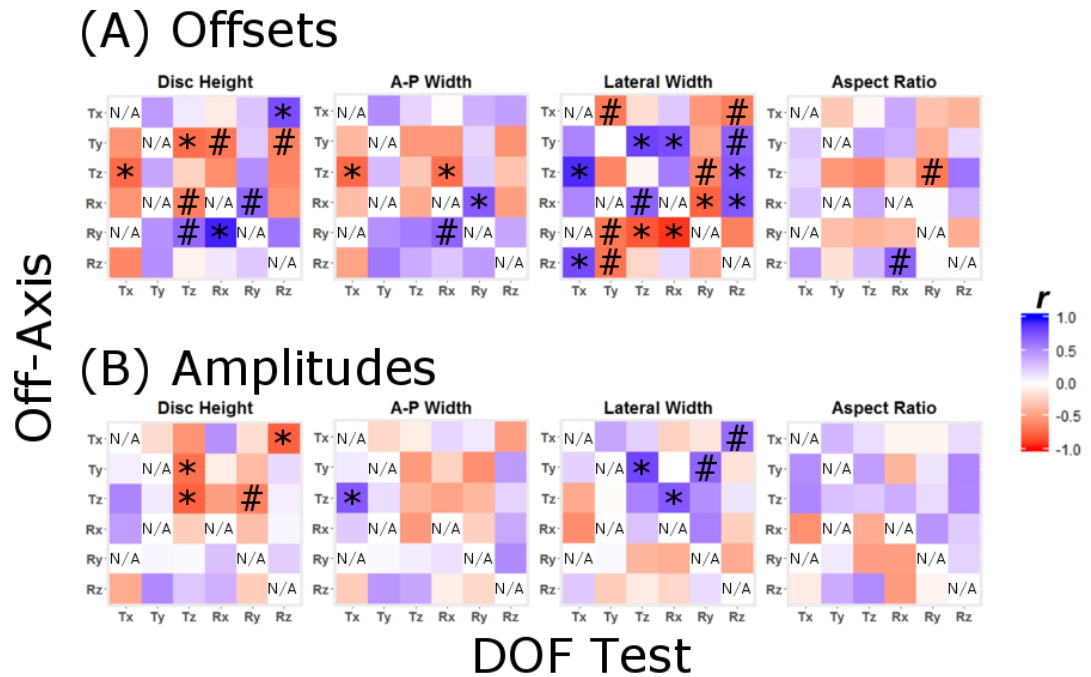


Figure 5-9: Heat maps showing correlations between disc geometry and offsets (A) and amplitudes (B) for each axis in each DOF test for the slow rate. Offsets were strongly correlated with geometry (top row), particularly lateral width, while amplitudes were generally not correlated with geometry (bottom row).

Discussion

This study quantified the mechanical behavior of the intervertebral disc in all six degrees of freedom, measured the coupling between applied loading and off-axis motion, and evaluated the potential role of disc geometry in these mechanical behaviors. All off-axis displacements and rotations were significantly correlated with the applied DOF and were of similar magnitude as physiologically relevant motion, confirming that off-axis coupling is an important mechanical response. Interestingly, there were pairs of DOFs that were especially strongly coupled: lateral shear (Tx) and lateral bending (Ry), anterior-posterior shear (Ty) and flexion-extension (Rx), and compression (Tz) and torsion (Rz). The large offsets in lateral bending and flexion-

extension are consistent with the prior observation that bending and flexion generate the highest shear strains in the disc [166]. Large off-axis shears may contribute to injury risk in bending and flexion. Importantly, the large coupled motions observed in this study were caused by the disc alone, as the facet joints were removed. In addition, the disc responded to shear (T_x , T_y) and rotational loading (R_x , R_y , R_z) by increasing in disc height in order to maintain the applied compressive load. This increase in disc height may be caused by an increase in intradiscal pressure during multiaxial loading [171].

The average same-axis stiffnesses in this study were comparable to those from those reported in literature for tests in lateral shear, A-P shear, compression, and torsion [71]. Flexion (0.13 Nm/deg) and bending (0.92 Nm/deg) stiffnesses tended to be lower than those reported in the literature for flexion (2.3 Nm/deg) and bending (3.4 Nm/deg) stiffness [69]. This may be due to the lower compressive load (0.2 MPa) used in this study than in the other flexion and bending (0.4 MPa) tests. Axial load significantly affects the rotational and compressive stiffness of the disc [80]. Studies which have used comparable axial follower loads (~0.2 – 0.3 MPa) to those in this study have reported similar compressive stiffnesses [71] while those which use larger follower loads have a corresponding higher stiffness [69]. Axial loads during testing, and thus NP pressurization, are critical for disc mechanics. Comparisons between studies and application of reported values should be done with due attention to the axial loads applied and the expected resulting NP pressures.

This study demonstrated that disc geometry correlates with the same-axis stiffness in all six DOFs and with some off-axis responses. In particular, the disc's aspect ratio (lateral width / A-P width) was a significant indicator of rotational and shear stiffnesses, whereas disc height was significantly correlated with compressive stiffness. In addition, lateral width was significantly correlated to each off-axis offset. The observation that lateral width significantly correlates with stiffness and off-axis offsets may be related to the fact that lateral width is the largest dimension of the disc and hence the largest contribution to its moment of inertia. These correlations demonstrate that geometry affects off-axis DOF coupling and therefore contribute to the forces and moments generated in the disc during physiological loading. Furthermore, the relationship between geometry and mechanics may be important for the validation and interpretation of finite element models. Geometry is a known indicator of disc mechanics [100] and typically one geometry is used to represent the disc when developing a finite element model. When reviewing the model's predictions for multiaxial stiffnesses, one should put its simulated stiffness in the context of the model's geometry and the available data relating mechanics to disc geometry.

The discs used in this study were isolated discs without posterior elements, demonstrating that the isolated disc has large coupled motions even without the facets. Facets have a role in spine mechanics and may produce different off-axis effects at the spine scale. Existing literature includes no information on the impact of facets on off-axis responses, and there is conflicting reports regarding their impact on same-axis stiffness. In position control tests, discs with facets had 60-100% higher compressive

and rotational stiffness than those without, [80] whereas in hybrid control tests, discs with facets showed no discernible difference in stiffness compared to isolated bone-disc-bone segments [72]. Additional experiments with facets are needed to determine the relative role of the disc and the facets in 6 DOF mechanical responses. Another limitation of this study was the use of grade 2 to 3 mild/moderately degenerated discs. It remains unknown whether the coupled response measured here would be different with more advanced degeneration.

A strength of this study is the hybrid control approach used in the mechanical testing, where the applied DOF is position controlled (except for axial compression T_z) while the off-axis is force and moments controlled, with physiological axial compression applied throughout. Choices made when designing mechanical testing protocols, such as position vs. load control, are known to effect the mechanical response [40, 72]. Typical experiments control 1 to 2 DOFs. Some studies have investigated combined loading including compression and torsion [37, 171], combined rotational DOFs [91], and compression and flexion [164]. One objective when choosing a testing protocol is to place it in the context of, and preferably simulate, in vivo conditions, thus enhancing translation of experimental results. Although in vivo loads are not completely known, it is certain that disc physiologically experiences 6 DOF loading from a combination of body weight and muscle forces [176-178]. The 6 DOF hybrid testing system in this study has the key advantage of being able to replicate 6 DOF in vivo loading [173]. Although this study perturbed each DOF in

turn, these tests demonstrated that all 6 DOFs are coupled and that combined hybrid control and measurement of all 6 DOFs is essential to fully measure disc mechanics.

The measured off-axis coupling and their relationships with geometry are important to improve the design and evaluation of disc implants. Conventional design and evaluation of implants are limited to 1-2 DOFs [179] but this study showed that large off-axis effects are generated during disc loading and that they are related to the disc's geometry. If not accounted for, these may contribute to implant failure, expulsion, or reduced function. Moreover, these results suggest the need for a patient-specific approach to implant design in order to account for the correlation in mechanics with geometry. For example, bending in discs that have a larger lateral width may increase AF stresses and/or cause expulsion of the implant. Moreover, if an implant is designed without considering the off-axis loads, the implant itself may fatigue due to large loads generated by the coupled off-axes. Lastly, when a disc undergoes discectomy (changing the disc structure) or is replaced with an implant (changing the material), the stiffness in each of the 6 DOFs and their coupled off-axis responses will be altered. These factors should be considered in the design and evaluation of disc implants and other treatments.

In conclusion, this study quantified strong mechanical coupling between DOFs in 6 DOF hybrid-control mechanical tests of the intervertebral disc, and demonstrated the this mechanical coupling varied with disc geometry. This multiaxial coupling and its interaction with geometry should be addressed in the design and evaluation of disc implants. This will likely require increased usage of multiaxial test equipment and

consideration of patient-specific disc geometry. Combined control and measurement of all 6 DOFs is needed to account for the multiaxial loads and their coupling experienced by the in vivo disc, and hybrid control multiaxial testers are well-suited for this application.

Chapter 6

AIM 4 – INCORPORATING RESIDUAL STRESS AND STRAIN IN A FINITE ELEMENT MODEL OF THE INTERVERTEBRAL DISC USING MULTIGENERATION CONSTITUTIVE MODELING IMPROVES MODEL PREDICTIVE CAPABILITIES IN MULTIAXIAL LOADING

The intervertebral disc undergoes significant 6 degree-of-freedom (DOF) dynamic loads under daily activity. To perform the disc's functions the nucleus pulposus (NP) must be hydrated to withstand compression, the annulus fibrosus (AF) must be stiff enough to support tensile loads, and the cartilage endplate (CEP) must permit fluid flow through the bone-disc interface. The combination of these behaviors results in disc mechanics that are complex: it has nonlinear, anisotropic, viscoelastic, biphasic, and osmotic properties. Finite element (FE) models of the disc aim to incorporate these mechanical behaviors to predict the disc's multiaxial mechanics. FE models should be constructed to reflect the disc constituent (e.g. NP, AF, and CEP) mechanical properties and validated against disc mechanical data. To acquire mechanical properties, disc constituents are dissected and tested in isolation allowing for measurement of constituent-specific properties [16, 52]. However, significant residual stresses are present in the intervertebral disc annulus fibrosus in the absence of external applied loads and dissection releases these stresses [96, 97, 180]. The AF mechanical properties obtained have therefore been tested in a reference state different

from the AF of intact discs and the effect of residual stress is excluded from measurement of tissue properties. This presents a challenge to FE model validation as the intact discs used for validation of FE models contain residual stresses while the AF samples used to acquire material properties for FE models are tested with residual stresses excluded. To remedy this issue, AF mechanical properties are tuned to validate disc FE models against intact disc experiments. A method to incorporate residual stresses in disc FE models is therefore needed.

Soft tissue residual stresses arise from osmotic swelling and fiber pre-stress due to growth and remodeling [92, 98, 99]. Swelling residual stresses arise from osmotic pressure induced by the negatively charged glycosaminoglycans of the tissue which result in water imbibing. The water movement into the tissue results in tension of the solid matrix and thus, residual stresses. Swelling is known to play an important role in disc mechanics by restoring hydration of the NP and imparting circumferential stress in the AF [76]. As such, disc FE models routinely include the contribution of swelling using several methods including fixed osmotic gradient [181] and Donnan osmotic swelling [76, 136]. While these techniques are able to capture the swelling of an intact cadaveric disc, the additional residual stresses arising from fiber pre-stress remain unaccounted for in FE models. Quantifying residual stresses in the AF can be valuable for FE models by providing a metric to ensure the AF is in sufficient tension prior to applied loading. Experimental efforts to determine AF residual stresses include incision of intact bovine AF and measuring the opening angle [96, 97]. These experimental efforts have demonstrated that the unloaded disc has residual stresses in

the form of circumferential hoop stress in the AF. While swelling residual stresses are commonly included in disc FE models, a method to incorporate fiber pre-stress is needed.

Multigeneration modeling is an approach that treats a tissue as a mixture of solid components, each with a distinct reference configuration [182]. This allows for interstitial growth of a tissue by deposition of successive “generations” of solids each with its own reference configuration. In the context of the intervertebral disc, a multigeneration approach allows for the extrafibrillar matrix of the AF to be modelled with a different reference configuration from that of the two oppositely-oriented fiber families within the AF ($+\theta$ and $-\theta$). The fibers can be deposited in configurations where the disc has been loaded and after returning the disc to its usual neutral position, the fibers will be pre-stressed in circumferential tension.

This study was designed to identify if incorporating residual stresses from both swelling and fiber pre-stress improves FE model performance in multiaxial loading. First, a method to incorporate residual stress in the AF collagen fibers by applying a multigeneration constitutive modeling approach in FEBio was developed. This was accomplished by a parameter selection routine where fibers were deposited at various degrees of disc torsion rotation and disc bulge and simulated in compressive creep. The resulting creep displacement and disc shape after loading were compared to experimental data. After multigeneration parameters were selected, the multigeneration FE model was simulated in multiaxial loading and compared to an FE model that only included swelling residual stresses. The two FE models were

compared to experimental disc segment testing in multiaxial loading. The results of this study are discussed in terms of the role of residual stress in disc mechanics and the implications of residual stress on FE validation.

2. Methods

In FEBio [183] two finite element models were developed: one with residual stress arising only from swelling, and one that incorporates both swelling and multigeneration residual stresses. Throughout this paper these models will be labeled as “Swelling” and “Multigeneration”, respectively. The Swelling model was previously developed and validated in quasi-static compression but was not compared to dynamic loading [136]. The Multigeneration model requires additional parameters for timing the deposition of collagen fibers, therefore we ran a parameter selection routine by comparing simulated creep results to experimental data of disc shape [184] and disc creep (Chapter 5) . After obtaining the Multigeneration parameters, the predictive capabilities of the two FE models were compared against a multiaxial loading experimental dataset.

2.1 Intervertebral Disc Finite Element Model

Previously we developed an FE model of the intervertebral disc [136] with geometry determined by shape analysis of MR images [102] and constitutive properties determined at the tissue-level [52, 65]. This model was validated against time-dependent stress-relaxation, creep, and slow-ramp quasi-static axial compression loading conditions [67]. This model was further validated by comparing FE-calculated

internal strains under quasi-static loading against MRI-calculated internal strains [184].

Disc constituents (NP, AF, and CEP) were represented by biphasic-swelling constitutive relationships which capture the contributions of fluid flow, osmotic swelling, and elastic matrix to each tissue's mechanics. A tissue's stress ($\boldsymbol{\sigma}$) can therefore be represented as the sum of fluid pressure (p) osmotic pressure (p_{OSM}), and elastic matrix stress ($\boldsymbol{\sigma}^e$):

$$\boldsymbol{\sigma} = -(p + p_{OSM})\mathbf{I} + \boldsymbol{\sigma}^e \quad (7)$$

where \mathbf{I} is the identity tensor. Hyperelastic strain energy density constitutive models were used to represent the elastic matrix, which can be represented by the addition of an isotropic component and an anisotropic component thus defining the total strain energy density as:

$$\Psi_{MATRIX} = \Psi_{ISO} + \Psi_{ANISO} \quad (8)$$

For the NP and CEP, only an isotropic formulation was used while the AF is defined by both isotropic and anisotropic terms due to the contributions of alternating collagen directions. The isotropic component for each tissue was a compressible Holmes-Mow formulation

$$\Psi_{ISO} = \frac{c_1}{I_3^\beta} (e^{[c_2(I_1-3)+c_3(I_2-3)]} - 1) \quad (9)$$

where $I_1 - I_3$ are strain invariants defined as:

$$I_1 = tr\mathbf{C}; I_2 = \frac{1}{2}[(tr\mathbf{C})^2 - tr(\mathbf{C}^2)]; I_3 = det\mathbf{C} \quad (20)$$

and $c_1 - c_3$ are related to modulus (E) and Poisson ratio (ν) via:

$$E = 4c_1(c_2 + c_3)(1 + \nu); \nu = \frac{c_3}{c_2 + 3c_3} \quad (31)$$

For the annulus fibrosus, the anisotropic component is defined by two fiber populations modeled using a toe-linear constitutive model [46]:

$$\Psi_{\text{ANISO}} = \begin{cases} 0, & I_n < 1 \\ \frac{\xi}{2\beta} (I_n - 1)^\beta & 1 \leq I_n \leq I_0 \\ E \left(I_0^{\frac{1}{2}} - I_n^{\frac{1}{2}} \right) + B(I_n - I_0) + \psi_0 & I_0 < I_n \end{cases} \quad (42)$$

$$\xi = \frac{E(I_0 - 1)^{2-\beta}}{2(\beta - 1)}, \quad B = \frac{E}{2} \left[\frac{(I_0 - 1)}{2(\beta - 1)} + I_0 \right], \quad \psi_0 = \frac{\xi}{2\beta} (I_0 - 1)^\beta$$

where I_0 is the square of the fiber stretch ratio when the toe-region transitions to the linear region, E is the fiber modulus in the linear range, β is the power-law exponent in the toe-region, and I_n is the invariant for a fiber family given by $I_n = \mathbf{a} \cdot \mathbf{C} \cdot \mathbf{a}$ where \mathbf{a} is the fiber orientation vector and \mathbf{C} is the right Cauchy-Green deformation tensor. Each tissue's hydraulic permeability was defined using a strain-dependent Holmes-Mow permeability

$$k(J) = k_0 \left(\frac{J - \phi_0}{1 - \phi_0} \right)^2 e^{M(J^2 - 1)/2} \quad (53)$$

where k_0 is the permeability in the reference state, J is the Jacobian of the deformation gradient tensor ($J = \det \mathbf{F}$), ϕ_0 is the hydration in the reference state, and M is a

nonlinearity parameter. The effect of fixed charge density was represented by a Donnan equilibrium term:

$$p_{OSM} = RT \left(\sqrt{c_{FC}^2 + 4c_B^2} - 2c_B \right) \quad (64)$$

where p_{OSM} is the osmotic pressure, R is the universal gas constant, T is absolute temperature, c_{FC} is the fixed charge density, and c_B is the bath osmolarity. Fixed charge density is a function of volumetric change in the tissue as defined by:

$$c_{FC} = \frac{c_{FC0}\phi_0}{J-1+\phi_0} \quad (75)$$

where c_{FC0} is the fixed charge density in the reference state. The properties used in the FE model for each tissue are summarized in Table 6-1. The properties listed for the inner AF and outer AF represent the properties at the inner-most AF lamella and the outer-most AF lamella, respectively. The lamellae in between these two had properties that were linearly-interpolated element-wise to account for the gradient in biochemistry, fiber angle, and mechanical property deviations from inner to outer AF [27, 46, 185]. The fiber angle varied from 25° in the outer AF to 40° in the inner AF.

Table 6-1: Properties for the Finite Element Model

Tissue	Matrix			Permeability		Biochemistry		Fibers		
	E (kPa)	ν	β	$k_0 10^{-16}$ (m ⁴ /Ns)	M	Φ^w	FCD (mEq/L?)	E (MPa)	β	λ_0
NP	64.9	0.24	0.95	5.5	1.92	0.79	379	-	-	-
IAF	26	0.16	2.1	25	3.5	0.77	55	3.3	4	1.30
OAF	18	0.24	0.16	47	5.75	0.77	44	26	4	1.17
CEP	305	0.18	0.29	5.6	3.79	0.60	248	-	-	-

2.2 Multigeneration Modeling

Two types of residual stress need to be incorporated into the disc FE model: residual stresses arising from tissue swelling in PBS and residual stresses arising from tissue growth. The Donnan equilibrium model is responsible for tissue swelling, but a strategy needs to be devised to incorporate the stresses arising from tissue growth. Multigeneration constitutive modeling allows defining different reference states for every constituent in a model [182, 186]. Briefly, a given body can be deformed from a global reference configuration, \mathbf{X} , (Figure 6-1A) to a new, intermediate reference configuration, \mathbf{X}^I (Figure 6-1B), where the subscript indexes the new generation deposited. Therefore, for the deformed body with spatial configuration (\mathbf{x}) the overall deformation gradient is \mathbf{F} (Figure 6-1C) and the relative deformation gradient for the new generation, \mathbf{F}^I , can be derived using the chain rule of differentiation as:

$$\mathbf{F} = \frac{\partial \mathbf{x}}{\partial \mathbf{X}} = \frac{\partial \mathbf{x}}{\partial \mathbf{X}^I} \frac{\partial \mathbf{X}^I}{\partial \mathbf{X}} = \mathbf{F}^I \mathbf{\Pi}^I$$

In the context of disc FE models this approach is advantageous for defining collagen fibers of the AF in a different reference state from the rest of the disc, allowing for pre-stressing of the fibers. The multigeneration strategy in this work aimed to define a different reference state for each family of AF fibers (e.g. +25° fibers, -25° fibers) while the remaining disc components (NP, CEP, and AF extracellular matrix) were all referenced to the usual stress-free geometry of the disc. The AF reference states were defined by fixing the two vertebral bodies in five DOFs (x, y, z, flexion, and bending) and rotating the disc in torsion + Ω° , depositing the $-\theta$ family of fibers, then rotating

the disc $-\Omega^\circ$ in torsion and depositing the $+\theta$ family of fibers before bringing the disc back to the neutral position (Figure X-A). After bringing the disc back to the neutral position, the disc swelling was simulated in 0.15M PBS under 50N axial preload per the experimental protocol. To determine the value for disc twist (Ω), a parametric study was performed and the resulting disc mesh shapes were compared to the preload template shape. Combinations of stress-free meshes with initial disc bulge (0, 0.5, 1.0, or 1.5 mm) underwent the pre-stress routine with different disc twists (0, 1, 2, 3, or 4°). Pre-bulged meshes are essential to counter the inward bulging that arises from rotating the disc. Each combination of initial bulge and disc twist produces a resulting disc bulge. This resulting disc bulge was compared to the disc bulge from our prior MRI strain work at 50N preload [184]. In this study disc twist and initial disc bulge are referred to as “multigeneration parameters”.

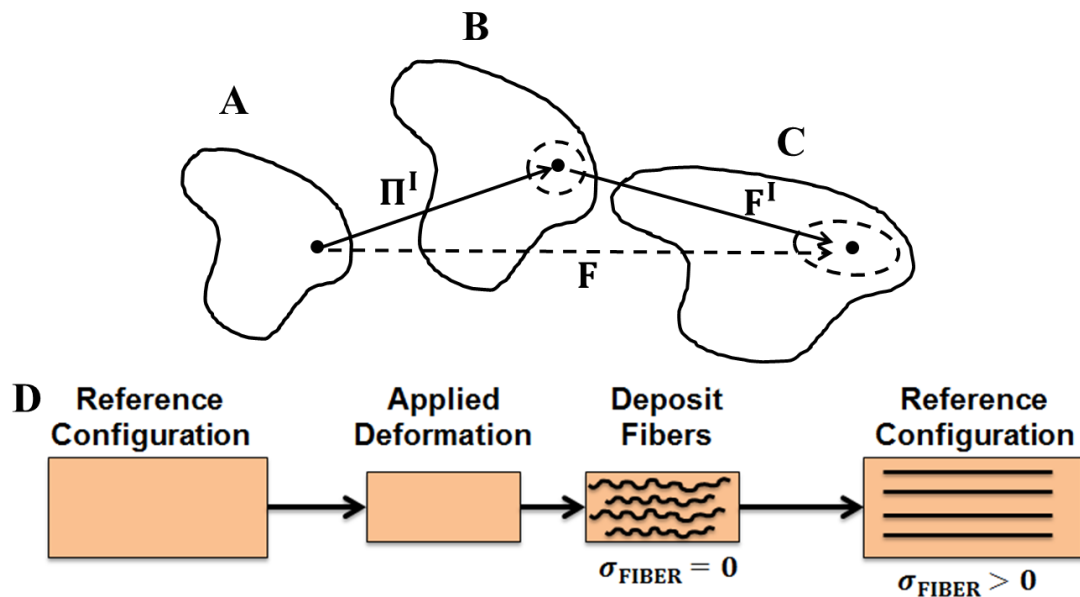


Figure 6-1: Schematic of multigeneration modeling. A body in a master reference configuration (A) undergoes a deformation Π^I to an intermediate state (B) that serves as the reference configuration for the constituent outlined with the dotted circle. The body continues to deform to the final state (C) with a deformation gradient \mathbf{F} for the initial body and a deformation gradient \mathbf{F}^I for the outlined constituent. In the context of the disc, this approach may be applied to the deposition of collagen fibers (D). The tissue can be deformed from its reference configuration, the fibers can be deposited so that when the applied deformation is undone, the fibers become stressed.

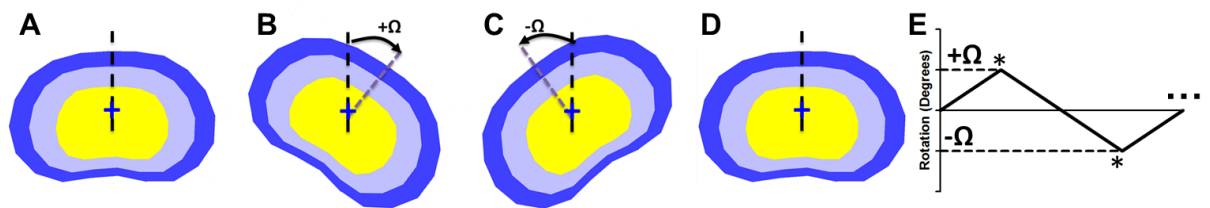


Figure 6-2: Method for multigeneration deposition of collagen fibers. The disc starts at its reference configuration (A) and undergoes a disc twist $+\Omega$ where the $-\theta$ family of collagen fibers are deposited (B). Then, the disc undergoes the opposite twist $-\Omega$ and the $+\theta$ family of collagen fibers are deposited before being returned to the reference configuration (D). (E) illustrates this schematic and is repeated for each lamellae of the AF.

2.3 Multiaxial Mechanical Loading – Specimen Preparation

Cadaveric human lumbar intervertebral discs ($n = 6$) from 6 spines (4M/2F; age 50 ± 8 yrs.) were imaged, graded for degeneration, and dissected with posterior elements removed. The sample set was selected to be moderately degenerate to further validate in multiaxial loading our previously validated moderately degenerate FE model in quasi-static compression [136]. The disc's geometry was determined from lateral and coronal x-ray images and the disc's axial area was estimated from $A = 0.84 * W_{AP} * W_{LAT}$ where W_{AP} and W_{LAT} are the anterior-posterior and lateral widths of the disc, respectively and 0.84 is an empirically determined scaling factor to account for the disc's kidney-bean shape [172]. The compressive preload force was then calculated to obtain a pressure of 0.2 MPa in the nucleus pulposus. Each disc was thawed under 50N compression in 0.15M PBS overnight. After thawing, three k-wires were placed into each vertebra at 120° apart and the disc was potted in PMMA.

2.4 Mechanical Testing

The potted disc was attached to a hexapod robot in a bath of 0.15M PBS heated to 37°C and a 0.2 MPa axial compression preload was applied and held for 12 hr. multiaxial mechanical testing was performed such that the sequence minimizes disc volume lost during testing: lateral shear, anterior-posterior shear, torsion, lateral bending, flexion-extension, and compression. Shear and rotation DOFs testing was performed at 5 sinusoid cycles each of 3 rates (0.5 Hz, 0.05 Hz, 0.005 Hz) from the fastest rate to the slowest rate followed by a 30 minute creep recovery at the preload

force. Compression loading was performed at 5 haversine cycles each of 1 Hz, 0.1 Hz, and 0.01 Hz with 30 minute creep recoveries after 0.1 Hz and 0.01 Hz.

2.5 Data Analysis

The two FE models were compared to one another as well as the experimental results for both load-displacement curves and stiffness. The loading phase of the final cycle (e.g. 5th cycle) of the slowest loading rate was used for comparison. The mean and 95% confidence interval (CI) of each loading phase was used for comparison. Stiffness was calculated between 70-90% of each loading phase of the final cycle (Figure 3).

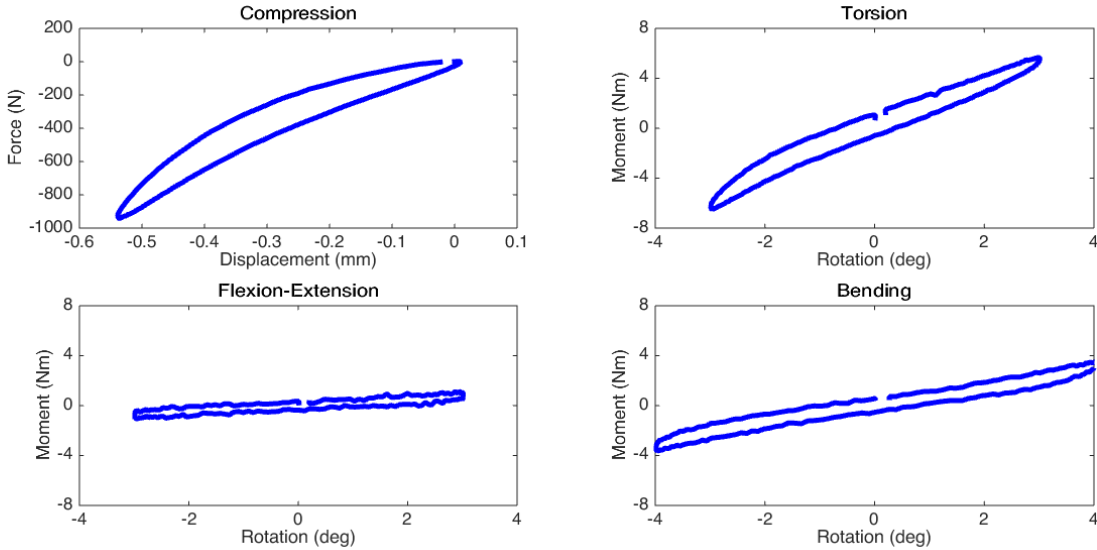


Figure 6-3: Example load-displacement curves for each degree-of-freedom

3. Results

3.1 Parameter Selection

Parameter selection was achieved by simulating combinations of disc bulge and disc twist in 50N axial compression and 0.2 MPa overnight creep to get metrics for disc shape and disc mechanics, respectively. The minimum resulting disc bulge from the simulations was 1.2 mm when 4° of disc twist and 0 mm of disc bulge were simulated, and the maximum resulting disc bulge was 3.3 mm when 2 mm of disc bulge and 0° of disc twist were simulated. The minimum overnight creep displacement was 1.02 mm when 4° of disc twist and 0 mm of disc bulge were simulated. The resulting surfaces from these simulations intercepted with the experimental values for disc creep (1.05 mm) and disc bulge (1.45 mm) (Figure 4). The intercept of the two black lines in Figure 4 gives the pair of disc bulge and disc twist that fit both metrics, disc bulge = 0.25 mm and disc twist = 3.8°. These multigeneration parameters lead to residual strains of 0.04 ± 0.04 throughout the AF.

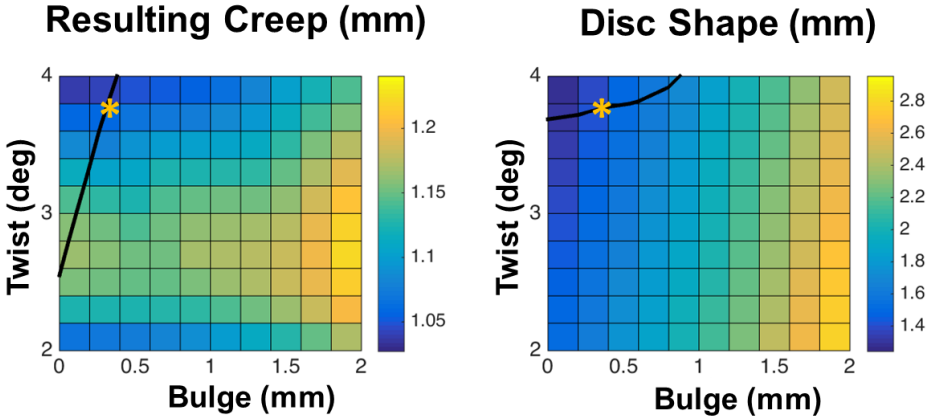


Figure 6-4: Parameter selection results for multigeneration parameters.

3.2 Finite Element Validation

The Swelling and Multigeneration models were simulated in compression, torsion, flexion-extension, and bending and the loading portion of the 5th cycle of the FE models was compared to that of the experimental data and its 95% confidence interval. The Swelling model produced an elongated neutral zone in compression and a resulting load-displacement curve that was outside of the experimental confidence interval (Figure 5A). The addition of fiber pre-stress led to a decrease in the neutral zone and a shift in the load curve up to the experimental confidence interval. In torsion, the Swelling model under-predicted the torsion moment while the Multigeneration model predicted a torsion load-displacement curve within the experimental confidence interval (Figure 5B). Similarly, the Swelling model under-predicted the bending moment while the Multigeneration model predicted a bending load-displacement curve within the experimental confidence interval close to the mean of the data (Figure 5C). In flexion-extension, the swelling only model predicted a load-displacement curve within the experimental confidence interval while the Multigeneration model predicted a load curve outside of the experimental window (Figure 5D). However, the experimental moment magnitudes in flexion-extension tended to be small (<0.5 Nm) and the Multigeneration model predicted the smallest moment magnitude in flexion-extension (0.88 Nm).

The linear-region stiffnesses for each DOF were compared between the two FE models and the experimental data. While the Swelling model had an elongated neutral

zone in compression, the model did achieve linear-region stiffness (2150 N/mm) at the mean of the experimental data (2140 ± 510 N/mm) (Table 6-2). The Multigeneration model preserves the linear region stiffness of the disc (2140 N/mm) and is likewise within the experimental standard deviation. The torsion stiffness (0.45 Nm/deg) of the Swelling model was 1.9 standard deviations away from the experimental mean (1.94 ± 0.8 Nm/deg) while the Multigeneration model (0.95 Nm/deg) was 1.2 standard deviations away from the experimental mean. In lateral bending, the Swelling model generated a stiffness (0.27 Nm/deg) that was 1 standard deviation away from the experimental mean (0.75 ± 0.48 Nm/deg) while the Multigeneration model produced a stiffness (0.56 Nm/deg) within the experimental standard deviation. The Swelling model produced a flexion stiffness (0.10 Nm/deg) within the experimental standard deviation (0.05 ± 0.07 Nm/deg) while the Multigeneration model produced a flexion stiffness (0.28 Nm/deg) that was outside of one standard deviation of the mean.

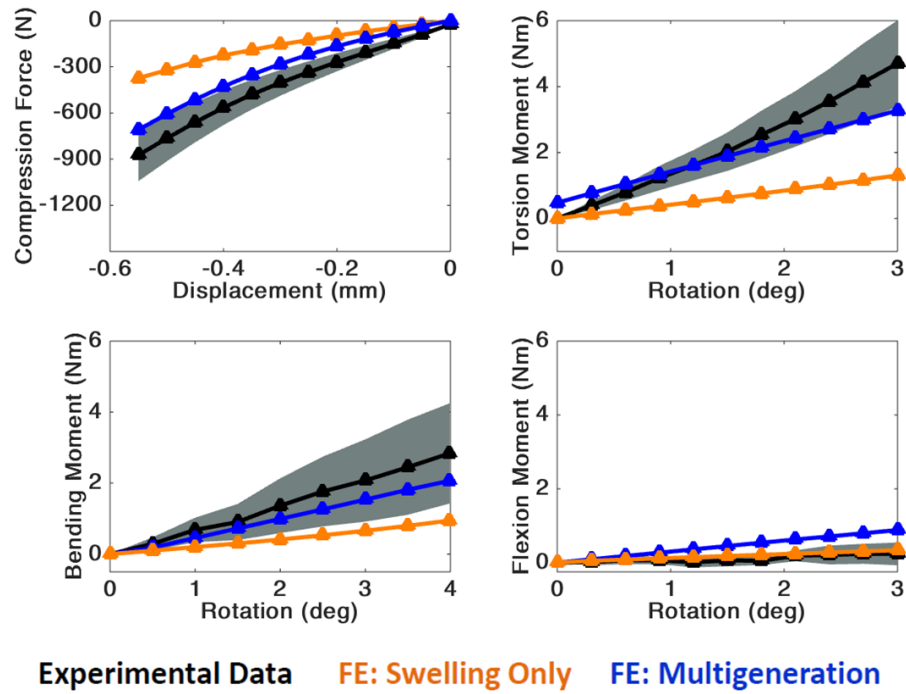


Figure 6-5: Validation results for multiaxial loading

Table 6-2: Comparison of multiaxial stiffnesses between experiment data, the Swelling model, and the Multigeneration model

	Compression (N/mm)	Torsion (Nm/deg)	Flexion- Extension (Nm/deg)	Bending (Nm/deg)
Experiment	2140±510	1.94±0.80	0.05±0.07	0.75±0.48
Swelling	2150	0.45	0.10	0.27
Multigeneration	2140	0.95	0.28	0.56

4. Discussion

The objective of this study was to identify if incorporating residual stresses from both swelling and fiber pre-stress improves FE model performance in multiaxial loading. A novel multigeneration modeling approach was developed to deposit the collagen fibers of the AF at different reference states from the extrafibrillar matrix of

the disc, increasing their residual stress (fiber pre-stress). Including both sources of residual stress resulted in increased stiffness in all rotational DOFs without compromising disc compressive stiffness and generated load-displacement curves within the experimental data, indicating that the multigeneration modeling approach successfully improved the model's predictive capabilities in multiaxial loading. A primary advantage of this approach is that it allows for the material properties measured experimentally to be used without tuning the properties themselves, but rather the reference state of the fibers within the model.

Discs with no external load are known to have significant residual stresses in the form of circumferential hoop stress [96, 97]. In particular, the proteoglycan-rich NP creates significant osmotic pressure, driving fluid into the disc, causing the NP to swell and impart circumferential tensile stresses on the AF. This interplay between the swelling of the NP and stress development in the AF may significantly affect the mechanics of the disc as a whole. Prior studies on the effects of nucleotomy have demonstrated an elongated neutral zone in compression while the linear-region stiffness remains unchanged [187]. The disc must be at a higher compressive displacement for the AF to be engaged, resulting in the linear-region seen in the load-displacement curve. This pattern of behavior is also observed in comparing the two FE models in the present study. The Swelling model produces an elongated neutral zone with linear-region stiffness comparable to the experimental data, while the Multigeneration model produces a smaller neutral zone and similar linear-region stiffness. This suggests that the Swelling model produces a stress state in the AF that

is too low compared to the experiment. The addition of fiber pre-stress in the Multigeneration model remedies this inconsistency between the FE simulations and the experimental data.

Including both swelling and fiber pre-stress residual stresses also validated the disc FE model in multiple loading modalities (compression, torsion, bending, and flexion) by comparing the FE-predicted load-displacement curves and stiffness values to the experimental counterparts. Using the full load curves as a metric for validation in this study highlights the importance of expanding validation criteria beyond single time-points (e.g. end-point displacement of a loading condition). Simply using stiffness as a metric would falsely lead to the conclusion that the Swelling model correctly predicts disc compression. While it is true that the Swelling model's linear-region stiffness matches the experimental stiffness, the neutral zone is wider in the model than in the experiment. Moreover, the constitutive model material properties and the multigeneration parameters (disc twist and disc bulge) were derived from tissue-level testing and disc-level axial compression tests and weren't tuned post-hoc to match the experimental multi-axial load curves. Separating the experiments for model development and model validation, coupled with using load-displacement curves and disc stiffness values, makes the validation more thorough and strengthens the predictive capabilities of the model.

While the source of swelling residual stresses, osmotic pressure due to the proteoglycan-rich NP, is known, the specific source of the collagen fiber pre-stress remain unknown. In general, the reference configuration for biological tissues is

unknown due to the complexities associated with tissue growth and remodeling. In the context of the disc, the lamellar structure of the disc forms early in embryogenesis with AF cells orienting in the classic angle-ply structure of the AF, creating the template for collagen organization [188, 189]. The lamellae thicken, particularly in the inner AF, as a result of matrix deposition in early development [190, 191] which may impart tensile stresses on the collagen of the AF. Beyond the early stages of development, however, the AF has limited capacity for remodeling and repair, and it remains unclear how the growth of the spine affects collagen fiber stress in the AF. Given that the reference state of the AF collagen fibers is unknown, the Multigeneration model in this study aimed to be a surrogate for the residual stresses generated from deposition and growth of AF collagen fibers physiologically. Although this multigeneration approach is a surrogate for the physiological processes, the values for strain are comparable to those predicted from opening-angle experiments in bovine caudal discs. The Multigeneration model predicted circumferential hoop strains of ~ 0.04 in the outer AF, comparable to the 0.02 ± 0.09 strains from [96]. However, the discs used in these studies were bovine discs and it is unclear how differences in human disc shape, size, hydration, and biochemical composition would affect its residual stress magnitude and distribution. Furthermore, the effect of the degenerative cascade on residual stresses in the human disc remains unknown but may be important validating finite element models of the disc in non-degenerate and advanced degenerate states. Future studies identifying the specific mechanisms of residual stress

development in the AF collagen fibers can guide adjustments to the multigeneration constitutive modeling approach in the current study.

In summary, the multigeneration modeling approach used in this study successfully generated residual stresses in the AF collagen fibers, expanding the predictive capabilities of a disc FE model in multiaxial loading. Importantly, the material properties measured in tissue-level testing do not need to be tuned in this approach, but rather a different reference state for the collagen fibers needs to be defined. While the strategy employed to determine the fiber reference states was not physiological, this approach generated a pattern of larger residual strains in the outer AF than in the inner AF that were comparable to those reported in prior opening-angle experiments. Future studies should identify residual strain magnitudes and distributions in human discs to serve as benchmarks for model development and to expand model predictive capabilities in multiaxial loading.

Chapter 7

CONCLUSIONS AND FUTURE WORK

Disc degeneration is a mechanical and biochemical process that alters intervertebral disc mechanics and is strongly associated with low back pain. However the unique structure and function of the disc challenges the study of the degeneration cascade. This challenge has motivated the development of finite element models as non-invasive computational tools to quantify disc mechanics and changes with degeneration. In order for these models to have utility in predicting disc mechanics, they should be formulated to reflect the disc's anatomy and its constituent's mechanical properties. The overall objective of this dissertation was to further develop and validate a finite element model of the disc by incorporating residual stresses and validating the model against experimental multiaxial mechanical data. To achieve this objective, the mechanical properties and anatomy of the cartilage endplate were added to the disc model (Chapters 3 and 4), a multiaxial experimental dataset was generated (Chapter 5), and a novel multigenerational constitutive modeling approach was used to add residual stresses to the model (Chapter 6).

The first aim of this dissertation was to quantify the cartilage endplate's mechanical properties and geometry and their changes with degeneration. In Chapter 3, confined compression experiments were performed on human CEP and the resulting

load curves were curve-fit with a biphasic-swelling constitutive model to obtain mechanical properties. Prior to this study there were two competing hypotheses for CEP permeability changes with degeneration. One hypothesis states that CEP permeability decreases with degeneration, restricting transport of solutes to the cells in the center of the disc and slowing the removal of waste products from the disc, altering the local pH in the NP which may lead to cellular damage. An alternative hypothesis states that CEP permeability increases with degeneration causing a leaking of water out of the disc, reducing disc height and compromising the mechanical integrity of the disc. This study demonstrated that the cartilage endplate's permeability decreases with degeneration, supporting the former hypothesis. It remains unclear what factors cause the decrease in CEP permeability but histological and biochemical analysis demonstrated an increase in fixed charge density in the CEP with degeneration. This may be related to accumulation of proteoglycan fragments from the NP that are slowly expunged in degeneration. In addition, the CEP is known to calcify, and this calcification process is believed to restrict transport through the CEP.

Although this study supports the hypothesis that CEP permeability decreases with degeneration, the alternative hypothesis may be true in advanced degeneration. In advanced degeneration the CEP is prone to damage which may create outlets for fluid flow from the disc, resulting in loss of disc height. Furthermore, this study was the first to include fibers in its model of the CEP mechanics. Including CEP fibers increased the fluid flux across the CEP compared to the model that excluded fibers which suggests models that exclude CEP fibers may underestimate fluid flow across

the bone-disc interface. Ultimately, the mechanical and biochemical properties quantified in this study serve as valuable inputs to the disc FE model and any future studies that aim to look at the progressive change in properties with degeneration can input properties obtained from this study.

In Chapter 4, CEP geometry was quantified and relationships between geometry and aging and degeneration were determined. A novel MRI FLASH technique was used to visualize the CEP and distinguish it from the surrounding NP and bone. Manual measurements of CEP thickness were made from paired MRI and morphological images to confirm that the MRI technique is valid for measuring CEP thickness. This study demonstrated that the CEP thickness is greater at the anterior and posterior boundaries, where the CEP interfaces with the AF, and is thin in the center of the CEP above the NP. This gradient in CEP thickness may be valuable to the CEP's mechanical functions. The CEP needs to be thick enough to provide mechanical support of the interface while containing the NP and needs to be thin enough to allow for solute, water, and waste transport across the interface. For the current dissertation, the average CEP thickness determined in this study served as an input for the disc FE model.

A dataset of multiaxial mechanics was needed for validation and in Chapter 5 a hexapod mechanical testing device was used to load human intervertebral disc segments in a multiaxial mechanical testing sequence. The disc's off-axis mechanics were quantified by determining the amplitude of the off-axis oscillation and the offset of the center of rotation. Large offsets were observed when the disc was driven in

lateral bending and flexion-extension and may be related to the observation that bending and flexion generate the highest shear strains in the disc [166]. Offsets were also correlated with disc geometry, particularly lateral width, the largest dimension in the disc, demonstrating that geometry affects the coupling of degrees-of-freedom in the disc. Stiffnesses and load-displacement curves were also obtained for each degree-of-freedom and served as metrics for validation in Chapter 6. Stiffnesses were correlated with disc geometric parameters, particularly lateral width and disc aspect ratio. Ultimately, this study demonstrates the importance of geometry in multiaxial mechanics of the disc. Future experimental studies as well as finite element models that examine patient-specific biomechanics should consider the patient's disc geometry in analyzing biomechanical data. For the current dissertation, these multiaxial mechanics serve as metrics for validation of a disc FE model.

The final aim of this dissertation integrates the properties obtained from Chapters 3-4 and a multigenerational constitutive modeling approach to residual stresses in the AF to validate a disc FE model in multiaxial loading against the experimental data from Chapter 5. Multigenerational constitutive modeling allows for the definition of model constituents at different reference states (e.g. the reference state for the extrafibrillar matrix and the reference state for the collagen fibers are different). To highlight the effects of this multigenerational constitutive approach, this model, which has residual stresses from both swelling and multigenerational fiber prestress, was compared to a model which only has residual stresses from swelling. The swelling-only model was unable to predict the torsion or bending response of the disc.

While the swelling-only model was able to predict disc compressive stiffness, it simulated an elongated neutral zone that was larger than that of the experimental data. This behavior has previously been observed in nucleotomy studies, wherein the AF is not engaged in circumferential tension under loading due to the removal of NP and therefore the disc has an elongated neutral zone. The model with both sources of residual stress remedies this issue by increasing the stress in the AF and this model was able to predict the compressive, torsion, and bending response of the disc.

7.1 Future Directions

While this work advances the capabilities of disc FE models by providing a technique for incorporating residual stresses, there are several applications for the model as well as features which may be added to the model to expand its utility.

7.1.1 Design of Implants

One potential application of the disc FE model is in the design of NP replacements and therapeutic interventions. An objective of NP implant design is to restore disc height and mechanical integrity to the disc. Often, the materials used in NP implants are hyperelastic polymers rather than biphasic-swelling materials like the NP. The disc FE model can be used to predict the mechanical properties needed for these alternative materials and ensure that these properties are suitable for multiaxial loading as opposed to just compression. A common issue with NP implants is that they are expelled from the disc space. This may be due to the fact that implants are often evaluated using compression testing but the disc experiences significant multiaxial loads physiologically and the locally large compression loads in bending

and flexion may result in expulsion of the implants. In addition, a common theme of NP implant design is the ability to be injected in the disc via puncture of the AF. This places the implant in a complicated mechanical environment where local residual stresses may be released at the puncture site while the AF at the opposite end of the disc remains intact with residual stress. It is known that AF punctures can alter tissue biomechanics and accelerate degeneration [50] and it is hypothesized that the release of residual stresses due to the puncture can compromise disc mechanics [96] and therefore the implant's performance. The current FE model was developed to incorporate residual stresses and the effects of a puncture on local residual stress and implant performance can be uniquely studied using this model.

7.1.2 In Vivo Biomechanics

Another potential application of this FE model is predicting in vivo disc mechanics. In vivo biomechanics are notoriously challenging to quantify due to the tissue's location physiologically and its complicated non-linear, anisotropic, viscoelastic mechanics. At present, the best non-invasive MRI methods provide valuable information regarding tissue's axial strain (in vivo) and the full strain tensor (ex vivo). While these techniques are valuable in quantifying tissue strain, an important indicator of mechanical performance, the tissue's transient behavior, fluid flow, and stresses are all not quantified by these techniques. If the model is validated against these measures of in vivo strain, the model can be used to predict the other mechanical behaviors not captured by MRI. The ability to predict patient-specific in vivo biomechanics has immense potential as loading scenarios which may overload an

individual's disc can be predicted and patient-specific therapeutic interventions can be designed.

7.1.3 Combined Loading Scenarios

A third application of this FE model is simulating combined loading scenarios. Conventionally, disc FE models are used to simulate one DOF at a time. Indeed there is interest in using FE models to predict which DOF causes damaging mechanical overload in the disc. However, it is hypothesized that, physiologically, combined loading scenarios (e.g. torsion and flexion) may result in the loading conditions that lead to locally high levels of tension in the AF, causing local tears. The current model is validated in multiaxial loading and can be used to examine which combined loading scenarios, and which loading magnitudes, are most likely to cause local AF damage and may lead to tears and disc failure.

7.1.4 Additional Features to Expand the FE Model

While the current model has several potential applications, there are several features which can be added to the model to expand its predictive capabilities. First, the current model uses a Donnan equilibrium swelling approach to simulate tissue swelling and does not account for the transient movement of specific non-charged (e.g. glucose) and charged solutes (e.g. Na^+ , Cl^-) into and out of the disc. At present MRI studies have been conducted to analyze the rate of solute flow into the disc over time [104, 192]. However, evaluating many different pharmaceutical solutes can be time consuming and financially costly, presenting challenges to using MRI to study solute transport. Expanding the model from a biphasic-swelling model to a fully

triphasic model enables prediction of solute movement that may be useful in analyzing the diffusion of pharmaceutical interventions aiming to, for example, target the NP to promote cellular activity.

Another feature that could be added to the model is continuum damage mechanics. With aging and degeneration, the disc is known to experience damage in the form of radial and circumferential AF tears, AF and CEP herniations, Schmorl's nodes, and bone-AF interface tears [30, 31, 34, 115]. It is hypothesized that mechanical overload may lead to these failures which are often associated with low back pain. Continuum damage mechanics is an approach that allows the definition of the onset of tissue damage, altering the tissue's mechanical properties and the resulting stress. The ability to define the onset of tissue damage is essential to predicting which loading scenarios are damaging and lead to the aforementioned failures.

If triphasic theory and continuum damage mechanics are implemented in the current model, its predictive capabilities will be unprecedented and will have immense clinical impact. The disc's solute transport and failure scenarios can be predicted enabling use in the design of pharmaceutical interventions like drugs targeting the NP as well as mechanical interventions like implants.

7.2 Summary

Ultimately, the unique structure and complex mechanical behavior of the disc challenges the formulation and validation of disc finite element models in multiaxial loading. This dissertation provides a validated disc FE model in multiaxial loading by incorporating residual stresses via a multigenerational constitutive modeling approach.

While successful multiaxial validation is a useful for step in the utility of the model presented in this dissertation its value will be demonstrated through its future applications in design of interventions, design of experiments, and predicting disc mechanics.

REFERENCES

- [1] G.B.J. Andersson, Epidemiological features of chronic low-back pain, *The Lancet* 354(9178) (1999) 581-585.
- [2] J.P.G. Urban, S. Roberts, Degeneration of the Intervertebral Disc, *Arthritis Res Ther* 5(3) (2003) 120.
- [3] M.A. Adams, P. Dolan, Intervertebral disc degeneration: evidence for two distinct phenotypes, *Journal of anatomy* 221(6) (2012) 497-506.
- [4] X. Luo, R. Pietrobon, S.X. Sun, G. Liu, L. Hey, Estimates and patterns of direct health care expenditures among individuals with back pain in the United States, *Spine* 29(1) (2003) 79-86.
- [5] A.F. Ozer, T. Oktenoglu, M. Sasani, T. Kaner, O. Ercelen, N. Canbulat, Unusual cause of acute low-back pain: sudden annulus fibrosus rupture, *Orthopedic reviews* 4(2) (2012) e22.
- [6] J. Cholewicki, S.M. McGill, Mechanical stability of the in vivo lumbar spine: implications for injury and chronic low back pain, *Clinical biomechanics* 11(1) (1996) 1-15.
- [7] N. Vo, L.J. Niedernhofer, L.A. Nasto, L. Jacobs, P.D. Robbins, J. Kang, C.H. Evans, An overview of underlying causes and animal models for the study of age-related degenerative disorders of the spine and synovial joints, *J Orthop Res* 31(6) (2013) 831-7.
- [8] J. Melancia, A. Francisco, Antunes, Spinal Stenosis, *Handbook of Clinical Neurology* 119 (2014) 541-549.
- [9] M. Rzewuska, M. Ferreira, A.J. McLachlan, G.C. Machado, C.G. Maher, The efficacy of conservative treatment of osteoporotic compression fractures on acute pain relief: a systematic review with meta-analysis, *Eur Spine J* 24(4) (2015) 702-14.
- [10] J.A. Buckwalter, Aging and degeneration of the human intervertebral disc, *Spine* 20(11) (1995) 1307-1314.
- [11] N. Tanaka, H.S. An, T.H. Lim, A. Fujiwara, C. Jeon, V.M. Haughton, The relationship between disc degeneration and flexibility of the lumbar spine, *Spine J* 1 (2001) 47-56.
- [12] B. Vernon-Roberts, R. Moore, R. Fraser, The natural history of age-related disc degeneration: the pathology and sequelae of tears, *Spine* 32(25) (2007) 2797-2804.
- [13] S. Mirza, R. Deyo, Systematic review of randomized trials comparing lumbar fusion surgery to nonoperative care for treatment of chronic back pain., *Spine* 32(7) (2007) 816-823.

- [14] E.N. Hanley, Jr., H.N. Herkowitz, J.S. Kirkpatrick, J.C. Wang, M.N. Chen, J.D. Kang, Debating the value of spine surgery, *The Journal of bone and joint surgery. American volume* 92(5) (2010) 1293-304.
- [15] L.J. Smith, N.L. Nerurkar, K.S. Choi, B.D. Harfe, D.M. Elliott, Degeneration and regeneration of the intervertebral disc: lessons from development, *Dis Model Mech* 4(1) (2011) 31-41.
- [16] W. Johannessen, D. Elliott, Effects of degeneration on the biphasic material properties of human nucleus pulposus in confined compression, *Spine* 30(24) (2005) E724-E729.
- [17] G. Pattappa, Z. Li, M. Peroglio, N. Wismer, M. Alini, S. Grad, Diversity of intervertebral disc cells: phenotype and function, *Journal of anatomy* 221(6) (2012) 480-96.
- [18] S. Roberts, J. Menage, J.P. Urban, Biochemical and structural properties of the cartilage end-plate and its relation to the intervertebral disc, *Spine* 14 (1989) 166-174.
- [19] D.R. Eyre, Biochemistry of the intervertebral disc, *Int Rev Connect Tissue Res* 8 (1979) 227-291.
- [20] T.R. Oegema, Biochemistry of the intervertebral disc, *Clinical Sports Medicine* 12(3) (1993) 419-439.
- [21] S.S. Sivan, A.J. Hayes, E. Wachtel, B. Caterson, Y. Merkher, A. Maroudas, S. Brown, S. Roberts, Biochemical composition and turnover of the extracellular matrix of the normal and degenerate intervertebral disc, *Eur Spine J* (2013).
- [22] J. Antoniou, N. Goudsouzian, T. Heathfield, N. Winterbottom, T. Steffen, A. Poole, M. Aebi, M. Alini, The Human Lumbar Endplate, *Spine* 21(10) (1996) 1153-1161.
- [23] W. Johannessen, J.D. Auerbach, A.J. Wheaton, A. Kurji, A. Borthakur, R. Reddy, D. Elliott, Assessment of human disc degeneration and proteoglycan content using T1rho-weighted magnetic resonance imaging, *Spine* 31(11) (2006) 1253-1257.
- [24] A. Maroudas, R. Stockwell, A. Nachemson, J. Urban, Factors involved in the nutrition of the human lumbar intervertebral disc: cellularity and diffusion of glucose in vitro, *Journal of anatomy* 120(1) (1975) 113-130.
- [25] J. Urban, S. Smith, J. Fairbank, Nutrition of the intervertebral disc, *Spine* 29(23) (2004) 2700-2709.
- [26] G.D. O'Connell, E.J. Vresilovic, D.M. Elliott, Comparison of Animals Used in Disc Research to Human Lumbar Disc Geometry, *Spine* 32(3) (2007) 328-333.
- [27] J.J. Cassidy, A. Hiltner, E. Baer, Hierarchical Structure of the Intervertebral Disc, *Connective Tissue Research* 23 (1989) 75-88.
- [28] J. Antoniou, T. Steffen, F. Nelson, N. Winterbottom, A. Hollander, R. Poole, M. Aebi, M. Alini, The human lumbar intervertebral disc: evidence for changes in the biosynthesis and denaturation of the extracellular matrix with growth, maturation, ageing, and degeneration., *J Clin Invest* 98(4) (1996) 996-1003.
- [29] R.C. Paietta, E.L. Burger, V.L. Ferguson, Mineralization and collagen orientation throughout aging at the vertebral endplate in the human lumbar spine, *Journal of structural biology* 184(2) (2013) 310-20.

- [30] L.M. Benneker, P.F. Heini, S.E. Anderson, M. Alini, K. Ito, Correlation of radiographic and MRI parameters to morphological and biochemical assessment of intervertebral disc degeneration, *Eur Spine J* 14(1) (2005) 27-35.
- [31] A. Przybyla, P. Pollintine, R. Bedzinski, M.A. Adams, Outer annulus tears have less effect than endplate fracture on stress distributions inside intervertebral discs: relevance to disc degeneration, *Clinical biomechanics* 21(10) (2006) 1013-9.
- [32] F.M. Williams, N.J. Manek, P.N. Sambrook, T.D. Spector, A.J. Macgregor, Schmorl's nodes: common, highly heritable, and related to lumbar disc disease, *Arthritis Rheum* 57(5) (2007) 855-60.
- [33] K.J. Faccia, R.C. Williams, Schmorl's nodes: clinical significance and implications for the bioarchaeological record, *International Journal of Osteoarchaeology* 18(1) (2008) 28-44.
- [34] G. Dar, Y. Masharawi, S. Peleg, N. Steinberg, H. May, B. Medlej, N. Peled, I. Hershkovitz, Schmorl's nodes distribution in the human spine and its possible etiology, *Eur Spine J* 19(4) (2010) 670-5.
- [35] K.A. Kyere, K.D. Than, A.C. Wang, S.U. Rahman, J.M. Valdivia-Valdivia, F. La Marca, P. Park, Schmorl's nodes, *Eur Spine J* 21(11) (2012) 2115-21.
- [36] N. Zhang, F.C. Li, Y.J. Huang, C. Teng, W.S. Chen, Possible key role of immune system in Schmorl's nodes, *Medical hypotheses* 74(3) (2010) 552-4.
- [37] M.A. Adams, W.C. Hutton, The relevance of torsion to the mechanical derangement of the lumbar spine, *Spine* 6(3) (1981) 241-248.
- [38] M.A. ADAMS, W.C. HUTTON, Prolapsed Intervertebral Disc: A Hyperflexion Injury, *Spine* 7(3) (1982) 184-191.
- [39] M.A. Adams, D.S. McNally, P. Dolan, 'Stress' distributions inside intervertebral discs. The effects of age and degeneration., *J Bone Joint Surg Br* 78(6) (1996) 965-972.
- [40] N. Newell, J.P. Little, A. Christou, M.A. Adams, C.J. Adam, S.D. Masouros, Biomechanics of the human intervertebral disc: A review of testing techniques and results, *Journal of the mechanical behavior of biomedical materials* 69 (2017) 420-434.
- [41] A.M. Nguyen, W. Johannessen, J.H. Yoder, A.J. Wheaton, E.J. Vresilovic, A. Borthakur, D.M. Elliott, Noninvasive quantification of human nucleus pulposus pressure with use of T1rho-weighted magnetic resonance imaging, *The Journal of bone and joint surgery. American volume* 90(4) (2008) 796-802.
- [42] M.A. Adams, P. Dolan, D.S. McNally, The internal mechanical functioning of intervertebral discs and articular cartilage, and its relevance to matrix biology, *Matrix Biol* 28(7) (2009) 384-9.
- [43] S. Sivan, Y. Merkher, E. Wachtel, S. Ehrlich, A. Maroudas, Correlation of swelling pressure and intrafibrillar water in young and aged human intervertebral discs, *J Orthop Res* 24(6) (2006) 1292-8.
- [44] S.P. Veres, P.A. Robertson, N.D. Broom, The influence of torsion on disc herniation when combined with flexion, *Eur Spine J* 19(9) (2010) 1468-78.

- [45] B.L. Showalter, J.C. Beckstein, J.T. Martin, E.E. Beattie, A.A. Espinoza Orias, T.P. Schaer, E.J. Vresilovic, D.M. Elliott, Comparison of animal discs used in disc research to human lumbar disc: torsion mechanics and collagen content, *Spine* 37(15) (2012) E900-7.
- [46] B. Yang, G.D. O'Connell, Effect of collagen fibre orientation on intervertebral disc torsion mechanics, *Biomechanics and modeling in mechanobiology* 16(6) (2017) 2005-2015.
- [47] N.L. Nerurkar, B.M. Baker, S. Sen, E.E. Wible, D.M. Elliott, R.L. Mauck, Nanofibrous biologic laminates replicate the form and function of the annulus fibrosus, *Nat Mater* 8(12) (2009) 986-92.
- [48] G.D. O'Connell, S. Sen, D.M. Elliott, Human annulus fibrosus material properties from biaxial testing and constitutive modeling are altered with degeneration, *Biomechanics and modeling in mechanobiology* 11(3-4) (2012) 493-503.
- [49] G.D. O'Connell, E.J. Vresilovic, D.M. Elliott, Human intervertebral disc internal strain in compression: the effect of disc region, loading position, and degeneration, *J Orthop Res* 29(4) (2011) 547-55.
- [50] J.C. Iatridis, S.B. Nicoll, A.J. Michalek, B.A. Walter, M.S. Gupta, Role of biomechanics in intervertebral disc degeneration and regenerative therapies: what needs repairing in the disc and what are promising biomaterials for its repair?, *Spine J* 13(3) (2013) 243-62.
- [51] D.H. Cortes, D.M. Elliott, Extra-fibrillar matrix mechanics of annulus fibrosus in tension and compression, *Biomechanics and modeling in mechanobiology* 11(6) (2012) 781-90.
- [52] D.H. Cortes, N.T. Jacobs, J.F. DeLucca, D.M. Elliott, Elastic, permeability and swelling properties of human intervertebral disc tissues: A benchmark for tissue engineering, *J Biomech* 47(9) (2014) 2088-2094.
- [53] J.M. Cloyd, N.R. Malhotra, L. Weng, W. Chen, R.L. Mauck, D.M. Elliott, Material properties in unconfined compression of human nucleus pulposus, injectable hyaluronic acid-based hydrogels and tissue engineering scaffolds, *Eur Spine J* 16(11) (2007) 1892-8.
- [54] G.D. O'Connell, H.L. Guerin, D.M. Elliott, Theoretical and uniaxial experimental evaluation of human annulus fibrosus degeneration, *J Biomech Eng* 131(11) (2009) 111007.
- [55] D.R. Wagner, J.C. Lotz, Theoretical model and experimental results for the nonlinear elastic behavior of human annulus fibrosus, *J Orthop Res* 22(4) (2004) 901-9.
- [56] A.J. Fields, D. Rodriguez, K.N. Gary, E.C. Liebenberg, J.C. Lotz, Influence of biochemical composition on endplate cartilage tensile properties in the human lumbar spine, *J Orthop Res* 32(2) (2014) 245-52.
- [57] L.A. Setton, W. Zhu, M. Weidenbaum, A. Ratcliffe, V.C. Mow, Compressive Properties of the Cartilaginous End-Plate of the Baboon Lumbar Spine, *J Orthop Res* 11 (1993) 228-239.

- [58] J. Debes, Y. Fung, Biaxial mechanics of excised canine pulmonary arteries, *American Journal of Physiology-Heart and Circulatory Physiology* 269(2) (1995) H433-H442.
- [59] Y. Lanir, Y. Fung, Two-dimensional mechanical properties of rabbit skin. I. Experimental system., *J Biomech* 7(1) (1974) 29-34.
- [60] Y. Lanir, Y. Fung, Two-dimensional mechanical properties of rabbit skin. II. Experimental results., *J Biomech* 7(2) (1974) 171-182.
- [61] E. Bass, F. Ashford, M. Segal, J. Lotz, Biaxial Testing of Human Annulus Fibrosus and Its Implications for a Constitutive Formulation, *Annals of Biomedical Engineering* 32(9) (2004) 1231-1242.
- [62] A.J. Fields, M. Han, R. Krug, J. Lotz, Cartilaginous end plates: quantitative MR imaging with very short echo times-orientation dependence and correlation with biochemical composition, *Radiology* (2014).
- [63] A. Eilaghi, J.G. Flanagan, I. Tertinegg, C.A. Simmons, G. Wayne Brodland, C. Ross Ethier, Biaxial mechanical testing of human sclera, *J Biomech* 43(9) (2010) 1696-701.
- [64] C. Bellini, P. Glass, M. Sitti, E.S. Di Martino, Biaxial mechanical modeling of the small intestine, *Journal of the mechanical behavior of biomedical materials* 4(8) (2011) 1727-40.
- [65] N.T. Jacobs, D.H. Cortes, E.J. Vresilovic, D.M. Elliott, Biaxial tension of fibrous tissue: using finite element methods to address experimental challenges arising from boundary conditions and anisotropy, *J Biomech Eng* 135(2) (2013) 021004.
- [66] S. Roberts, J.P. Urban, H. Evans, S. Einstein, Transport Properties of the Human Cartilage Endplate in Relation to Its Composition and Calcification, *Spine* 21(4) (1996) 415-420.
- [67] G.D. O'Connell, N.T. Jacobs, S. Sen, E.J. Vresilovic, D.M. Elliott, Axial creep loading and unloaded recovery of the human intervertebral disc and the effect of degeneration, *Journal of the mechanical behavior of biomedical materials* 4(7) (2011) 933-42.
- [68] C. Court, J.R. Chin, E. Liebenberg, O.K. Colliou, J.C. Lotz, Biological and mechanical consequences of transient intervertebral disc bending, *Eur Spine J* 16(11) (2007) 1899-906.
- [69] J.J. Costi, I.A. Stokes, M.G. Gardner-Morse, J.C. Iatridis, Frequency-dependent behavior of the intervertebral disc in response to each of six degree of freedom dynamic loading: solid phase and fluid phase contributions, *Spine* 33(16) (2008) 1731-8.
- [70] S.C. Chan, S.J. Ferguson, B. Gantenbein-Ritter, The effects of dynamic loading on the intervertebral disc, *Eur Spine J* 20(11) (2011) 1796-812.
- [71] I.A. Stokes, M. Gardner-Morse, A database of lumbar spinal mechanical behavior for validation of spinal analytical models, *J Biomech* 49(5) (2016) 780-5.
- [72] D. Amin, I. Lawless, D. Sommerfeld, R. Stanley, B. Ding, J. Costi, The effect of six degree of freedom loading sequence on the in-vitro compressive properties of human lumbar spine segments, *J Biomech In press.* (2016).

- [73] D. Amin, D. Sommerfeld, I. Lawless, R. Stanley, B. Ding, J. Costi, Effect of degeneration on the six degree of freedom mechanical properties of human lumbar spine segments, *J Orthop Res* 34(8) (2016) 1399-1409.
- [74] S.E. Bezci, A. Nandy, G.D. O'Connell, Effect of hydration on healthy intervertebral disk mechanical stiffness, *J Biomech Eng* 137(10) (2015) 101007.
- [75] J. Costi, T. Hearn, N. Fazzalari, The effect of hydration on the stiffness of intervertebral discs in an ovine model, *Clinical biomechanics* 17 (2002) 446-455.
- [76] F. Galbusera, H. Schmidt, J. Noailly, A. Malandrino, D. Lacroix, H.J. Wilke, A. Shirazi-Adl, Comparison of four methods to simulate swelling in poroelastic finite element models of intervertebral discs, *Journal of the mechanical behavior of biomedical materials* 4(7) (2011) 1234-41.
- [77] S. Ebara, J.C. Iatridis, L.A. Setton, R.J. Foster, V.C. Mow, M. Weidenbaum, Tensile properties of nondegenerate human lumbar annulus fibrosus, *Spine* 21(4) (1996) 452-461.
- [78] D. McMillan, G. Garbutt, M.A. Adams, Effect of sustained loading on the water content of intervertebral discs: implications for disc metabolism, *Annals of Rheumatic Diseases* 55(12) (1996) 880-887.
- [79] D. Pflaster, M. Krag, C. Johnson, L. Haugh, M. Pope, Effect of test environment on intervertebral disc hydration, *Spine* 22(2) (1997) 133-139.
- [80] M.G. Gardner-Morse, I.A. Stokes, Physiological axial compressive preloads increase motion segment stiffness, linearity and hysteresis in all six degrees of freedom for small displacements about the neutral posture, *J Orthop Res* 21 (2003) 547-552.
- [81] S.E. Bezci, E.O. Klineberg, G.D. O'Connell, Effects of axial compression and rotation angle on torsional mechanical properties of bovine caudal discs, *Journal of the mechanical behavior of biomedical materials* 77 (2018) 353-359.
- [82] H. Schmidt, C. Schilling, A.L.P. Reyna, A. Shirazi-Adl, M. Dreischarf, Fluid-flow dependent response of intervertebral discs under cyclic loading: On the role of specimen preparation and preconditioning, *J Biomech* 49(6) (2016) 846-856.
- [83] A. Race, N. Broom, P.A. Robertson, Effect of loading rate and hydration on the mechanical properties of the disc, *Spine* 25(6) (2000) 662-669.
- [84] H. Schmidt, A. Shirazi-Adl, C. Schilling, M. Dreischarf, Preload substantially influences the intervertebral disc stiffness in loading-unloading cycles of compression, *J Biomech* 49(9) (2016) 1926-1932.
- [85] P. Vergroesen, A. van der Veen, B. van Royen, I. Kingma, T. Smit, Intradiscal pressure depends on recent loading and correlates with disc height and compressive stiffness, *Eur Spine J* 23(11) (2014) 2359-2368.
- [86] G.D. O'Connell, W. Johannessen, E.J. Vresilovic, D.M. Elliott, Human Internal Disc Strains in Axial Compression Measured Noninvasively Using Magnetic Resonance Imaging, *Spine* 32(25) (2007) 2860-2868.
- [87] N. Dhillon, E. Bass, J. Lotz, Effect of frozen storage on the creep behavior of human intervertebral discs, *Spine* 26(8) (2001) 883-888.

- [88] D. Amin, I. Lawless, D. Sommerfeld, R. Stanley, B. Ding, J. Costi, Effect of potting technique on the measurement of six degree-of-freedom viscoelastic properties of human lumbar spine segments, *J Biomech Eng* 137 (2015) 054501.
- [89] B. Ding, B.S. Cazzolato, R. Stanley, S. Grainger, J. Costi, Stiffness analysis and control of a Stewart platform-based manipulator with decoupled sensor-actuator locations for ultrahigh accuracy positioning under large external loads, *Journal of Dynamic Systems, Measurement, and Control* 136(6) (2014) 061008.
- [90] T.P. Holsgrove, H.S. Gill, A.W. Miles, S. Gheduzzi, Dynamic, six-axis stiffness matrix characteristics of the intact intervertebral disc and a disc replacement, *Proc Inst Mech Eng H* 229(11) (2015) 769-77.
- [91] D. Spenciner, D. Greene, J. Paiva, M. Palumbo, J. Crisco, The multidirectional bending properties of the human lumbar intervertebral disc, *Spine J* 6(3) (2006) 248-57.
- [92] Y. Lanir, Mechanisms of residual stress in soft tissues, *J Biomech Eng* 131(4) (2009) 044506.
- [93] Y. Fung, S. Liu, Strain distribution in small blood vessels with zero-stress state taken into consideration, *American Journal of Physiology-Heart and Circulatory Physiology* 262(2) (1992) H544-H552.
- [94] J. Omens, Y. Fung, Residual strain in rat left ventricle, *Circulation Research* 66(1) (1990) 37-45.
- [95] H. Han, Y. Fung, Residual strains in porcine and canine trachea, *J Biomech* 24(5) (1991) 307-315.
- [96] A.J. Michalek, M.G. Gardner-Morse, J.C. Iatridis, Large residual strains are present in the intervertebral disc annulus fibrosus in the unloaded state, *J Biomech* 45(7) (2012) 1227-31.
- [97] S.E. Duclos, A.J. Michalek, Residual strains in the intervertebral disc annulus fibrosus suggest complex tissue remodeling in response to in-vivo loading, *Journal of the mechanical behavior of biomedical materials* 68 (2017) 232-238.
- [98] K.Y. Volokh, Stresses in growing soft tissues, *Acta Biomater* 2(5) (2006) 493-504.
- [99] K. Myers, G.A. Ateshian, Interstitial growth and remodeling of biological tissues: tissue composition as state variables, *Journal of the mechanical behavior of biomedical materials* 29 (2014) 544-56.
- [100] F. Niemeyer, H.J. Wilke, H. Schmidt, Geometry strongly influences the response of numerical models of the lumbar spine--a probabilistic finite element analysis, *J Biomech* 45(8) (2012) 1414-23.
- [101] K. Akeda, T. Yamada, N. Inoue, A. Nishimura, A. Sudo, Risk factors for lumbar intervertebral disc height narrowing: a population-based longitudinal study in the elderly, *BMC musculoskeletal disorders* 16 (2015) 344.
- [102] J.M. Pelouquin, J.H. Yoder, N.T. Jacobs, S.M. Moon, A.C. Wright, E.J. Vresilovic, D.M. Elliott, Human L3L4 intervertebral disc mean 3D shape, modes of variation, and their relationship to degeneration, *J Biomech* 47(10) (2014) 2452-9.

- [103] S. Roberts, J. Menage, S. Eisenstein, The cartilage end-plate and intervertebral disc in scoliosis: calcification and other sequelae, *J Orthop Res* 11 (1993) 747-757.
- [104] S. Rajasekaran, J.N. Babu, R. Arun, B.R. Armstrong, A.P. Shetty, S. Murugan, ISSLS Prize Winner: A study of diffusion in human lumbar discs: a serial magnetic resonance imaging study documenting the influence of the endplate on diffusion in normal and degenerate discs., *Spine* 29(23) (2004) 2654-2657.
- [105] J.F. DeLuca, D.H. Cortes, N.T. Jacobs, E.J. Vresilovic, R.L. Duncan, D.M. Elliott, Human Cartilage Endplate Permeability Varies with Degeneration and Intervertebral Disc Site, *J Biomech* (2016).
- [106] J. Aoki, I. Yamamoto, N. Kitamura, T. Sone, H. Itoh, K. Torizuka, K. Takasu, End Plate of the Discovertebral Joint: Degenerative Change in the Elderly Adult, *Radiology* 164(2) (1987) 411-414.
- [107] A.G. Rodriguez, C.K. Slichter, F.L. Acosta, A.E. Rodriguez-Soto, A.J. Burghardt, S. Majumdar, J.C. Lotz, Human disc nucleus properties and vertebral endplate permeability, *Spine* 36(7) (2011) 512-20.
- [108] C. Chen, Z. Jia, Z. Han, T. Gu, W. Li, H. Li, Y. Tang, J. Wu, D. Wang, Q. He, D. Ruan, Quantitative T2 relaxation time and magnetic transfer ratio predict endplate biochemical content of intervertebral disc degeneration in a canine model, *BMC musculoskeletal disorders* 16 (2015) 157.
- [109] W.C. Bae, S. Statum, Z. Zhang, T.W. Yamaguchi, T., A.C. Gamst, J. Du, G.M. Bydder, K. Masuda, C.B. Chung, Morphology of the Cartilaginous Endplates in Human Intervertebral Disks with Ultrashort Echo Time MR Imaging, *Radiology* 266(2) (2013) 564-574.
- [110] T. Law, M.P. Anthony, Q. Chan, D. Samartzis, M. Kim, K.M. Cheung, P.L. Khong, Ultrashort time-to-echo MRI of the cartilaginous endplate: technique and association with intervertebral disc degeneration, *Journal of medical imaging and radiation oncology* 57(4) (2013) 427-34.
- [111] S.M. Moon, J.H. Yoder, A.C. Wright, L.J. Smith, E.J. Vresilovic, D.M. Elliott, Evaluation of intervertebral disc cartilaginous endplate structure using magnetic resonance imaging, *Eur Spine J* (2013).
- [112] G.H. Welsch, S. Trattnig, T. Paternostro-Sluga, K. Bohndorf, S. Goed, D. Stelzener, T.C. Mamisch, Parametric T2 and T2* mapping techniques to visualize intervertebral disc degeneration in patients with low back pain: initial results on the clinical use of 3.0 Tesla MRI, *Skeletal radiology* 40(5) (2011) 543-51.
- [113] R: A Language And Environment For Statistical Computing. <<https://www.R-project.org/>>, 2015).
- [114] Y. Zhang, B.A. Lenart, J.K. Lee, D. Chen, P. Shi, J. Ren, C. Muehleman, D. Chen, H.S. An, Histological features of endplates of the mammalian spine: from mice to men, *Spine* 39(5) (2014) E312-7.
- [115] P. Lama, U. Zehra, C. Balkovec, H.A. Claireaux, L. Flower, I.J. Harding, P. Dolan, M.A. Adams, Significance of cartilage endplate within herniated disc tissue, *Eur Spine J* (2014).

- [116] T. Grunhagen, G. Wilde, D.M. Soukane, A. Shirazi-Adl, J. Urban, Nutrient supply and intervertebral disc metabolism, *J Bone Joint Surg* 88(Suppl. 2) (2006) 30-35.
- [117] S. Motaghinasab, A. Shirazi-Adl, M. Parnianpour, J.P. Urban, Disc size markedly influences concentration profiles of intravenously administered solutes in the intervertebral disc: a computational study on glucosamine as a model solute, *Eur Spine J* 23(4) (2014) 715-23.
- [118] S.A. Rodrigues, K.R. Wade, A. Thambyah, N.D. Broom, Micromechanics of annulus-end plate integration in the intervertebral disc, *Spine J* 12(2) (2012) 143-50.
- [119] Y.S. Nosikova, J.P. Santerre, M. Grynepas, G. Gibson, R.A. Kandel, Characterization of the annulus fibrosus-vertebral body interface: identification of new structural features, *Journal of anatomy* 221(6) (2012) 577-89.
- [120] J.H. Yoder, J.M. Peloquin, G. Song, N.J. Tustison, S.M. Moon, A.C. Wright, E.J. Vresilovic, J.C. Gee, D.M. Elliott, Internal three-dimensional strains in human intervertebral discs under axial compression quantified noninvasively by magnetic resonance imaging and image registration, *J Biomech Eng* 136(11) (2014).
- [121] S. Kokubun, M. Sakurai, Y. Tanaka, Cartilaginous endplate in cervical disc herniation, *Spine* 21(2) (1996) 190-195.
- [122] E. Joe, J.W. Lee, K.W. Park, J.S. Yeom, E. Lee, G.Y. Lee, H.S. Kang, Herniation of Cartilaginous Endplates in the Lumbar Spine: MRI Findings, *American Journal of Roentgenology* 204(5) (2015) 1075-1081.
- [123] J.C. Lotz, A.J. Fields, E.C. Liebenberg, The role of the vertebral end plate in low back pain, *Global Spine J* 3 (2013) 153-164.
- [124] L.A. Setton, D.M. Elliott, V.C. Mow, Altered mechanics of cartilage with osteoarthritis: human osteoarthritis and an experimental model of joint degeneration, *Osteoarthritis and Cartilage* 7(1) (1999) 2-14.
- [125] A.C. Moore, D.L. Burris, An analytical model to predict interstitial lubrication of cartilage in migrating contact areas, *J Biomech* 47(1) (2014) 148-53.
- [126] A.R. Jackson, C.Y. Huang, M.D. Brown, W.Y. Gu, 3D finite element analysis of nutrient distributions and cell viability in the intervertebral disc: effects of deformation and degeneration, *J Biomech Eng* 133(9) (2011) 091006.
- [127] A.R. Jackson, C.Y. Huang, W.Y. Gu, Effect of endplate calcification and mechanical deformation on the distribution of glucose in intervertebral disc: a 3D finite element study, *Comput Methods Biomech Biomed Engin* 14(2) (2011) 195-204.
- [128] A. Shirazi-Adl, M. Taheri, J.P. Urban, Analysis of cell viability in intervertebral disc: Effect of endplate permeability on cell population, *J Biomech* 43(7) (2010) 1330-6.
- [129] J.P. Grant, T.R. Oxland, M.F. Dvorak, C.G. Fisher, The effects of bone density and disc degeneration on the structural property distributions in the lower lumbar vertebral endplates, *J Orthop Res* 20 (2002) 1115-1120.
- [130] Y. Hou, W. Yuan, Influences of disc degeneration and bone mineral density on the structural properties of lumbar end plates, *Spine J* 12(3) (2012) 249-56.

- [131] A. Malandrino, J.A. Planell, D. Lacroix, Statistical factorial analysis on the poroelastic material properties sensitivity of the lumbar intervertebral disc under compression, flexion and axial rotation, *J Biomech* 42(16) (2009) 2780-8.
- [132] M. Qasim, R.N. Natarajan, H.S. An, G.B. Andersson, Initiation and progression of mechanical damage in the intervertebral disc under cyclic loading using continuum damage mechanics methodology: A finite element study, *J Biomech* 45(11) (2012) 1934-40.
- [133] S.J. Ferguson, K. Ito, L.-P. Nolte, Fluid flow and convective transport of solutes within the intervertebral disc, *J Biomech* 37(2) (2004) 213-221.
- [134] D.H. Cortes, J.F. Magland, A.C. Wright, D.M. Elliott, The shear modulus of the nucleus pulposus measured using magnetic resonance elastography: a potential biomarker for intervertebral disc degeneration, *Magn Reson Med* 72(1) (2014) 211-9.
- [135] N.L. Marinelli, V.M. Haughton, P.A. Anderson, T2 relaxation times correlated with stage of lumbar intervertebral disk degeneration and patient age, *AJNR Am J Neuroradiol* 31(7) (2010) 1278-82.
- [136] N.T. Jacobs, D.H. Cortes, J.M. Peloquin, E.J. Vresilovic, D.M. Elliott, Validation and application of an intervertebral disc finite element model utilizing independently constructed tissue-level constitutive formulations that are nonlinear, anisotropic, and time-dependent, *J Biomech* 47(11) (2014) 2540-6.
- [137] G.A. Ateshian, V. Rajan, N.O. Chahine, C.E. Canal, C.T. Hung, Modeling the matrix of articular cartilage using a continuous fiber angular distribution predicts many observed phenomena, *J Biomech Eng* 131(6) (2009) 061003.
- [138] R.E. Wilusz, J. Sanchez-Adams, F. Guilak, The structure and function of the pericellular matrix of articular cartilage, *Matrix Biol* 39 (2014) 25-32.
- [139] A. Nachemson, T. Lewin, A. Maroudas, M. Freeman, In vitro diffusion of dye through the end-plates and the annulus fibrosus of human lumbar inter-vertebral discs, *Acta Orthop Scand* 41(6) (1970) 589-607.
- [140] A. Malandrino, D. Lacroix, C. Hellmich, K. Ito, S.J. Ferguson, J. Noailly, The role of endplate poromechanical properties on the nutrient availability in the intervertebral disc, *Osteoarthritis and Cartilage* 22(7) (2014) 1053-60.
- [141] Q. Zhu, A.R. Jackson, W.Y. Gu, Cell viability in intervertebral disc under various nutritional and dynamic loading conditions: 3d finite element analysis, *J Biomech* 45(16) (2012) 2769-77.
- [142] A. Malandrino, J. Noailly, D. Lacroix, Numerical exploration of the combined effect of nutrient supply, tissue condition and deformation in the intervertebral disc, *J Biomech* 47(6) (2014) 1520-5.
- [143] S.S. Sivan, E. Tsitron, E. Wachtel, P. Roughley, N. Sakkee, F. van der Ham, J. Degroot, A. Maroudas, Age-related accumulation of pentosidine in aggrecan and collagen from normal and degenerate human intervertebral discs, *Biochem J* 399(1) (2006) 29-35.
- [144] J.P. Grant, T. Oxland, M.F. Dvorak, Mapping the Structural Properties of the Lumbosacral Vertebral Endplates, *Spine* 26(8) (2001) 889-896.

- [145] F.D. Zhao, P. Pollintine, B.D. Hole, M.A. Adams, P. Dolan, Vertebral fractures usually affect the cranial endplate because it is thinner and supported by less-dense trabecular bone, *Bone* 44(2) (2009) 372-9.
- [146] A. Malandrino, J. Noailly, D. Lacroix, The effect of sustained compression on oxygen metabolic transport in the intervertebral disc decreases with degenerative changes, *PLoS computational biology* 7(8) (2011) e1002112.
- [147] A.C. Moore, D.L. Burris, Tribological and material properties for cartilage of and throughout the bovine stifle: support for the altered joint kinematics hypothesis of osteoarthritis, *Osteoarthritis and Cartilage* 23(1) (2015) 161-9.
- [148] A.C.B. Chen, W.C., R.M. Schinagl, R.L. Sah, Depth- and strain-dependent mechanical and electromechanical properties of full-thickness bovine articular cartilage in confined compression, *J Biomech* 34 (2001) 1-12.
- [149] K.A. Athanasiou, M.P. Rosenwasser, J.A. Buckwalter, T.I. Malinin, V.C. Mow, Interspecies comparisons of in situ intrinsic mechanical properties of distal femoral cartilage, *J Orthop Res* 9(3) (1991) 330-340.
- [150] V.C. Mow, S.C. Kuei, W.M. Lai, C.G. Armstrong, Biphasic Creep and Stress Relaxation of Articular Cartilage in Compression: Theory and Experiments, *J Biomech Eng* 102 (1980) 73-84.
- [151] C.Y. Huang, M.A. Soltz, M. Kopacz, V.C. Mow, G.A. Ateshian, Experimental verification of the roles of intrinsic matrix viscoelasticity and tension-compression nonlinearity in the biphasic response of cartilage, *J Biomech Eng* 125(1) (2003) 84-93.
- [152] G.A. Ateshian, M.A. Soltz, R.L. Mauck, I.M. Basalo, C.T. Hung, W.M. Lai, The role of osmotic pressure and tension-compression nonlinearity in the frictional response of articular cartilage, *Transport in Porous Media* 50 (2003) 5-33.
- [153] N.O. Chahine, C.C. Wang, C.T. Hung, G.A. Ateshian, Anisotropic strain-dependent material properties of bovine articular cartilage in the transitional range from tension to compression, *J Biomech* 37(8) (2004) 1251-61.
- [154] J.A.M. Buckwalter, V.C., A. Ratcliffe, Restoration of injured or degenerated articular cartilage, *J Am Acad Orthop Surg* 2(4) (1994) 192-201.
- [155] C.G. Armstrong, V.C. Mow, Variations in the intrinsic mechanical properties of human articular cartilage with age, degeneration, and water content, *J Bone Joint Surg* 64 (1982) 88-94.
- [156] C. Canal Guterl, C.T. Hung, G.A. Ateshian, Electrostatic and non-electrostatic contributions of proteoglycans to the compressive equilibrium modulus of bovine articular cartilage, *J Biomech* 43(7) (2010) 1343-50.
- [157] M. Panjabi, M. Krag, V.K. Goel, A technique for measurement and description of three-dimensional six degree-of-freedom motion of a body joint with an application to the human spine, *J Biomech* 14(7) (1981) 447-449.
- [158] J. Lysack, J. Dickey, G. Dumas, D. Yen, A continuous pure moment loading apparatus for biomechanical testing of multi-segment spine specimens., *J Biomech* 33(6) (2000) 765-770.

- [159] A. Patwardhan, R. Havey, K. Meade, B. Lee, B. Dunlap, A follower load increases the load-carrying capacity of the lumbar spine in compression., *Spine* 24(10) (1999) 1003-1009.
- [160] D.J. Goertzen, C. Lane, T.R. Oxland, Neutral zone and range of motion in the spine are greater with stepwise loading than with a continuous loading protocol. An in vitro porcine investigation, *J Biomech* 37(2) (2004) 257-261.
- [161] H.J. Wilke, L. Claes, H. Schmitt, S. Wolf, A universal spine tester for in vitro experiments with muscle force simulation, *Eur Spine J* 3(2) (1994) 91-97.
- [162] J.D. Auerbach, C.M. Ballester, F. Hammond, E.T. Carine, R.A. Balderston, D.M. Elliott, The effect of implant size and device keel on vertebral compression properties in lumbar total disc replacement, *Spine J* 10(4) (2010) 333-40.
- [163] J.B. Tan, C.S., M.F. Dvorak, C.G. Fisher, T. Oxland, Interbody Device Shape and Size are Important to Strengthen the Vertebra-Implant Interface, *Spine* 30(6) (2005) 638-644.
- [164] K.R. Wade, P.A. Robertson, A. Thambyah, N.D. Broom, How healthy discs herniate: a biomechanical and microstructural study investigating the combined effects of compression rate and flexion, *Spine* 39(13) (2014) 1018-28.
- [165] M.A. Adams, W.C. Hutton, The effect of fatigue on the lumbar intervertebral disc, *Journal of Bone and Joint Surgery (British)* 65(2) (1983) 199-203.
- [166] J.J. Costi, I.A. Stokes, M. Gardner-Morse, J.P. Laible, H.M. Scoffone, J.C. Iatridis, Direct measurement of intervertebral disc maximum shear strain in six degrees of freedom: motions that place disc tissue at risk of injury, *J Biomech* 40(11) (2007) 2457-66.
- [167] J.C. Beckstein, S. Sen, T.P. Schaer, E.J. Vresilovic, D.M. Elliott, Comparison of animal discs used in disc research to human lumbar disc, *Spine* 33(6) (2008) E166-E173.
- [168] F. Heuer, H. Schmidt, Z. Klezl, L. Claes, H.J. Wilke, Stepwise reduction of functional spinal structures increase range of motion and change lordosis angle, *J Biomech* 40(2) (2007) 271-80.
- [169] D.K. Stolworthy, S.A. Zirbel, L.L. Howell, M. Samuels, A.E. Bowden, Characterization and prediction of rate-dependent flexibility in lumbar spine biomechanics at room and body temperature, *Spine J* 14(5) (2014) 789-98.
- [170] K.M. Bell, R.A. Hartman, L.G. Gilbertson, J.D. Kang, In vitro spine testing using a robot-based testing system: comparison of displacement control and "hybrid control", *J Biomech* 46(10) (2013) 1663-9.
- [171] D.L. van Duersen, C.J. Snijders, J.H. van Dieen, I. Kingma, L.L.J.M. van Duersen, The effect of passive vertebral rotation on pressure in the nucleus pulposus, *J Biomech* 34(3) (2001) 405-408.
- [172] A. Nachemson, J. Morris, IN VIVO MEASUREMENTS OF INTRADISCAL PRESSURE. DISCOMETRY, A METHOD FOR THE DETERMINATION OF PRESSURE IN THE LOWER LUMBAR DISCS., *The Journal of bone and joint surgery. American volume* 46 (1964) 1077-1092.

- [173] I.M. Lawless, B. Ding, B.S. Cazzolato, J.J. Costi, Adaptive velocity-based six degree of freedom load control for real-time unconstrained biomechanical testing, *J Biomech* 47(12) (2014) 3241-7.
- [174] M. Pearcy, I. Portek, J. Shepherd, Three-dimensional x-ray analysis of normal movement in the lumbar spine, *Spine* 9 (1984) 294-297.
- [175] M. Pearcy, S.B. Tibrewal, Axial rotation and lateral bending in the normal lumbar spine measured by three-dimensional radiography, *Spine* 9 (1984) 582-587.
- [176] S. Wang, W.M. Park, Y.H. Kim, T. Cha, K. Wood, G. Li, In vivo loads in the lumbar L3-4 disc during a weight lifting extension, *Clinical biomechanics* 29(2) (2014) 155-60.
- [177] M. Dreischarf, A. Rohlmann, F. Graichen, G. Bergmann, H. Schmidt, In vivo loads on a vertebral body replacement during different lifting techniques, *J Biomech* 49(6) (2016) 890-895.
- [178] M. Dreischarf, A. Shirazi-Adl, N. Arjmand, A. Rohlmann, H. Schmidt, Estimation of loads on human lumbar spine: A review of in vivo and computational model studies, *J Biomech* 49(6) (2016) 833-845.
- [179] J.J. Costi, B.J. Freeman, D.M. Elliott, Intervertebral disc properties: challenges for biodevices, *Expert Review of Medical Devices* 8(3) (2011) 357-376.
- [180] A.M. Ellingson, T.M. Nagel, D.W. Polly, J. Ellermann, D.J. Nuckley, Quantitative T2* (T2 star) relaxation times predict site specific proteoglycan content and residual mechanics of the intervertebral disc throughout degeneration, *J Orthop Res* 32(8) (2014) 1083-9.
- [181] W. Wilson, A Comparison Between Mechano-Electrochemical and Biphasic Swelling Theories for Soft Hydrated Tissues, *J Biomech Eng* 127(1) (2005) 158.
- [182] G.A. Ateshian, T. Ricken, Multigenerational interstitial growth of biological tissues, *Biomechanics and modeling in mechanobiology* 9(6) (2010) 689-702.
- [183] S.A. Maas, B.J. Ellis, G.A. Ateshian, J.A. Weiss, FEBio: finite elements for biomechanics, *J Biomech Eng* 134(1) (2012) 011005.
- [184] B.L. Showalter, J.F. DeLucca, J.M. Peloquin, D.H. Cortes, J.H. Yoder, N.T. Jacobs, A.C. Wright, J.C. Gee, E.J. Vresilovic, D.M. Elliott, A novel human intervertebral disc strain template to quantify regional three-dimensional strains in a population and compare to internal strains predicted by a finite element model, *J Orthop Res* (2015).
- [185] G.A. Holzapfel, C. Schulze-Bauer, G. Feigl, P. Regitnig, Single lamellar mechanics of the human lumbar anulus fibrosus, *Biomechanics and modeling in mechanobiology* 3(3) (2005) 125-140.
- [186] R.J. Nims, G.A. Ateshian, Reactive Constrained Mixtures for Modeling the Solid Matrix of Biological Tissues, *Journal of Elasticity* 129(1-2) (2017) 69-105.
- [187] B.L. Showalter, N.R. Malhotra, E.J. Vresilovic, D.M. Elliott, Nucleotomy reduces the effects of cyclic compressive loading with unloaded recovery on human intervertebral discs, *J Biomech* 47(11) (2014) 2633-40.
- [188] A. Rufai, M. Benjamin, J. Ralphs, The development of fibrocartilage in the rat intervertebral disc, *Anatomy and Embryology* 192(1) (1995) 53-62.

- [189] A.J. Hayes, M. Benjamin, J. Ralphs, Role of actin stress fibres in the development of the intervertebral disc: cytoskeletal control of extracellular matrix assembly, *Developmental Dynamics* 215(3) (1999) 179-189.
- [190] A. Peacock, Observations on the prenatal development of the intervertebral disc in man, *Journal of anatomy* 85(3) (1951) 260-274.
- [191] A. Peacock, Observations on the postnatal structure of the intervertebral disc in man, *Journal of anatomy* 86 (1952) 162-179.
- [192] L.T. Muftuler, J.P. Jarman, H.J. Yu, V.O. Gardner, D.J. Maiman, V.E. Arpinar, Association between intervertebral disc degeneration and endplate perfusion studied by DCE-MRI, *Eur Spine J* 24(4) (2015) 679-85.

APPENDIX A

PERMISSIONS AND RIGHTS

At the time of the submission of the thesis, the work in Chapter 3 was published in the Journal of Orthopedic Research and the work in Chapter 4 was published in the Journal of Biomechanics. Both journals allow manuscripts to be published in academic dissertations without permission from the journal.

Journal of Orthopedic Research:

<https://www.elsevier.com/journals/journal-of-orthopaedics/0972-978X/guide-for-authors>

Submission declaration

Submission of an article implies that the work described has not been published previously (except in the form of an abstract, a published lecture or academic thesis, see '[Multiple, redundant or concurrent publication](#)' for more information), that it is not under consideration for publication elsewhere, that its publication is approved by all authors and tacitly or explicitly by the responsible authorities where the work was carried out, and that, if accepted, it will not be published elsewhere in the same form, in English or in any other language, including electronically without the written consent of the copyright-holder.

Journal of Biomechanics:

<https://www.elsevier.com/about/policies/copyright/permissions>

Can I include/use my article in my thesis/dissertation? –

Yes. Authors can include their articles in full or in part in a thesis or dissertation for non-commercial purposes.